UNIVERSITY OF CALIFORNIA,
IRVINE

Formation of Galactic Components in Milky-Way-mass Galaxy Simulations

DISSERTATION

submitted in partial satisfaction of the requirements
for the degree of

DOCTOR OF PHILOSOPHY

in Physics

by

Sijie Yu

Dissertation Committee:
Professor James S. Bullock, Chair
Professor Michael Cooper
Professor Manoj Kaplinghat

2022

DEDICATION

To my parents

TABLE OF CONTENTS

LIST OF FIGURES

LIST OF TABLES

ACKNOWLEDGMENTS

I would like to thank my advisor Dr. James S. Bullock for guiding me through my graduate career. This is one of the best choices I have ever made in my life. I have always looked up to you as my role model. Thank you for making graduate school a wonderful place full of joy and excitement.

I would like to thank my committee members, Mike Cooper and Manoj Kaplinghat, for their time and help. I would like to show acknowledgement to all the present and past members of the UCI astronomy group for giving me a lot of support and inspirations. I am especially thankful for all the members in Bullock's group. I would also like to thank all the graduate students who helped mentor me during this time, and specifically Andrew Graus and Zach Hafen for the time when James was busy or away. I would also thank all of the collaborators in the FIRE simulation group. I want to thank Andrew Wetzel, Michael Boylan-Kolchin, Jonathan Stern, Alex Gurvich, Phil Hopkins, and Robyn Sandersons. I learnt a lot in the collaboration.

I would like to thank all my friends and colleagues who have supported me over the past six years. I want to thank Vincent for the care and support during the writing of this thesis. I want to thank Nick "taco" for always being patient, caring, and helpful. I want to thank Mishu for being the (best) (dancing) potato. I want to thank Jake for being extremely patient and helpful, especially when I was preparing for my job interviews. Michael, Matt, Cody, Alexis, Laura, Katy, Tyler, and everyone else from UCI, thank you for making this place full of wonderful memories. And Bryan, thank you for always checking on me and helping me prepare for my data scientist interviews, although you went to pharmacy school. I really wish all of you all the best in the future. It's all the people I have met here that makes this place unforgettable.

I also want to thank all my friends in undergrad. Zhenlin Zhu, Xiaoxi Wu, and Lu Lu, thank you for being my partner-in-crime. Yifei Luo, Zhen Wan, Qilao Gu, and Lei Zhou, thank you for all the meaningful talks and discussions. Li Zhang, thank you for being the best basketball coach and I will always miss you.

I want to express my gratitude to my dearest friend Yixuan "Berber" Lu for her company over the past almost 20 years. I will always and forever be your friend.

Finally, it would be impossible for me to go this far without the support from my family. I have never said it out loud but I always love you. And I hope you are proud of me.

A portion of this dissertation has been published in the Oxford University Press. Specifically Chapter 2 was published in the Monthly Notices of the Royal Astronomical Society (MNRAS) 494, 1536. Chapter 3 was published in MNRAS 505, 889. This work was supported by NSF grants AST-1910346 and AST-1518291. Part of the work was also provided from HST-AR-14282 and HST-AR-13888 from the Space Telescope Science Institute (STScI), which is operated by AURA, Inc., under NASA contract NAS5–26555. Additional

support was provided to co-authors from NSF grants AST-1517226, AST-1910346, AST-1715847, AST-1911233, AST-1517491, AST-1715216, AST-1652522, AST-1516374, DGE-0948017, DGE-145000. Co–author support was also provided from NSF CAREER grant AST-1752913, AST-1455342. Co–author support was also provided from National Science Foundation Graduate Research Fellowship Program under grant DGE-1839285, and DGE-1842165. Co–author support was also provided from the German Science Foundation via DIP grant STE 1869/2-1 GE 625/17-1. Co–author support was also provided from NASA, through ATP grant 80NSSC18K1097, 80NSSC20K0513, 80NSSC18K0562, 17-ATP17-0067, and grant NNX17AG29G. Co–author support was also provided from HST-GO-14734, HST-AR-15057, HST- AR-14282, HST-AR-14554, HST-AR-15006, HST-GO-14191, HST-AR-15809, HST-GO-15902, and HST-GO-15658 from STScI. Co–author support was also provided from a Scialog Award from the Heising-Simons Foundation, a Hellman Fellowship, a Cottrell Scholar Award from the Research Corporation for Science Advancement, and a Gary A. McCue postdoctoral fellowship at UC Irvine. Simulations were run using: XSEDE, supported by NSF grant ACI-1548562; Blue Waters, supported by the NSF; Pleiades, via the NASA HEC program through the NAS Division at Ames Research Center. Part of our data analysis were performed on the Green Planet cluster at the University of California, Irvine. This research also utilized `astropy`, a community–developed core Python package for Astronomy [12, 11]. The Python packages `NumPy` [105], `iPython` [180], `SciPy` [125], `matplotlib` [121], and scikit–learn [179] were also utilized for the majority of our data analysis and presentation. This work also made use of the NASA Astrophysics Data System.

VITA

Sijie Yu

EDUCATION

Doctor of Philosophy in Physics **2022**
University of California, Irvine *Irvine, California*

Bachelor of Science in Astronomy **2016**
Nanjing university *Nanjing, Jiangsu, China*

RESEARCH EXPERIENCE

Graduate Research Assistant **2017–2022**
University of California, Irvine *Irvine, California*

Undergraduate Research Assistant **2015**
University of Wisconsin - Madison *Madison, Wisconsin*

TEACHING EXPERIENCE

Graduate Teaching Assistant **2016–2019**
University of California, Irvine *Irvine, California*

REFEREED JOURNAL PUBLICATIONS

1. **S. Yu**, J. S. Bullock, C. Klein, J. Stern,A. Wetzel, M. Xiangcheng, J. Moreno, Z. Hafen, A. B. Gurvich, P. F. Hopkins, D. Kereš, C. Faucher-Giguère, R. Feldmann, and E. Quataert. *The bursty origin of the Milky Way thick disc*, Monthly Notices of the Royal Astronomical Society, 505, 889 (2021)

2. **S. Yu**, J. S. Bullock, A. Wetzel, R. E. Sanderson, A. S. Graus, M. Boylan-Kolchin, A. M. Nierenberg, M. Y. Grudić, P. F. Hopkins, D. Kereš, and C. Faucher-Giguère. *Stars made in outflows may populate the stellar halo of the Milky Way*, Monthly Notices of the Royal Astronomical Society, 494, 1539 (2020)

ABSTRACT OF THE DISSERTATION

Formation of Galactic Components in Milky-Way-mass Galaxy Simulations

By

Sijie Yu

Doctor of Philosophy in Physics

University of California, Irvine, 2022

Professor James S. Bullock, Chair

This thesis presents a computational study of the formation and evolution of Milky-Way-mass galaxies using FIRE-2 cosmological zoom-in simulations. All simulated galaxies experience an early period of bursty star formation that transitions to a late-time steady phase of near-constant star formation. Stars form at different time have very different kinematic properties, morphologies, and chemical abundances. We classify stars in the central galaxy as bulge, thick-disc, and thin-disc according to their orbital properties and discover that these components are assembled in a time-sequence from early to late times, respectively. Stars born during the early bursty phase have more radial orbits and they evolve into a central spheroidal structure at $z = 0$, while stars form during the late-time steady phase have more circular orbits and thin-disc-like morphology. Thick-disc stars form during a transitional period, mostly before the star formation settles down. Thus, we find a strong correlation between the age of thick-disc population at $z = 0$ and the transition time. We also find that galaxies with earlier transition from bursty to steady star formation have higher thin-disc fractions at $z = 0$. Bursty star formation at early time also triggers a significant amount of strong outflow events. During starbursts, the instantaneous fraction of stars born in outflows can be as high as $\sim 20 - 50\%$. These outflow stars contribute substantially to the in-situ stellar halo. Statistically, stellar populations form at different times tend to maintain their disc/bulge-like kinematics, with only moderate evolution over

time. Mergers do alter kinematics, but play a secondary role in "disc-settling" process. They do not destroy the thin disc nor change broad trend between star formation transition time and thin/thick-disc/bulge properties. If our simulations are representative of the Universe, then stellar archaeological studies of the Milky Way can provide a window into past star-formation modes in the Galaxy. Current age estimates of the Galactic thick disc would suggest that Milky Way transitioned from bursty to steady phase > 6.5 Gyr ago; prior to that time the Milky Way likely lacked a stable thin disc and underwent intense outflow activities.

Chapter 1

Introduction

1.1 The Milky Way Disc

Many galaxies have been shown to have discs that are composed of two kinematically and chemically different populations and they are often described as a thin disc embedded within a thick disc. They were first identified in external galaxies [42, 223]. Later Gilmore & Reid et al. 1983 [96] discovered that the Milky Way has a significant thick disc. They found an excessive part in the stellar density profile perpendicular to the disc plane. When using scale heights to characterizing the vertical distribution of the stars in the disc, there is a first deep exponential component of thin disc with small scale height of $\sim$ 300 pc along with a thick disc component that has scale height of $\sim$ 1 kpc in the tail.

Thin-disc stars are usually observed to be young, metal-rich, while thick-disc stars are older, more metal-poor, and more alpha-enhanced [87, 27, 138, 110, 107, 151, 210]. There is a clear dichotomy in the abundance of α elements relative to iron ([α/Fe]) - a high-α and a low-α population. While it's natural to associate this dichotomy with two distinct and separate kinematic populations, it may also be explained without requiring a distinct thick

disc component that emerged from a separate evolutionary path (e.g., Sharma et al. 2021 [209]).

When, why, and how thick and thin disc populations arise within the broader story of galaxy formation remains a key question in galaxy formation from both theoretical and observational perspectives. One of the most prevailing ideas is that thin discs are present even at high redshift, with thick discs forming later as a result of the heating of thin discs in mergers with small satellite galaxies [186, 130, 185]. Alternatively, stars could be born in relatively thick discs at early times, with thin discs emerging only relatively recently. Many recent cosmological simulations naturally produce $z = 0$ discs with young stars concentrated in a thin component [146, 164, 98, 181, 29, 178, 100, 10] and these same simulations at high redshift, however, produce discs that are systematically thicker and clumpier. Indeed, modern observations demonstrate that the bulk of star-forming galaxies at higher redshift have irregular morphologies, dominated by massive star-forming clumps [70, 72, 208, 177, 232, 102, 237]. Many of these systems are perturbed and turbulent, with low rotation-to-dispersion ratios. Only at low redshift and in relatively massive galaxies does thin disc start to emerge. This observed transition from irregular galaxies at high redshift to thin rotation-dominated discs at low redshift is sometimes referred to as the era of "disc settling" [128, 230, 222].

While "upside-down" disc formation is popular in simulations, the physical origin of this transition remains undetermined. One possibility is that discs are born thick during the early period of gas-rich mergers [34]. At high redshift, high star formation rate densities, high gas fractions, and feedback-induced turbulence could contribute to an initially hot disc [139]. An alternative possibility is that chaotic accretion of gas heat the pre-existing thin disc [160]. In this thesis, we explore the transition from thick to thin disc formation using FIRE-2 cosmological zoom-in simulations. The discs in our simulations tend to form upside-down, with thick discs in place early and then thin disc forming at late time. We find

that the transition from thick-disc to thin-disc formation is associated with transitions in multiple other properties. The onset of the formation of thin disc appears to be related to the transition from bursty to steady star formation, the formation of a rotationally-supported interstellar medium (ISM), and the virialisation of the inner circumgalactic medium (CGM). If this is true in the real Universe, the stellar archaeological studies of the Milky Way could provide a window into past star formation modes, as well as the build up of the Galactic CGM.

1.2 Galactic Bulge

Baade 1946 [14] and Stebbins & Whitford 1947 [215] first identified the Galactic bulge as a distinct component of our galaxy. It is the prominent over-density present in the inner few kiloparsecs of the Galaxy. Central bulges are common among Milky-Way-mass galaxies in the nearby universe and they can further be diagnosed into *classical bulges* and *pseudo bulges*. Classical bulges are usually more spheroidal and similar to elliptical galaxies, while pseudo bulges are flattened, mildly rotating, and appear more disc-like [135, 13, 82, 90]. Milky Way has been shown to have a small classical bulge and more dominant pseudo bulge [97]. The majority of the stars in the bulge are old, typically $\gtrsim$ 10 Gyr [220, 115, 175, 80, 238, 45, 37, 224].

One of the major questions in galaxy evolution is how bulges relate to disc formation – are the processes connected or completely disjoint? While the traditional scenario is that bulges form through violent processes, such as hierarchical clustering via mergers, in the early phase of the Milky Way evolution [175, 225, 238, 37, 119, 127], there are growing indications that bulges can form in multiple ways and bulge mass does not appear to be linked closely to merger history [17]. Some bulge material may come from stars and gas with high initial angular momentum support that is later scrambled by secular processes[46, 187, 169, 51,

149, 13, 61, 59, 166]. Another possibility is that bulges are formed directly from turbulently supported gas or the migration of giant gaseous clumps at high redshifts [70, 161, 44]. Rapid gas inflow to the galaxy center is another possibility [202].

The Milky Way bulge appears to have formed fairly early, with its chemical properties and stellar populations consistent with a star-formation timescale within $\sim$ 2 Gyr [15]. These properties are generally consistent with either the bulge forming early, prior to the disc formation altogether or the merging of early thick-disc subclumps, which migrate to the center to form the bulge. If the bulge formed from disc material through a bar instability or a triggered event, such a process would have to happen quite early, though the expected fraction of young stars and the detailed chemical patterns expected from disc-driven scenarios would depend on the timescales of the secular processes.

In this thesis, we try to gain some insight into the process of bulge formation. All of our Milky-Way-mass systems are shown to have a thin and thick disc with a central bulge. The bulge stars appear to be the oldest population that formed first in the galaxies, before the emergence of thin and thick discs. They were born when galaxies were very disordered and clumpy. Due to stronger feedback and less constraint from the inner CGM, most of bulge stars form on more radial and isotropic orbits and they remain in relatively spheroidal configurations at $z = 0$.

1.3 Stellar Halo of the Milky Way

Stellar halo is the very outskirt of the galaxies. It contains only $\sim$ 1% of the stars in a typical disc galaxy [56, 150] but spread out over volumes of $\sim 10^6$ larger than the bulk of other components. Although it contributes only a small fraction of total mass to the galaxy, galactic stellar haloes are considered excellent repositories of fossil evidence from the

epoch of star formation They are good laboratories for testing galaxy formation theories and revealing the specific formation histories of individual galaxies.

The stellar halo of the Milky Way was first discovered and characterized by a bunch of low-metallicity stars on elliptical orbits different from those of the Galactic disc [173, 144]. Johnston 2016 [123] proposed a classification system for stars in the stellar halo with three categories associated with different dynamical origins. First, *in-situ* stars, which are formed in orbits close to their current orbits. Second, *kicked-out* stars, which are formed in orbits different from their current ones. And finally, *accreted* stars, which are formed in smaller galaxies outdoes the dark matter halo they currently reside.

The classic model of the Milky Way stellar halo formation is that halo stars were born on eccentric orbits from radially-infilling gas clouds and they preserve their eccentricities today. This falls under the *in-situ* category. The *kicked-out* stellar halo stars are born within the inner galaxy on orbits that initially confined them to the disc but become heated to eccentric orbits by mergers [239, 183, 31, 111, 62, 23, 30] or by potential fluctuations from explosive feedback events [69, 68].

Recent evidence seems to suggest that the third category — *accreted* stars — is responsible for the majority of the stellar halo. Searle & Zinn 1978 [206] first discussed about this idea in a scenario that the halo is built up entirely from independent infalling fragments. Indeed, observations from large sky surveys confirm that the stellar halo has a complex structure and that the accretion of smaller galaxies is still ongoing [122, 24, 203]. The success of CDM/accretion-based models of stellar halo formation [41, 40, 54, 124, 50, 7, 77] in predicting the structures observed in the outer stellar halos of the Milky Way and M31 [18, 158] is also considered as one of the strongest evidence in favor of hierarchical galaxy-formation theory [112, 53, 21]. There is strong evidence that a significant amount of stars in the central stellar halo of the Milky Way appear to originate from at least one such accretion event [113, 152, 211, 52, 76, 163, 157, 165].

In this thesis, however, we focus on the *in-situ* population in the stellar halo, especially in the outer region. In stead of forming on eccentric orbits from *infalling* gas clouds, this population we observed in the simulations are created in feedback-driven molecular outflows. Star formation as a result of positive feedback has been reported in multiple recent observations [153, 88] but this is the first time it is connected with stellar halo formation. In our simulations, strong outflows occur at early times when the star formation is bursty and essentially disappear after disc settling. The contribution of this type of events to the stellar halo will depend in detail on star formation and galaxy-formation physics and it may offer a new way to test global galaxy formation models by local searches for such a population.

Chapter 2

Stars made in outflows may populate the stellar halo of the Milky Way

2.1 Introduction

Galactic outflows are common in the Universe and are crucial for understanding the enrichment of the intergalactic medium and galaxy evolution in general [227]. Molecular outflows with the densities required for star formation are common [1, 217, 196] and there is growing evidence that stars sometimes form in outflows. For example, Maiolino et al. 2017 [153] reported spectroscopic evidence of star formation inside of a galactic outflow at a rate exceeding $15 M_{\odot}\,\mathrm{yr}^{-1}$ in a $z \simeq 0.05$ galaxy. These authors go on to suggest that star formation may be occurring commonly in galactic outflows but that it has been missed due to inadequate diagnostics. Similarly, Gallagher et al. 2019 [88] have used the integral field spectroscopic data from MaNGA-SDSS4 to show that prominent star formation is occurring inside 30% of the galactic outflows in their sample. They also find that star formation inside outflows accounts for $5-30\%$ of the total star formation in the galaxy when detected, consistent with

another independent analysis from Rodríguez del Pino et al. 2019 [195].

One important feature of these observed star-forming outflows is that they are fast ($\sim 100 - 250$ km s^{-1}) but not so fast that they are unbound to the halo potential. While the outflow stars will not remain confined to the *central* galaxy, most will travel outward and then return on plunging, stellar-halo like orbits. If only $\sim 1\%$ of a $M_\star \simeq 5 \times 10^{10} M_\odot$ galaxy's stars are formed in (bound) radial outflows, this could contribute an appreciable fraction of a $\sim 10^9$ $M_\odot$ stellar halo typical of a Milky Way-mass galaxy today. In this paper, we show that stellar outflows do occur in FIRE-2 simulations[1] of Milky Way-mass galaxies and that they contribute to their stellar halos appreciably at $z = 0$, especially at large galacto-centric radius. Searches for and detections of such stars could provide a new tool for near-field cosmology to constrain feedback physics and to trace the outflow history of the Milky Way.

Galactic stellar halos are broadly understood to be good laboratories for testing ideas about galaxy formation and for revealing the specific formation histories of individual galaxies. The stellar halo of the Milky Way was first discovered and characterized by stars that exist on plunging elliptical orbits distinct from those of the Galactic disc [173, 144]. Later, authors such as Eggen, Lynden-Bell & Sandage [65, ELS hereafter] recognized that the timescales for stars on such orbits to exchange energy and angular momentum are long compared to the age of the universe, and used this as an opportunity to investigate the Galactic past.

Johnston 2016 [123] proposed a classification system for stars in the stellar halo with three categories associated with dynamical origin. First, *in-situ* stars, which are formed in orbits close to their current orbits. Second, *kicked-out* stars, which are formed in orbits unlike their current ones. And finally, *accreted* stars, which are formed in smaller galaxies outside the dark matter halo they currently occupy. The original proposal for the Milky Way's stellar halo formation by ELS falls into the *in-situ* category. ELS suggested that halo stars were born on eccentric orbits from radially-infalling gas clouds and that these stars preserve their

[1] See the FIRE project web site at http://fire.northwestern.edu.

eccentricity today. Stellar halo stars that are classified as kicked-out are born within the inner galaxy on orbits that initially confine them to the disc but become heated to eccentric orbits by mergers [239, 183] or by potential fluctuations from explosive feedback events [69, 68]. Kicked-out stars are usually envisioned to contribute to the inner stellar halo ($\lesssim 50$ kpc).

Today there is general agreement that the third category – accretion – is responsible for much of the stellar halo. This idea was first discussed by Searle & Zinn [206] in a scenario that bears strong anecdotal resemblance to the hierarchical galaxy formation prediction of modern ΛCDM. Indeed, one of the strongest pieces of evidence that structure formation is hierarchical on small scales is the success of CDM/accretion-based models of stellar halo formation [41, 40, 54, 124, 50] in predicting the coherent structure observed in the outer stellar halos of the Milky Way and M31 [18, 158]. It is likely that even the central stellar halo of the Milky Way is significantly populated by at least one such accretion event [**?** 152, 211, 52, 76, 163, 157, 165].

While there is substantial theoretical motivation from a ΛCDM context to believe that both accreted and kicked-out components populate the stellar halo, little work in the modern framework has discussed the *in-situ* population advocated by ELS. As discussed above, if star-forming outflows are indeed common, then there is good reason to think that *in-situ* stars populate the stellar halo after all. However, unlike the classic ELS conjecture, where halo stars are born on eccentric orbits from *inflowing* gas clouds, these *in-situ* halo stars are created in feedback-driven molecular *outflows*. According to the classification of Johnston 2016 [123], these stars are *in-situ* because they were created on orbits that are similar to those they inhabit today.

In what follows, we present an analysis of six high-resolution, ΛCDM cosmological zoom simulations of Milky Way-mass galaxies [229, 92, 199] from the FIRE-2 collaboration [120]. In these simulations, clustered supernovae feedback events regularly drive outflows of compressed shells of high-density gas. Occasionally, the accelerated regions are compressed to

densities above our star-formation threshold of 1000 cm^{-3} and become self-gravitating such that they trigger star formation within ~ 1 Myr of the acceleration. Stars formed in these outflows travel ballistically outward and eventually fall back into the halo on eccentric orbits. As we show below, this *in-situ* population can contribute as much as $20-40\%$ of the stellar halo at $r > 250$ kpc and may be distinguished from accreted stars based on their chemical and spatial characteristics.

The outline of this chapter is as follows. §2.2 provides an overview of our simulations and §2.3 details our method for identifying outflow stars, while §2.4 contains an investigation of their origin. §2.5 covers properties of outflow stellar halo. §2.6 discusses some caveats, and §2.7 provides our conclusions.

2.2 Simulations and Methods

The simulations that form the basis of our analysis are the hydrodynamic, cosmological zoom-in simulations run with the multi-method gravity plus hydrodynamics code Gizmo [116]. They utilize the FIRE-2 feedback implementation [120] and the mesh-free Lagrangian Godunov (MFM) method that provides adaptive spatial resolution while maintaining conservation of mass, energy, and momentum. The simulations include cooling, as well as heating from an ionizing background and stellar sources, including stellar feedback from OB stars and AGB mass-loss, type Ia and type II supernovae, and photo-heating and radiation pressure, the inputs for which are taken directly from stellar evolution models. Subgrid turbulent metal diffusion is also added, which can produce more realistic metallicity distributions in dwarf galaxies [75] but does not significantly change other general properties of the galaxies [118, 218]. Star formation occurs in molecular gas that is locally self-gravitating, sufficiently dense (> 1000 cm^{-3}) and Jeans unstable [137]. The default model requires that the thermal Jeans mass is below the particle mass (~ 7000 $M_\odot$), which is necessarily satisfied with the

Table 2.1: Simulations used in this work ordered by stellar mass. All simulations have baryonic mass resolution $m_b = 7,067 M_\odot$

Name	$M_{200\mathrm{m}}$ [$M_\odot$]	$R_{200\mathrm{m}}$ [kpc]	$M_\star$ [$M_\odot$]	R_{90} [kpc]	V_{max} [km·s^{-1}]
`m12m`	1.3e12	342	1.1e11	11.3	184
`m12f`	1.4e12	355	8.6e10	11.0	183
`m12b`	1.2e12	335	8.1e10	9.8	181
`m12i`	9.8e11	314	6.4e10	9.2	161
`m12c`	1.1e12	328	6.0e10	9.7	156
`m12w`	9.1e11	301	5.8e10	8.7	156

Columns include: (1) M_{200m}, R_{200m}: Mass and radius of the halo at $z = 0$ defined at an overdensity of 200 times the mean matter density. (2) $M_\star$: Stellar mass within 20 kpc of the center of the halo at $z = 0$. (3) R_{90}: radius enclosing 90% of M_{star}. (4)V_{max}: Maximum circular velocity.

Table 2.2: Simulations used in this work ordered by stellar mass. All simulations have baryonic mass resolution $m_b = 7,067 M_\odot$

Name	$M_{\star>20}$ [$M_\odot$]	f_{20}	$M_{\star>50}$ [$M_\odot$]	f_{50}	$M_{\star>150}$ [$M_\odot$]	f_{150}
`m12m`	5.9e9	0.05	2.1e9	0.04	1.4e8	0.09
`m12f`	8.7e9	0.05	1.9e9	0.06	3.1e8	0.07
`m12b`	5.8e9	0.05	1.9e9	0.07	2.0e8	0.24
`m12i`	2.8e9	0.08	9.8e8	0.07	9.8e7	0.17
`m12c`	1.9e9	0.12	7.3e8	0.13	1.6e8	0.13
`m12w`	2.4e9	0.10	6.0e8	0.14	4.8e7	0.34

Columns include: (1) $M_{>20}/M_{>50}/M_{>150}$: Mass of all the stars outside 20/50/150kpc from the center of the galaxy. (2) $f_{20}/f_{50}/f_{150}$: Mass fraction of stars outside of 20/50/150kpc that were born within 20 kpc from the center of the galaxy with birth radial velocity $> 200\mathrm{km\,s^{-1}}$.

virial criterion. We also explore a more conservative model where the thermal Jeans mass is required to be below 1000 $M_\odot$, the flow must be converging, and the virial criterion is smoothed over time to eliminate spurious cases where the SF criteria is only met in a transient sense. The star formation efficiency of the molecular component of particles that satisfy all star formation criteria is set to 100% per freefall time, ie. $\mathrm{SFR_{particle}} = \mathrm{m_{particle}} \cdot \mathrm{f_{mol}} \,/\, \mathrm{t_{ff}}$. Gas particles are converted to stars at this rate probablistically [129]. Note that this does *not* imply that the global efficiency of star formation (even on GMC-scales) is 100%. Self-regulated feedback limits star formation to $\sim 1 - 10\%$ per free-fall time [118, 174].

We focus on six Milky Way-mass galaxy simulations that are part of the "Latte Suite" [229, 92, 199, 197]. These were all simulated with identical resolutions: initial baryonic particle masses of $m_b = 7,067 M_\odot$, gas softening lengths fully adaptive down to $\simeq 0.5 - 1$ pc, star softening lengths to $\simeq 4$ pc, and a dark matter force softening of $\simeq 40$ pc. Table 4.1 summarizes the galaxy/halo properties. The galaxies are ordered by decreasing galaxy stellar mass at $z = 0$, from $M_\star = 1.1 \times 10^{11} M_\odot$ (`m12m`, top) to $M_\star = 5.8 \times 10^{10} M_\odot$ (`m12w`, bottom).

2.3 Stellar Birth Velocities and Radii

In order to characterize the origin of stellar halo material, we use methods described in Sanderson et al. 2018b [198] to trace all star particles back to their formation time. The birth radius $r_{\rm birth}$ is defined as the distance of a star particle from the center of the main progenitor host galaxy at the time of their formation.[2] We also measure the radial velocity at birth $V_{\rm rad}^{\rm birth}$ in order to roughly characterize the initial trajectory of stars at formation. We begin by exploring the content of two of our halos (`m12i` and `m12w`).

Figure 2.1 shows the birth radii ($r_{\rm birth}$) and current ($z = 0$) radii (r) for star particles in the vicinity of two of our simulations `m12i` (left) and `m12w` (right). We have removed all stars that are bound to satellite galaxies in the vicinity of the host, so only main-galaxy stars and halo stars are shown here. The particles are color coded by their ages, as indicated by the color bar, with the youngest stars in blue/purple and the oldest stars in yellow. The dashed black line in each panel traces $r_{\rm birth} = r$. This representation provides insight into the origin of various populations of the stellar halo.

One clear population visible in each panel of Figure 2.1 consists of central galaxy (disc)

[2]Note that Sanderson et al. 2018b [198] were motivated to distinguish accreted stars from stars born within the galaxy (they used $r_{\rm birth} < 30$ kpc). For this reason they used the term "*in-situ* " to include all stars that were formed within or near the galaxy – this is different than our dynamical definition of *in-situ* because it includes both stars that are "kicked-out" by mergers and those that we identify as forming in outflows.

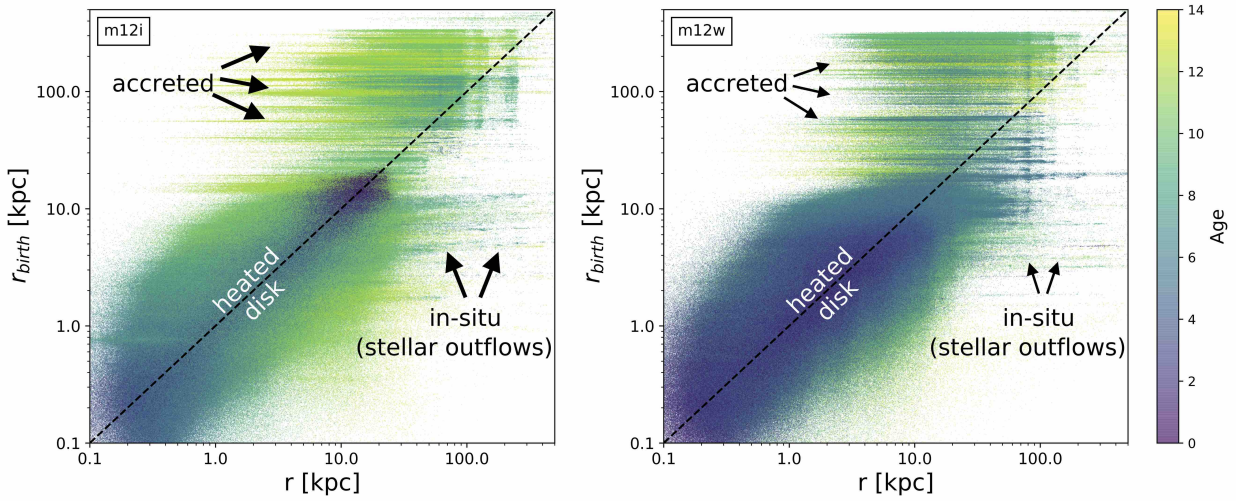

Figure 2.1: Star particle birth radius vs. current radius color coded by stellar age for `m12i`(left) and `m12w` (right). All the star particles that are bound to satellites have been removed from our sample. The dashed black lines in each panel trace $r_{\rm now} = r$. Three populations are distinguishable here. 1) Accreted stars: these populations dominate at large birth radii ($\gtrsim$ 30 kpc) and make thick horizontal bands that extend mostly to the left of the one-to-one line ($r_{\rm birth} > r$). There is a less dominant population of accreted stars that are flung out after their birth galaxies are destroyed to present radii ($r > r_{\rm birth}$). These stars sometimes pile up in shells of constant r, which is the origin of vertical banding (e.g. at $r \simeq 200$ kpc in `m12i`). 2) Heated/disc stars: these populations mix to create the dense sequence of mostly young stars that is uniformly scattered about the one-to-one line at small radii ($r \lesssim 30$ kpc. Heated stars are perturbed to both smaller and larger radius. They sample a continuous population of pre-heated disc stars and leave no horizontal bands. 3) *in-situ* halo stars: this population is characterized by distinct horizontal bands with characteristic birth radii within the main galaxy ($r_{\rm birth} \lesssim 10$ kpc) that today have $r > r_{\rm birth}$ as large as ~ 500 kpc. Unlike the accreted stars, the *in-situ* bands extend to the right of the one-to-one line, which is indicative of an outflow.

stars at $r \lesssim 20$ kpc, which scatters about the $r = r_{\rm birth}$ line. Stellar migration and heating processes have driven stars to exist at radii that are either smaller (to the left of the line) or larger (to the right of the line) than their birth radii.

A second population is that of accreted stars (most visible at $r_{\rm birth} \gtrsim 30$ kpc), which are evident as horizontal bands that extend mainly to the left of the one-to-one lines. The leftward extension means that they were born at a much greater galactocentric distance from the radius where they currently reside. Stars in this population were formed in smaller galaxies that were accreted and incorporated into the stellar halo of the main host. Note that in some cases these horizontal bands have less-prominent extensions to the right of the one-to-one line (with $r > r_{\rm birth}$). These are stars flung out to large radii after their birth galaxies are destroyed. In a few places we see vertical bands (e.g. at $r \simeq 100$ kpc and 200 kpc in `m12i` and at $r \simeq 80$ kpc in `m12w`). We have studied these bands and find that they are "shells" left over from galaxy mergers that pile up at orbital apocenter.

Most relevant to this work is a third population of halo stars that can be seen as distinct horizontal bands with characteristic birth radii within the main galaxy ($r_{\rm birth} \lesssim 20$ kpc). Unlike the accreted stars, these bands (labeled "*in-situ* ") exist primarily to the right of the one-to-one line ($r > r_{\rm birth}$). This population is intriguing because it consists of star particles that are now at much greater galactocentric distance relative to their birth places; the banding at near-constant[3] $r_{\rm birth}$ suggest multiple populations with unique episodes of origin. Note that there are stars that were born within 20 kpc that now populate distances out to $r \sim 500$ kpc.

Figure 2.2 demonstrates that most of these *in-situ* stars that now exist at large radii were indeed born with large positive (outward) radial velocities $\gtrsim 150\,{\rm km\,s^{-1}}$, indicative of outflow.

[3]Some of these bands show a slight slope towards larger $r_{\rm birth}$ at increasing $z = 0$ radius. As we discuss below, these *in-situ* stars are born in dense, shell-like outflows. The stars that form last have emerged from gas that has had more time to be accelerated and this pushes them towards slightly larger birth radii and more extended orbits today.

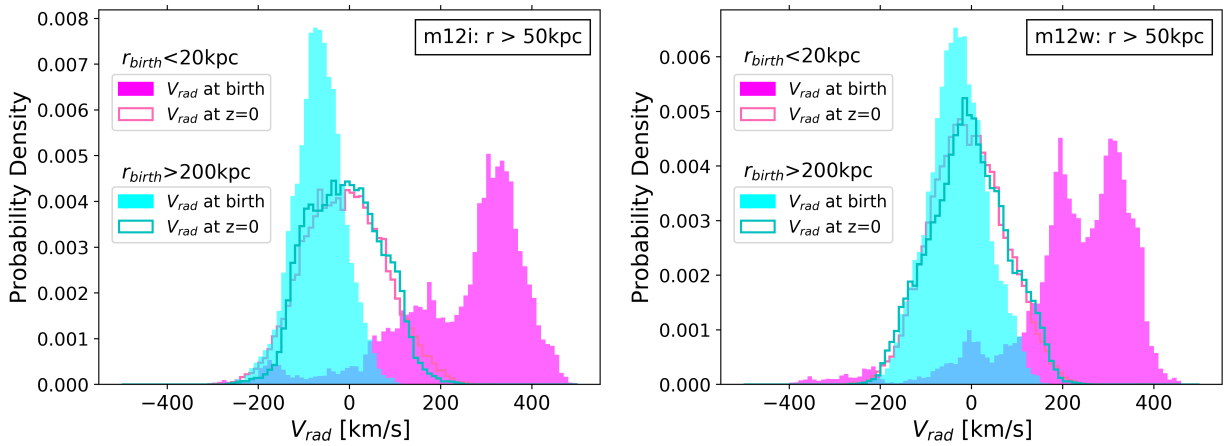

Figure 2.2: Radial velocities at birth (shaded) and at the present time (lines) of $z = 0$ for outer stellar halo stars (with current radii $r > 50$ kpc) in `m12i` (left) and `m12w` (right). The shaded magenta histograms show birth velocities of the subset of halo stars that were born within the central galaxy ($r_{\rm birth} < 20$ kpc) while the shaded cyan histograms show birth radial velocities for accreted halo stars ($r_{\rm birth} > 200$ kpc). We see that outer halo stars that were born within the central galaxy tend to have been created with large positive radial velocities, which means that they were born outflowing. The accreted halo stars have a bias to have been born with negative radial velocity, consistent with an infalling population. The radial velocities of these two groups are quite similar at $z = 0$ (open histograms). While the accreted and *in-situ* populations have different origins, their kinematic properties today do not readily reveal an observable difference.

The shaded magenta histograms show $V_{\rm rad}^{\rm birth}$ for outer halo stars with $r > 50$ kpc that were born within the central galaxy region $r_{\rm birth} < 20$ kpc for both `m12i` (left) and `m12w` (right). Compare these distributions to the shaded cyan histograms, which show birth radial velocities for stars at the same current radius ($r > 50$ kpc) that were born at large radii $r > 200$ kpc. These stars tend to be slightly infalling at birth, which is consistent with an accreted population. Interestingly, these two populations, which had significantly different kinematic properties at formation, today have radial velocity distributions that are very similar (open histograms). This would be expected for stars that have similar apocenters orbiting in the same potential for several dynamical times. §2.4.2 provides an exploration of the physical origin of these stellar outflows and demonstrates that they tend to occur during bursty star formation episodes, specifically in conjunction with super-bubble winds that accelerate dense molecular gas that goes unstable to star formation after being accelerated outward.

The definition of "outflow" is inherently subjective. For the sake of concreteness, in what follows we will identify stars that formed in outflows to be represented by star particles that originated within the central galactic region, $r_{\rm birth} < 20$ kpc, and that had large, positive velocities at the time they were created: $V_{\rm rad}^{\rm birth} > V_{\rm O}$. For most of our analysis will use $V_{\rm O} = 200\,{\rm km\,s^{-1}}$ as a conservative choice based on the results shown in Figure 2.2 and similar analyses done for our other four halos. As we discuss in §2.5.3, more than 95% of stars that exist in the central disc at $z = 0$ were born with velocities $V_{\rm rad}^{\rm birth} < 150\,{\rm km\,s^{-1}}$. Based on this we also explore how our results change if we adopt $V_{\rm O} = 150{\rm km\,s^{-1}}$. Our qualitative conclusions do not change with this choice, though the fraction of halo stars in the inner halo identified as originating in outflows does increase as $V_{\rm O}$ decreases.

We show below that our adopted strategy for identifying stars born in outflows – stars with small birth radius and large positive birth velocity – seems to select stars that are born within dense gas that has been accelerated in feedback-driven winds from the main galaxy. In principle, however, the selection does not preclude other possibilities. For example, one could

imagine stars born within a gas-rich satellite that experiences a starburst episode just after pericenter crossing. On rare occasions, such stars could meet our selection criteria and then become liberated into the stellar halo after the satellite is tidally disrupted. We have looked for instances of these events and find them to be rare. As discussed in subsequent sections, the outflow stars we identify tend to be metal-rich (like the central galaxy), with higher metallicity than the vast majority of satellite galaxies, rendering this possibility statistically unlikely.

With this definition of outflow stars in hand, we can ask how they populate the stellar halos of our galaxies. Figure 2.3 shows that they contribute significantly, especially at large radius. The solid black lines in each lower panel present the differential density profiles of all stars in `m12i` (left) and `m12w` (right). Stars bound to satellite galaxies have been removed. For reference, the black dashed lines are best-fit power-law slopes ($\rho \propto r^{-\alpha}$) that fit the profile of all the halo stars in each galaxy within $r = 10 - 85$ kpc. The solid blue lines show the density profiles of stars born in outflows (using $V_{\rm O} = 200 {\rm km\,s^{-1}}$), with corresponding power-law fits within $10 - 85$ kpc shown as dashed lines. We see that the outflow profiles tend to be flatter than the total stars, such that the fraction of all stars born in stellar outflows tends to rise with galacto-centric radius. The upper panels show the fraction of stars identified as being born in outflows as the ratio of the two density profiles (solid blue). We see that outflows contribute a substantial fraction to all the halo stars at large radius in these two halos ($\sim 10 - 50\%$ beyond 50 kpc). The dotted lines show the fraction for halo stars identified with $V_{\rm O} = 150 {\rm km\,s^{-1}}$. With this selection, the fraction identified as outflow is slightly higher within 50 kpc but remains similar at larger radius.

The solid lines in Figure 2.4 show the fraction of stars born in outflows for all six halos, defined in the same way as the solid lines in the upper panels of Figure 2.3. The systems are colored from lowest to highest in the stellar mass of the central galaxy, starting with `m12w`, which has $M_\star = 5.6 \times 10^{10} M_\odot$ and proceeding to `m12m` with $M_\star = 1.1 \times 10^{11} M_\odot$. Four of

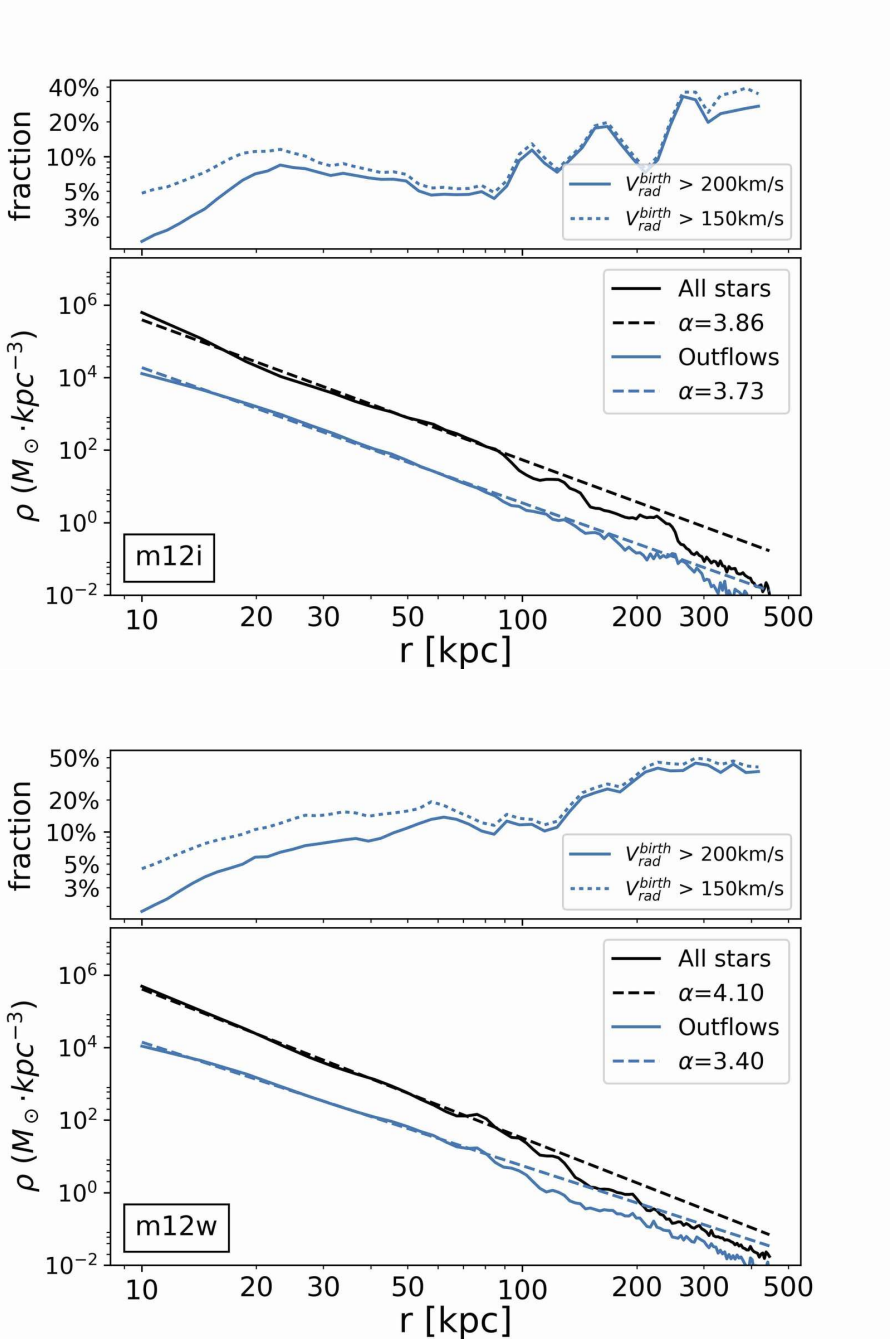

Figure 2.3: Stellar density profiles for all stars (black) and for stars born in outflows (colored, defined as $V_{\rm rad}^{\rm birth} > 200\,{\rm km\,s^{-1}}$ and $r_{\rm birth} < 20$ kpc) as a function of radius for `m12i` (top) and `m12w` (bottom). The dashed lines illustrate power-law fits ($\rho \propto r^{-\alpha}$) done for $r = 10 - 85$ kpc in each component and then extrapolated. The top sections of each panel show the fraction of stars born in outflows, $\rho_{\rm outflow}(r)/\rho_{\rm total}(r)$, as a function of present radius r for two ways of identifying outflow: $V_{\rm rad}^{\rm birth} > 200\,{\rm km\,s^{-1}}$ (solid) and $> 150\,{\rm km\,s^{-1}}$ (dotted), both with $r_{\rm birth} < 20$ kpc. The fraction of stars born in outflows can become quite substantial at large radius, reaching $\sim 25 - 50\%$ of all stars at $r > 250$ kpc, while at 50 kpc the fraction is fairly modest $\sim 5 - 10\%$.

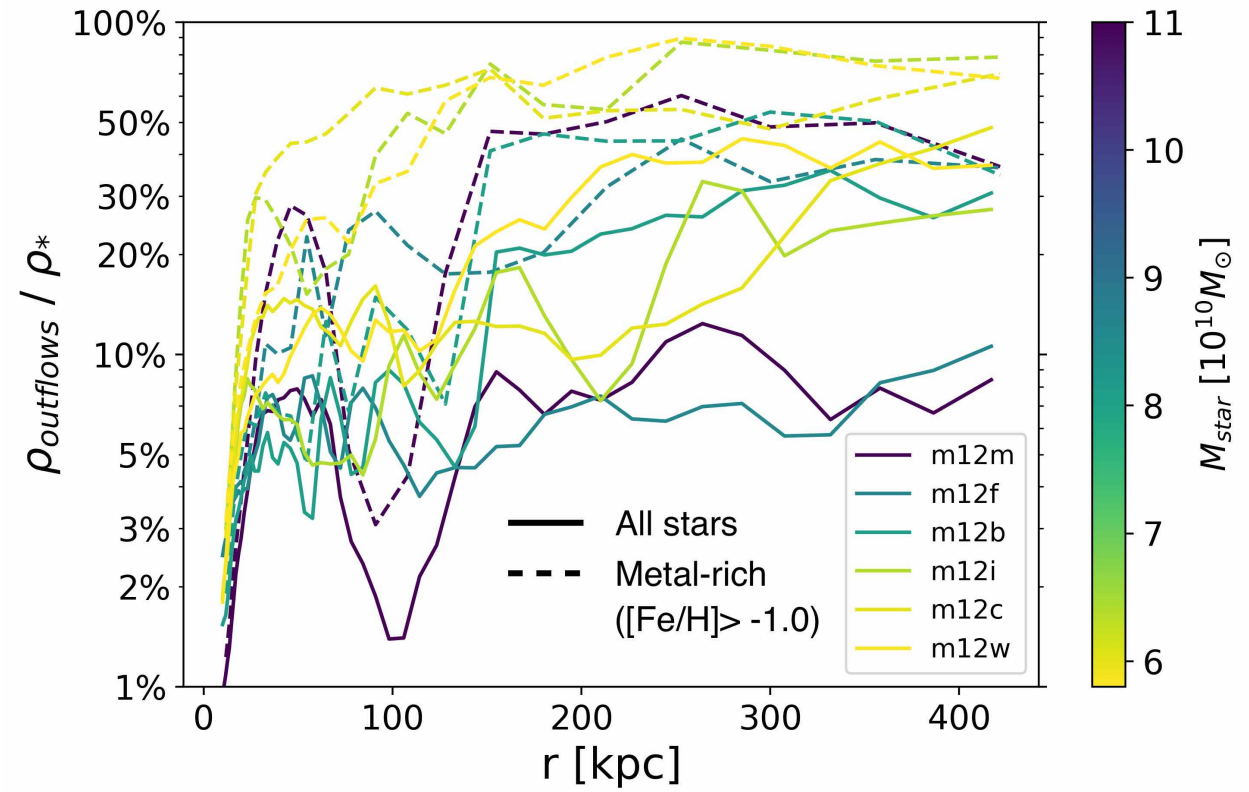

Figure 2.4: The fraction of stars born in outflows as a function of present radius for all six simulations color coded by central galaxy stellar mass. Outflow stars are defined to be those with $V_{\rm rad}^{\rm birth} > 200\,{\rm km\,s^{-1}}$ and $r_{\rm birth} < 20$ kpc. The solid lines show the result for all stars while the dashed lines only calculate the ratio the density profiles of the metal-rich ([Fe/H] > -1.0) stars born in outflows to the density profile of all metal-rich. The fraction of metal-rich stars born in outflows can reach $> 50\%$ at $r > 150$ kpc for many systems.

the six have $\gtrsim 20\%$ of the stars in their outer (> 250 kpc) stellar halos composed of stars that were formed in radial outflows from the main galaxy. The two lowest outflow fractions happen to correspond to the two most massive galaxies `m12m` and `m12f`, but given the small sample size is it not possible to say if this is representative of a mass trend or simply halo-to-halo scatter. Both of these galaxies experience late-time mergers that help populate the outer halo with accreted stars. This may be the reason why the outflow fraction is small – it is that the accreted mass is larger than average, rather than the outflow mass being smaller than average. The dip in outflow fraction at ~ 100 kpc in `m12m` is associated with a bump in the total stellar profile at that radius that comes from a remnant of a fairly large, recently-accreted dwarf galaxy that has deposited stars in that area.

The dashed lines in Figure 2.4 show the fraction of metal rich ([Fe/H] > -1.0) halo stars born in outflows as a function of radius. We see that among the most metal rich stars in the outer stellar halo, outflows typically dominate. We discuss the origin of this difference in §2.5.2 and §2.5.3.

Table 2.2 provides more detailed information on the stellar halos of each of our galaxies. In the six columns we list the total stellar mass and fraction of that mass in outflow stars outside of various radial cuts ($r > 20$, 50, and 150 kpc). Note that the total mass of outflow stars outside of 20 kpc ranges from $\sim 10^8 - 10^9$ $M_\odot$ and that this makes up $\sim 5 - 10\%$ of all stars in the stellar halo beyond 20 kpc.

2.4 Origin of stellar outflows

In this section we discuss the identification of outflow stars in our simulations and provide a brief exploration of their origin.

As seen in Figure 2.1, the *in-situ* component of outer ($r > 50$ kpc) halo stars in `m12i` and

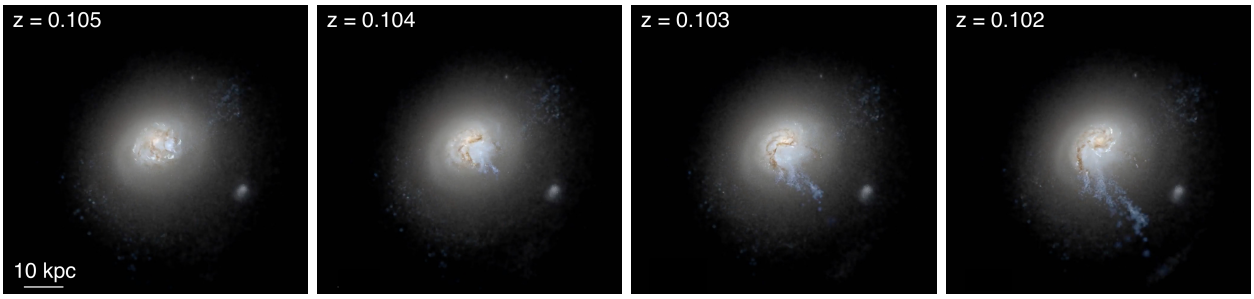

Figure 2.5: Star-forming outflows developing in halo `m12w` over a ~ 40 Myr period around redshift $z \simeq 0.1$ (from left). These are mock *Hubble Space Telescope* u/g/r composite images created as described in Hopkins et al. 2018 [120] and span 80 kpc on a side. We see several prominent plumes of young blue stars that were born in gas that was originally rotating and then blown radially outward just prior to star formation. The bulk of these stars are bound to the main halo and should eventually fall back on radial orbits indicative of halo stars.

`m12w` show multiple populations with narrow horizontal bands of roughly discrete birth radii. This is consistent with distinct outflow events and would not be expected for stars that were kicked out in merger events or heating. Figure 2.2 shows that these stars are born with large positive radial velocities, which is again consistent with radial outflow and not stars that were kicked out after formation. By examining the formation histories of our galaxies, we find that these stars tend to be born in shells of gas compressed and accelerated in discrete outflow events. We provide examples below. These events are quite obvious in visualizations and movies. [4]

2.4.1 Example Stellar Outflow Events

Figure 2.5 presents mock u/g/r composite images of a stellar outflow developing over 40 Myr in `m12w`. Note that this image shows stars and dust only (not gas). A stream of blue (young) stars extends outward towards the lower right corner of the image as time progresses from left to right. These stars were born in dense gas that was rotating within the disc and subsequently accelerated in an outflow prior to star formation.

[4]For movies and images of Milky Way and Andromeda - like systems in FIRE2 simulations, see: `http://www.tapir.caltech.edu/~phopkins/Site/animations/a-gallery-of-milky-way-/`

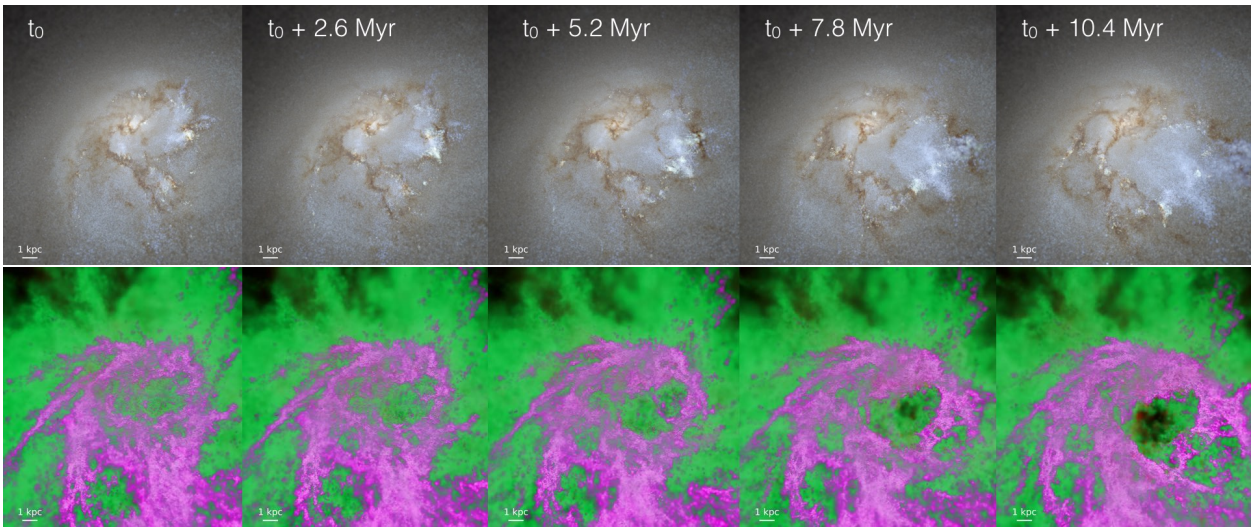

Figure 2.6: An outflow event in stars (upper) and gas (lower) developing in halo `m12w` over a 10.4 Myr time period. The left most panel starts at time t_0 (1,342.4 Myr before $z = 0$) and progresses forward in time in steps of 2.6 Myr from left to right. Each image is 20 kpc square. The upper panels are u/g/r composites as in Figure 2.5. In the lower panel, magenta is cold molecular/atomic gas (< 1000 K) and green is warm ionized gas ($10^4 - 10^5$ K). We see that stellar outflows develop along with cold-gas outflows, as stars form from compressed gas that has been accelerated outward at the edges of evacuated super-bubbles.

Figure 2.6 shows a zoomed-in (20 kpc) region around `m12w` as this prominent outflow develops over the first 10.4 Myr of its evolution. The upper panels show a false-color visualization and lower panels present cold (pink) and warm (green) gas at the same epochs. Clustered supernovae events are driving bubbles of cold-gas outflows in the bottom panels. Stellar outflows are apparent at the edges of these bubbles where compressed, radially-accelerated gas is converted into stars.

Figure 2.7 focuses on the beginning of same outflow event in `m12w`, with more information provided. The panels are time-ordered from left to right, beginning at a time roughly 1 Myr earlier than the first panel of Figure 2.6. The top row shows all gas particles within a 10 by 10 kpc region around the central galaxy, color coded by radial velocity, with red indicative of radial gas outflow according to the color bar. The second row shows the surface density of that gas color coded according to the bar on the right. The third row plots *new stars* that were formed between the snapshots shown (i.e. those formed in the previous ~ 3 Myr) color

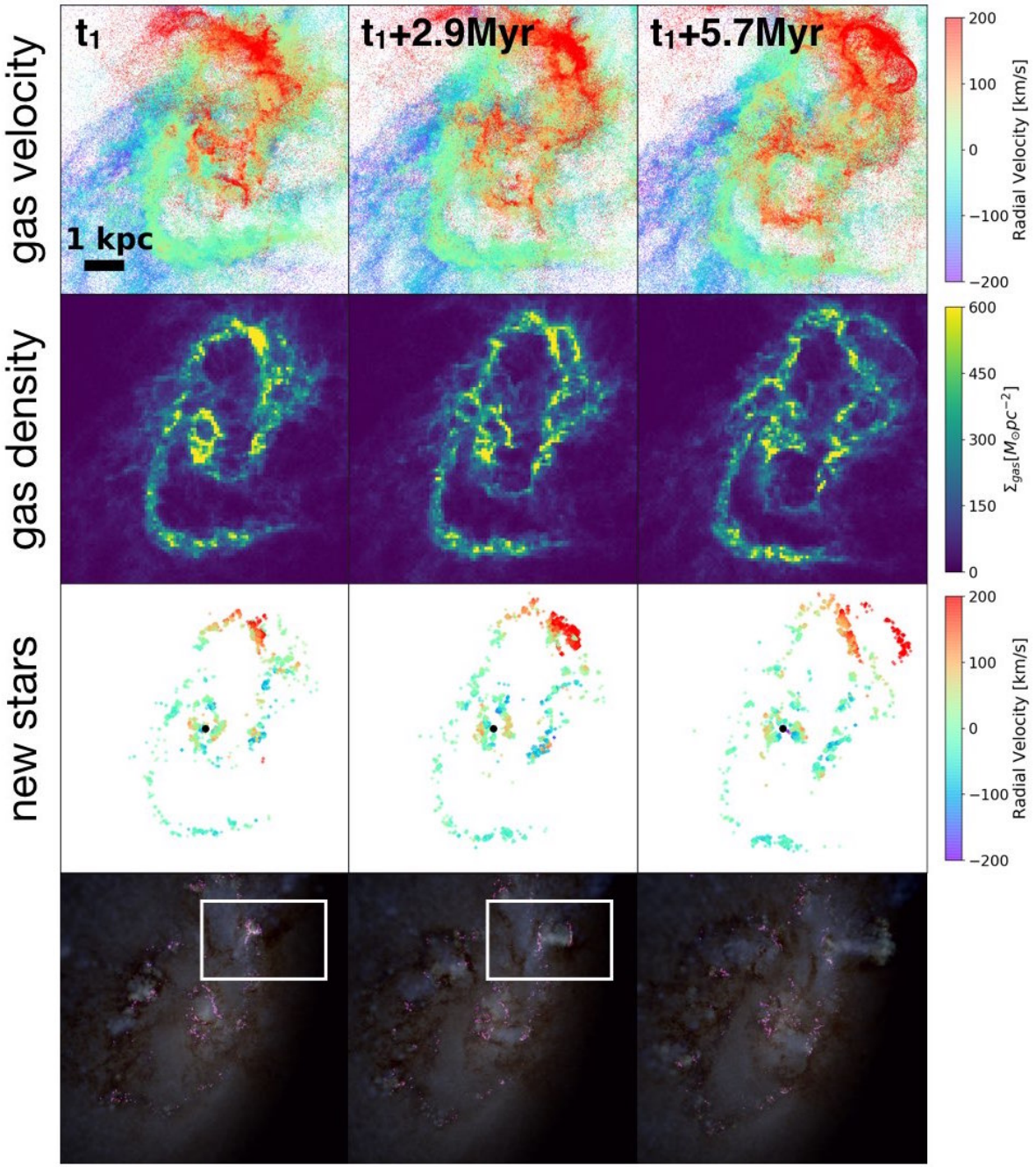

Figure 2.7: Development of a stellar outflow in `m12w` starting starts at time t_1 (1,343.5 Myr before $z = 0$) and progressing in ~ 2.9 Myr timesteps from left to right. The top row shows gas particles within a 10 kpc region of the galaxy color coded by radial velocity, with red indicative of fast radial outflow. The second row shows gas surface density and the third row shows new stars (formed within the previous 2.9 Myr) color coded by radial velocity. The red regions in the third row are young stars that are outflowing, which overlap spatially with high-density gas at the edges of expanding superbubbles. The lowest set of images show color composite similar to those shown in Figure 2.5, now with pink overlaid to trace star formation rate density. A clear pair of stellar outflow shells is being generated in the white-boxed regions (enlarged in Figure 2.8) in the upper left portion of the galaxy.

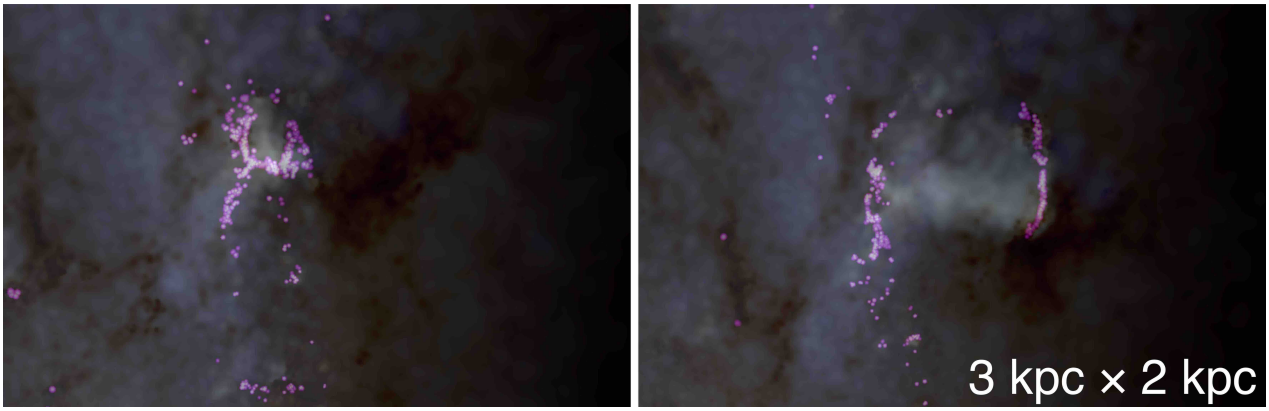

Figure 2.8: Zoomed-in mock *Hubble Space Telescope* u/g/r composite images of the first-two panels in Figure 2.7, illustrating an expanding bubble of triggered star formation (pink). Each image spans ~ 3 kpc in width and ~ 2 kpc in height.

coded by radial velocity, such that the red points are indicative of young stellar outflows. The dense gas that spawns these stars accelerates over ~ 1 Myr timescales just prior to star formation. The stars then travel ballistically outward. The bottom row shows the galaxy as a mock u/g/r composite image with the star formation rate density overlaid in pink. We see star formation (pink) work to both drive outflows and generate new outflowing stars at the edges of an expanding bubble. Figure 2.8 zooms in on the first two panels of this image to show a particularly prominent stellar outflow shell developing. Stars are clearly forming at the edge of a super bubble that is expanding at high radial velocity.

2.4.2 Stellar Outflows and Total Star Formation

Figure 2.9 provides a global view of how these stellar outflows track star formation with time. The six panels show star formation rates averaged over 10 Myr as a function of lookback time in each galaxy, presented in the order of increasing main-galaxy stellar mass from upper left to lower right. The top panels give the total star formation rate of stars that born in the main galaxy ($r_{\rm birth} < 20$ kpc), while the bottom panels show the formation rate only of stars that we identify as being created in outflows ($r_{\rm birth} < 20$ kpc and $V_{\rm rad}^{\rm birth} > 200\,{\rm km\,s^{-1}}$). Generally, our galaxies have bursty star-formation histories at early times and settle into

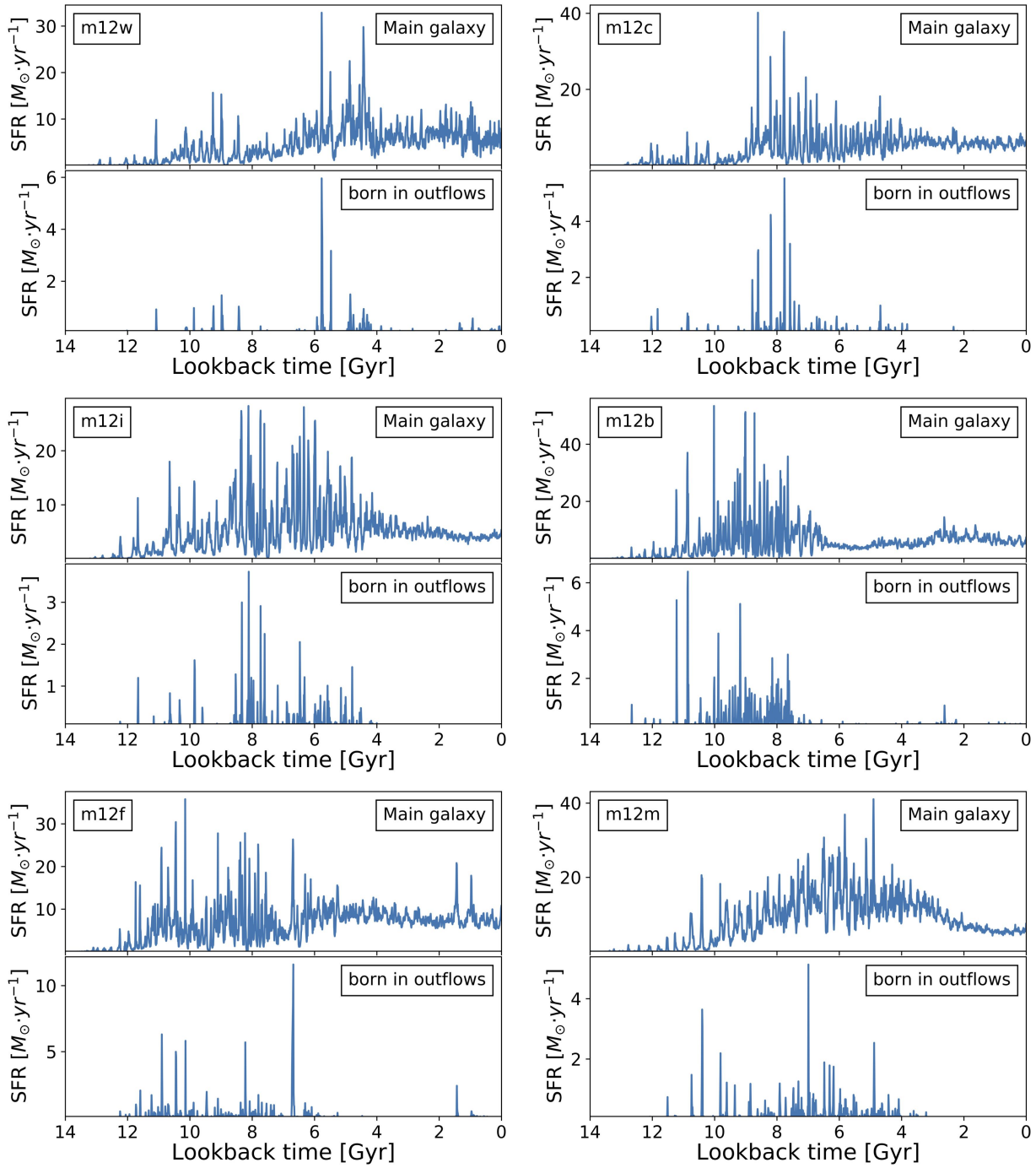

Figure 2.9: Instantaneous star formation rates for the main galaxy (top panels) compared to stellar outflow star formation rate (bottom panels) for all six of our simulated galaxies, as indicated. Star formation rates are averaged over 10 Myr. Outflows are defined as stars that were formed with $r_{\rm birth} < 20$ kpc and $V_{\rm rad}^{\rm birth} > 200\,{\rm km\,s^{-1}}$. The galaxies are ordered from lowest to highest in total stellar mass from upper left to bottom right. Stellar outflows tend to correlate with bursty star formation and become rare at late time as star formation becomes more constant. Overall, stars made in outflows account for only $\sim 1\%$ of all stars formed in the galaxy, but during some starbursts the instantaneous outflow fraction can be as high as $\sim 20 - 30\%$.

more steady star formation over the last ~ 4 Gyr. Stellar outflows are clearly correlated with bursty star formation and become rare at late times when the main galaxy's star formation rate becomes less bursty. In the FIRE simulations, strong outflows occur during the bursty phase, and essentially disappear after disc settling [162, 8, 216]. This suggest that most of the stars born in outflows form before disc settling, which occurs at different times for different galaxies. The outflow event we have chosen to show in the previous section is fairly isolated, which provides us a particularly clean example. The other events that we see, especially those during very bursty star formation episodes appear to be triggered by similar feedback events. The few stellar outflow events that do occur at late times are correlated with brief periods of elevated star formation in the main galaxy.

Surprisingly, while the fraction of all stars that form in outflows is small compared to the total stellar mass of the system ($\sim 1\%$ overall), during starbursts, the instantaneous fraction of stars born in outflows can be as high as $\sim 20 - 50\%$. Interestingly, this result is broadly consistent with the observations in Gallagher et al. 2019 [88], who find that star formation inside outflows accounts for $5 - 30\%$ of the total star formation when detected. Since the focus of this paper is on the $z = 0$ stellar halos of Milky Way-mass galaxies, we defer a more detailed comparison to observation for future work. [5]

One thing worth noting here is that the discs in the runs we study here have "hotter" stellar velocity dispersion than the Milky Way and are more comparable to M31 (Sanderson et al. 2018a, Figure 2[199]). Nevertheless, as we discuss below, outflow stars contribute only small fractions to thick-disc type populations and negligibly to thin-disc stars, and therefore are unlikely to have significant influence on, for example, the disc kinematics at $z \sim 0$, especially for young stars.

[5] We note that the $z = 0$ global star formation rates of our galaxies ($4 - 10\,M_\odot$/yr) are somewhat higher than estimates for the Milky Way [1-4 $M_\odot$/yr 143, 240]. However, most of them are relatively steady at late times (like the Milky Way). These systems lack recent outflow activity, and we would expect that the Milky Way would be similar.

It is clear from Figure 2.9 that the bulk of stellar outflow activity happened at lookback times greater than $\sim 4-8$ Gyr ago. Since halo dynamical times are ~ 2 Gyr at the virial radius, there is ample time for most of these outflow stars to have traveled outward and fallen back in to the main halo. We expect, therefore, that most of these stars will be fairly uniformly distributed in the halo. However, the small number of late-time outflow events (that occur within the last ~ 2 Gyr) may preserve some spatially coherent structure. In the following section we investigate these issues in more detail and explore observational differences between outflow stars and other stellar halo material.

2.5 Outflow Stars in the Inner and Outer Halo

2.5.1 The Outer Stellar Halo: Phase Space Structure

Figure 2.10 presents orbit diagrams ($V_{\rm rad}$ vs. r) and face-on spatial distributions of halo stars in `m12i` (top set) and `m12w` (bottom) at z=0. The color bars map to stellar age for the radial velocity figures (top) and to metallicity for the spatial figures (bottom). The left columns include all stellar particles, the middle columns include only *in-situ* stars that were born within the central region of the galaxy ($r_{\rm birth} < 20$ kpc) and with large positive radial velocity ($V_{\rm rad}^{\rm birth} > 200\,{\rm km\,s^{-1}}$). The right panels include only accreted stars that were born beyond 200 kpc of the central galaxy for comparison. We have removed all stars bound to satellite galaxies in these diagrams.

There are significant differences between outflow stars and accreted stars in both the orbital diagrams and spatial structures. While overall the velocity distributions are quite similar at $z = 0$ (see the open histograms in Figure 2.2), the phase-space structure is different. Substructures, visible both spatially and in the orbital diagrams in Figure 2.10, are dominated by accreted stars born at large radius in distinct dwarf galaxies. These structures

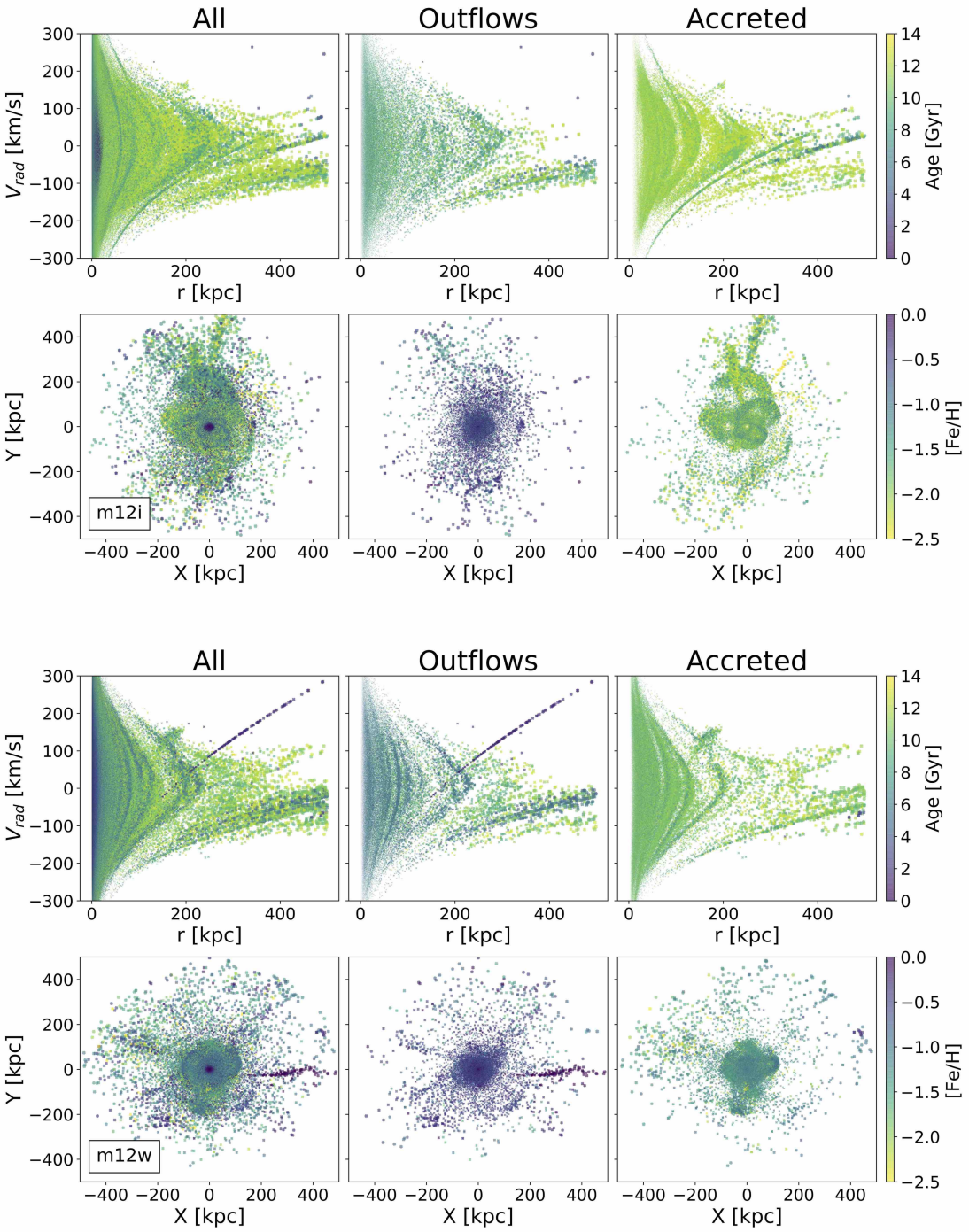

Figure 2.10: Phase space structure of `m12i` (top set) and `m12w` (bottom set). Top rows depict stellar radial velocity vs. radius, color coded by age. Bottom rows show the spatial distribution of star particles color coded by metallicity. Stars bound to satellite galaxies have been removed. The left panels includes all star particles. The middle panels includes only outflow stars identified to have $r_{\rm birth} < 20$ kpc and $V_{\rm rad}^{\rm birth} > 200\,{\rm km\,s^{-1}}$. The right panels include only stars with $r_{\rm birth} > 200$ kpc (accreted). The *in-situ* stars tend to be more metal-rich and more smoothly distributed in the stellar halo than accreted stars. A recent, metal-rich stellar outflow is visible in purple in the bottom set of `m12w`.

offer important constraints on the accretion history. The *in-situ* outflow population shows many fewer structures and is much more smoothly distributed. While the orbital properties of accreted and outflow halo stars are *not* particularly distinct, the phase-space structure of the two populations is. Although one might have expected outflow stars to follow more radial orbits, we find that by the time most of them have traveled out and fallen back in to the stellar halo at $z = 0$, they end up on similar orbits as the rest of the stellar halo.

The main reason why outflow stars are more smoothly distributed is that the outflow events tend to occur long enough ago (Figure 2.9) that they become well mixed in the halo potential. One counter example to this trend is seen in `m12w`, which had an outflow event at $z \simeq 0.1$ that remains visible as a blue plume at $z = 0$. In the bottom middle panel of Figure 2.10, we see this as an outflowing stream of metal-rich stars at $Y \simeq 0$ that extends from $X \simeq 0$ to 500 kpc. The same stars make up the young streak of particles that have increasing radial velocity with distance in the panel above it. This behavior is characteristic of an outflow because stars that are liberated from a tidally-destroyed galaxy will tend to trace a characteristic orbital pattern, with radial velocity decreasing in magnitude with distance from the main galaxy (as seen in the upper-right panels). Instead, the stars in this stream are moving more quickly at larger radius, because of the birth velocity gradient[6]. They were born within 20 kpc of the galaxy $t_{\rm age} \simeq 1.34$ Gyr ago and the most distant ones are still on their way out. We find that $< 10\%$ of the stars in this young plume are unbound, so that the bulk of these stars are destined to return and inhabit the stellar halo in the future. In fact, the upper panels for `m12w` show that stars in the stream with $r \lesssim 150$ kpc have already started to fall back in with negative radial velocity.

Of the six halos in our simulation sample, `m12w` and to a lesser extend `m12b` and `m12f` have visible outflow streams in phase space at $z = 0$. In both cases, the plumes are less prominent

[6]As we have discussed above, these stars are born in accelerated gas outflows. The stars that form last have emerged from gas that has had more time to be accelerated and this creates a velocity gradient among the stars that have formed.

than the big plume in m12w. The vast majority of outflow stars in all six halos have smooth phase-space structure.

Figure 2.10 also demonstrates that the outflow populations in m12i and m12w are both more metal-rich and moderately younger than the bulk of the stellar halo at large radius. The age difference is not systematic among our six runs. Halos m12b, m12c, and m12f all have outflow halo populations that are slightly older than the accreted halo stars. This is perhaps not unexpected since the outflow star formation rates shown in Figure 2.9 suggests that these three galaxies have more early-time outflow star formation than the others. However, in all six runs, outflow stars in the outer stellar halo are chemically distinct. We discuss this difference in the next subsection.

2.5.2 The Outer Stellar Halo: Chemical Abundances

Figure 2.11 illustrates [Mg/Fe] versus [Fe/H] distributions for outer halo stars ($r = 50 - 200$ kpc) for all six halos as indicated, ordered from upper left to bottom right with increasing central galaxy stellar mass. The different colors are used to represent different populations, with blue showing accreted stars with $r_{\rm birth} > 200$ kpc and red showing outflow stars identified as stars born within 20 kpc of the main galaxy and with large positive radial velocity ($V_{\rm rad}^{\rm birth} > 200\,{\rm km\,s^{-1}}$). The outflow population tends to be more alpha-enhanced at fixed iron abundance, and typically more iron-rich than the accreted halo.

This difference may provide a way to distinguish outflow-produced halo stars from their accreted counterparts. Specifically, outflow stars born within the main galaxy are inherently metal-rich, unlike outer halo stars from accreted, low-mass dwarfs, which tend to be lower metallicity [40, 124]. These outflow stars also form in bursts, which pushed them towards higher α element abundance at fixed [Fe/H]. Elements like Mg are produced in core-collapse supernovae on timescales that are significantly shorter than SNe Type Ia, which produce

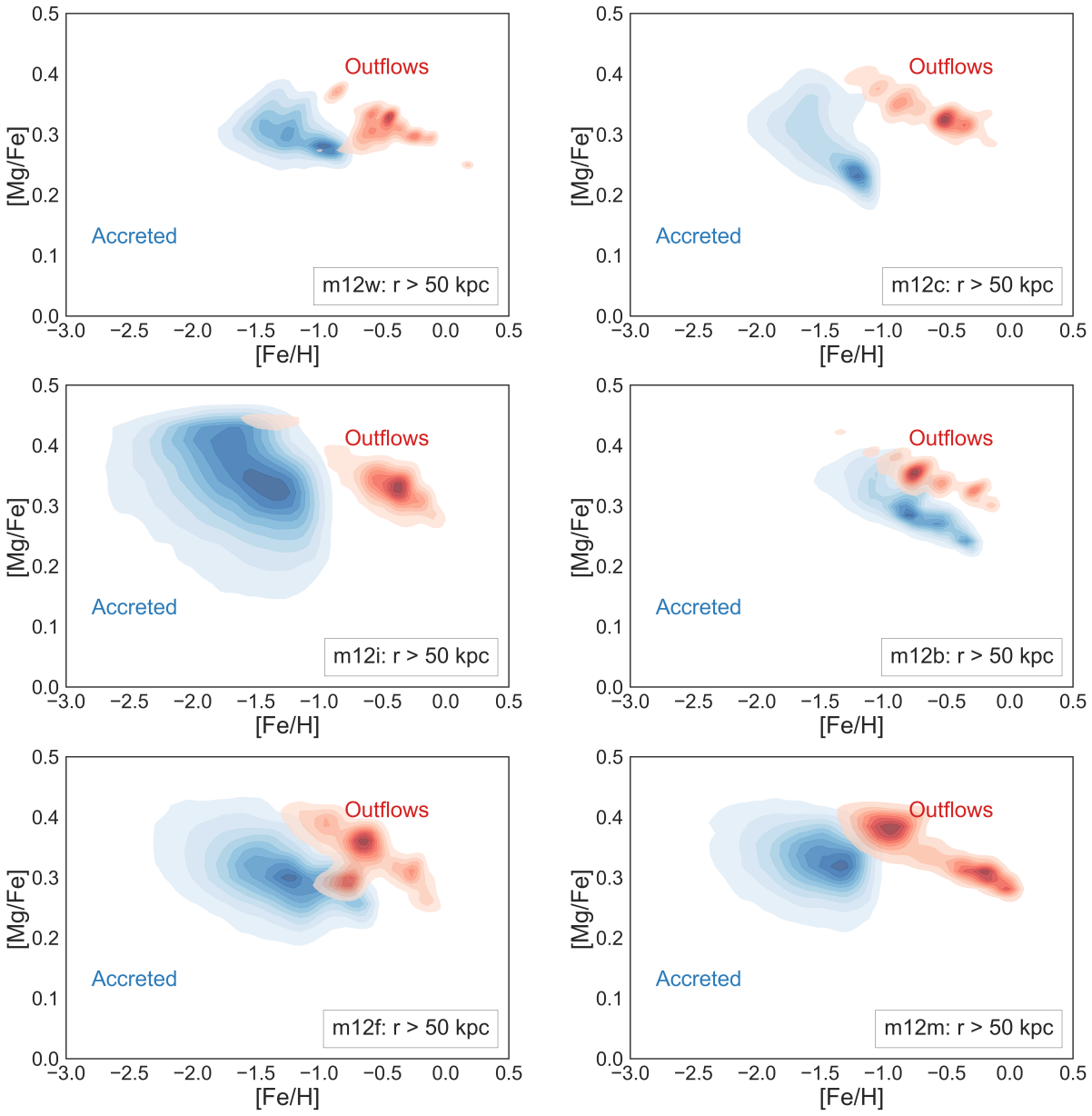

Figure 2.11: Kernel density estimate in [Mg/Fe] versus [Fe/H] for outer halo stars with $r = 50 - 200$ kpc in each system. The galaxies are ordered from lowest to highest in total galaxy stellar mass from upper left to bottom right. The red region shows the outflow population and the blue one shows the distribution for accreted stars born outside of 200 kpc.

the majority of iron [194, 154]. The accreted dwarfs that form the outer stellar halo tend to have longer periods of star formation, and are less α enhanced at fixed iron abundance than stars formed in bursts.

Note that, while stars from accreted dwarfs in the outer halo are mostly old, they were typically born in low-mass dwarf galaxies that had star formation histories that are extended enough (> 1 Gyr) to have some iron-rich Type-Ia enhancement (and thus Mg/Fe-depletion), as expected from semi-analytic models [84, 124]. The outflow stars, on the other hand, were born of gas that was recently enriched in a starburst (via short-lived massive stars with high alpha yields) but liberated from the main galaxy prior to Type-Ia enrichment. This is consistent with the notion that alpha-enhancement is indicative of short-lived star formation rather than overall stellar age.

2.5.3 The Local Stellar Halo

Stars in the local stellar halo offer rich observable diagnostics and this motivates us to explore the degree to which stars formed in outflows may contribute to the local stellar halo and whether their presence might be discerned using observations.

Before summarizing results for all six of our halos, we use the `m12i`, the original *Latte* primary halo [229], as an example to illustrate our approach.

The Local Hot Stellar Halo of the Latte Galaxy

In order to define local solar-like populations of stars we construct an ensemble of simulated environments that mimic stellar observations within 5 kpc spheres around the sun. Specifically, we select all star particles that exist within a torus centered on a ring radius 8 kpc in the disc plane from the center of each galaxy. The small radius of the torus is 5 kpc around

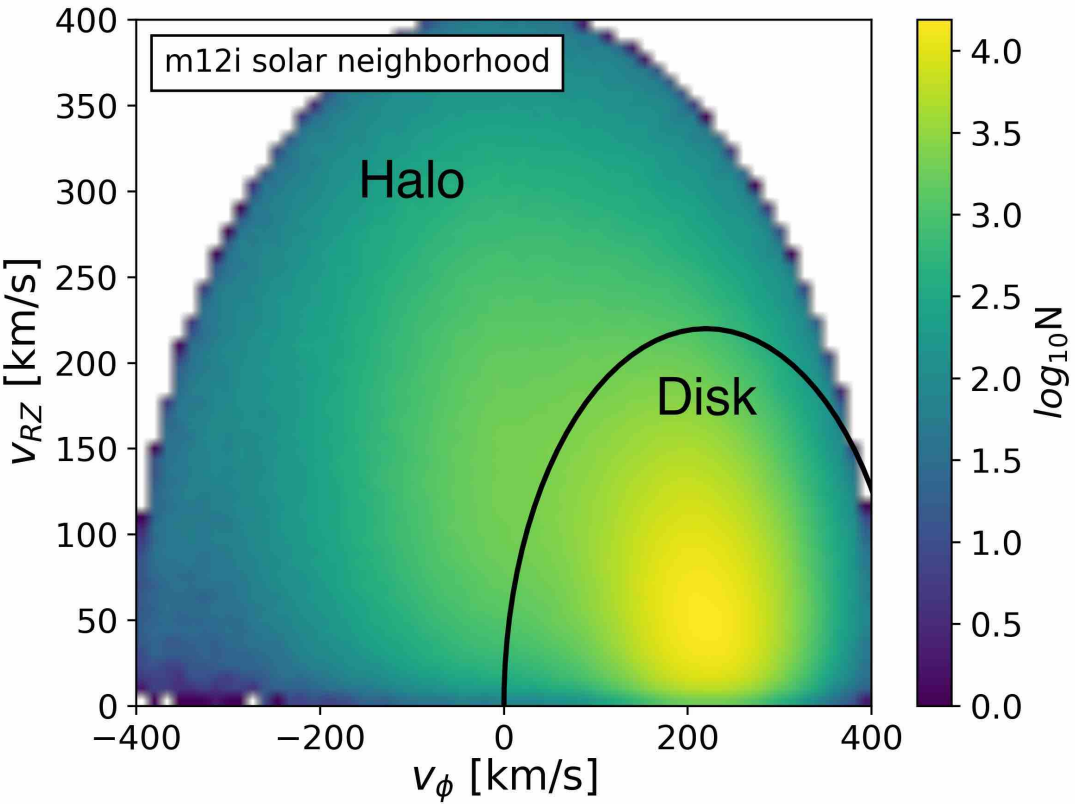

Figure 2.12: Toomre diagram of stars in an ensemble of solar neighborhoods in `m12i`, specifically all star particles within 5 kpc of an 8 kpc ring about the galactic center. We divide the star particles into disc and halo components, based on their location in this diagram. Halo stars have $|\mathbf{V} - \mathbf{V}_{\rm LSR}| > \ 220\,{\rm km\,s^{-1}}$, as indicated by the black line.

the main ring.

Figure 2.12 shows the kinematic properties of star particles found in the solar neighborhood torus in `m12i`. This is a Toomre diagram with the Galactocentric azimuthal component of the velocity vector, V_ϕ, on the horizontal axis and the perpendicular Toomre component, $\sqrt{(V_R^2 + V_Z^2)}$, on the vertical axis. Disc stars dominate a large overdensity at $V_\phi \approx 220\,{\rm km\,s^{-1}}$, corresponding to the circular velocity of the Local Standard of Rest (LSR). Following the selection method of Nissen & Schuster 2010 [168] and Bonaca et al. 2017 [31], we identify halo stars with the velocity cut $|\mathbf{V} - \mathbf{V}_{\rm LSR}| > \ 220\,{\rm km\,s^{-1}}$, where $\mathbf{V}_{\rm LSR}$ is defined to have $V_\phi = 220\,{\rm km\,s^{-1}}$, $V_R = 0$, $V_Z = 0$. The black line in Figure 2.12 marks the boundary where

we divide the two populations, as labeled.

The left panel of Figure 2.13 shows the metallicity distribution for the two kinematic components identified in Figure 2.12. The distribution of disc stars (cyan) is more metal-rich than the halo (magenta) and peaks at approximately solar metallicity, [Fe/H] = 0. The halo is comparatively metal-poor and shows a peak at [Fe/H] ~ -0.5, which is higher than the typical inner halo of the Milky Way [4]. Here we also show the sub-components of halo stars with different birth radial velocities. The shaded yellow histogram shows the metallicity distribution for the halos stars with $V_{\rm rad}^{\rm birth} > 150\,{\rm km\,s^{-1}}$ while the green one with a slightly stricter criterion, with $V_{\rm rad}^{\rm birth} > 200\,{\rm km\,s^{-1}}$. These two components, which have birth velocities indicative of outflows stars, are located in the metal-rich tail of the distribution of halo stars. This region overlaps significantly with disc star metallicity distribution, which is consistent with the idea that these stars were initially born within the disc but now have a hotter velocity distribution than present-day disc stars.

We have examined the chemical abundances of local halo stars as a function of birth velocity and birth radius and find no trend that differentiates outflow stars from heated disc stars in this space (see Figure A.2). They also show no significant difference in $z = 0$ kinematics from other halo stars (see Figure A.3).

The right panel of Figure 2.13 presents the distribution of radial birth velocities of local stars divided in the same way between disc and halo. Disc stars show a symmetric distribution about the $V_{\rm rad}^{\rm birth} \simeq 0\,{\rm km\,s^{-1}}$, whereas halo stars show a significant asymmetry towards positive birth radial velocities, which suggests that some fraction of these stars were born in outflows. We have argued earlier that outflow stars contribute a significant amount to the outer stellar halo, is is therefore natural to suspect that a fraction of high-velocity halo stars in the solar neighborhood were also born this way. As the energy required to put stars on plunging orbits in the solar neighborhood is potentially lower than that required to make them orbit to the outer stellar halo, we might even expect to see more of these stars in the

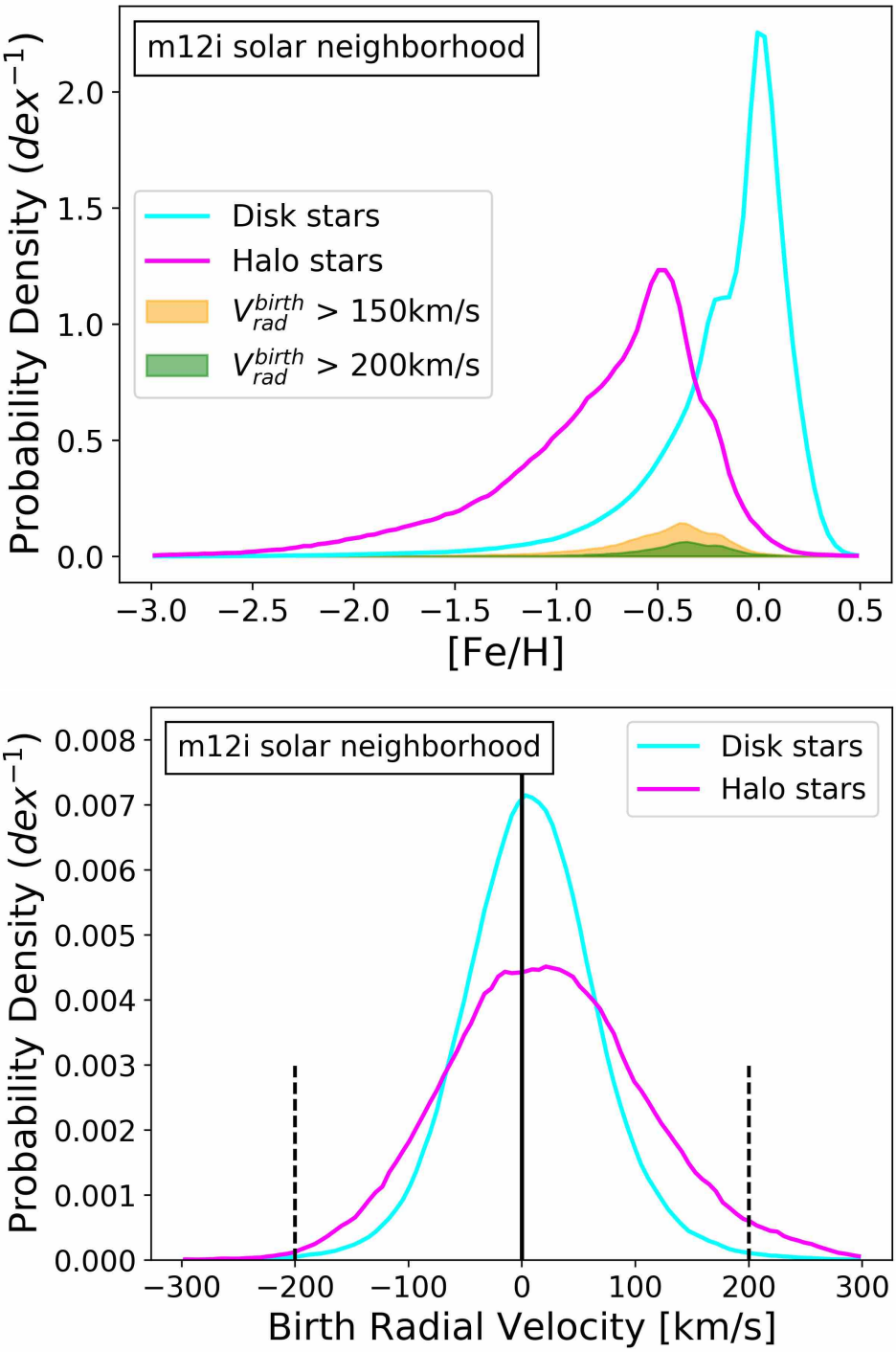

Figure 2.13: **Top:** Metallicity distributions of local kinematically-identified disc stars (cyan) and halo stars (magenta) in `m12i`. Disc stars are more metal-rich, as expected. Halo stars that had radial velocities at birth indicative of outflows ($> 150\,\mathrm{km\,s^{-1}}$ and $> 200\,\mathrm{km\,s^{-1}}$, green and yellow) are shown within the halo distributions. Outflow-identified stars preferentially inhabit the high-[Fe/H] tail of the local stellar halo. **Bottom:** Radial velocities at birth for local disc (cyan) and halo (magenta) stars. Disc stars were born with a symmetric distribution of radial velocities, with a 98% width spanning $\pm 150\,\mathrm{km\,s^{-1}}$. Halo stars show a significant asymmetry towards positive birth velocities, indicative of an outflow contribution.

area around the Sun.

We now focus on kinematically identified halo stars and divide them into a metal-rich component with [Fe/H] > -1.0, and a metal-poor one with [Fe/H] ≤ -1.0, in a similar manner as Bonaca et al. 2017 [31]. Approximately 80% of the halo sample in `m12i` is metal-rich by this definition, which is comparable to the $\sim 50\%$ metal-rich fraction of local halo stars identified by Bonaca et al. 2017 [31] for the Milky Way.

The left panel of Figure 2.14 demonstrate that almost all these metal-rich local halo stars were born within ~ 15 kpc of the center of the galaxy, with the median of the distribution at 6 kpc. These stars were either born in the central disc/galaxy and subsequently heated or they were born in outflows. The metal poor halo stars, by contrast, shows a significant contribution from stars born at large distances. We find $\sim 40\%$ of the metal-poor stars formed with $r_{\rm birth} > 20$ kpc, suggesting that many of these stars were formed inside dwarf galaxies that later merged with the host galaxy.

The right panel of Figure 2.14 shows the birth radial velocity distributions for each of these two populations. The local metal poor halo in `m12i` has a roughly symmetric birth velocity distribution (cyan), with a slight preference for infall velocities at birth. This is again consistent with a significant contribution from accreted dwarfs galaxies. The metal-rich population, shown in magenta, is significantly skewed towards positive birth velocity. It is clear that the asymmetry in halo star birth velocities seen in the right panel of Figure 2.13 mainly comes from metal-rich halo stars. The dashed line shows a Gaussian fit to the negative portion of the metal-poor distribution, which is remarkably similar to the birth velocity distribution of disc stars shown by the cyan line in the right panel of Figure 2.13. If we interpret this part of the distribution as the heated-disc contribution to the stellar halo, the remaining shaded region can be interpreted as coming from outflow stars. If we do so, we find that these stars contributes approximately 27% of metal-rich halo stars locally.

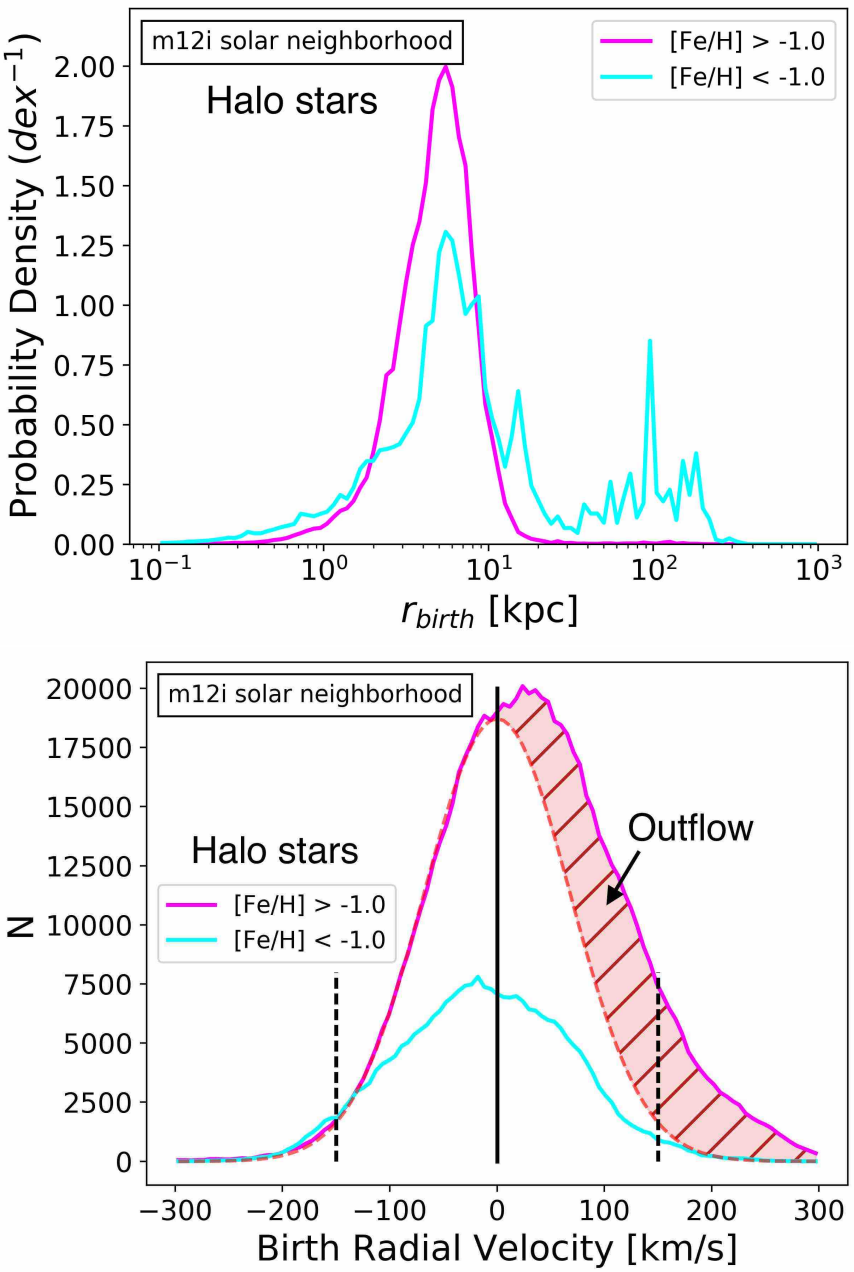

Figure 2.14: **Top:** Birth radii distributions of local kinematically-identified halo stars in `m12i` split into two groups of metal-rich ([Fe/H] > -1.0, magenta) and metal poor ([Fe/H] < -1.0, cyan) stars. A significant fraction of local metal-poor halo stars formed at large distances, suggesting that accretion events contributed a major portion of this population. In contrast, metal-rich local halo stars formed primarily inside the central galaxy. **Bottom:** Radial velocities at birth for the same two populations of local halo stars. Vertical dashed lines at ± 150 km s^{-1} are shown for reference. The metal-poor halo stars have a roughly symmetric birth velocity distribution. The metal-rich halo stars, on the other hand, show a strong asymmetry towards positive birth velocities. The dashed line shows a Gaussian fit to the negative part of the metal-rich $V_{\rm rad}^{\rm birth}$ distribution. If we treat the full Gaussian distribution as the heated-disc contribution to the metal-rich stellar halo, the remaining shaded region can be interpreted as coming from outflow stars (27%).

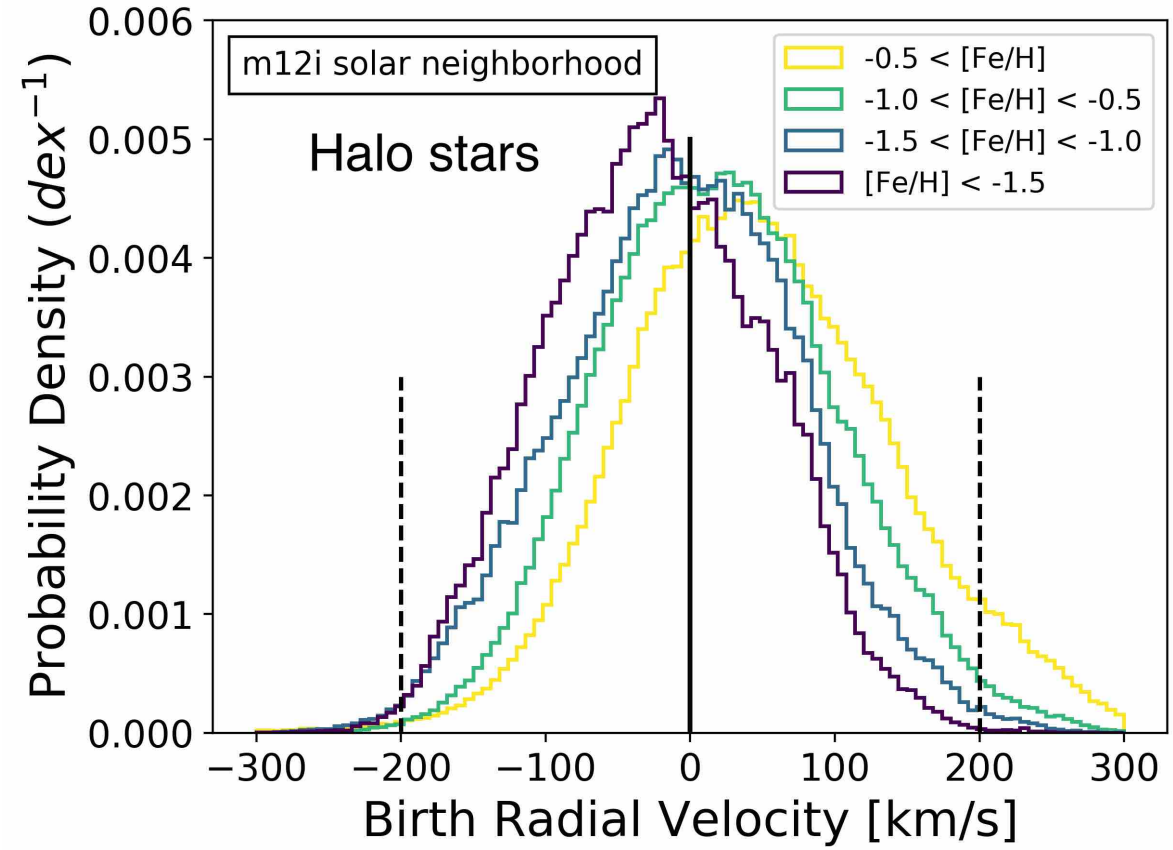

Figure 2.15: Radial velocities at birth for solar neighborhood halo stars in different metallicity bins as indicated. The most metal poor local halo stars have birth velocity distributions that are biased towards negative values, indicative of a large contribution from accreted stars that were born within infalling dwarf galaxies. As metallicity increases, the birth velocity distributions shift towards positive values, as would be expected if outflows make up an increasing fraction of the local stellar halo at higher metallicities.

In Figure 2.15, we further explore this asymmetry by looking at the differences in the birth radial velocity distribution for halo stars with different metallicities. The most metal-rich stars (yellow) are strongly skewed towards being born with large, positive (outflow) velocities. The most metal-poor stars (purple) tend to have been born with negative radial velocities, indicative of infall inside of accreting dwarf galaxies. If we fit a Gaussian to the negative side of the [Fe/H] > -0.5 distribution (as we did in the right-panel of Figure 2.14) we find that the excess outflow fraction is $\sim 40\%$ in this case.

Local Phase-space Structures in the Latte Galaxy

Recently, Belokurov et al. 2019 [23] presented an analysis of Solar neighborhood stars that used *Gaia* data to identify a population of metal-rich halo-like stars, dubbed "the Splash". These stars are on eccentric orbits and many are counter-rotating with respect to the disc. While Belokurov et al. 2019 [23] suggested that the Splash may be associated with a proto-disc-heating event [62, 152, 89], they did not rule out other alternatives, including the role of outflows. Here we show that stars born in outflows could contribute to Splash-like phase-space structure and use `m12i` as an example case.

The top row of Figure 2.16 is similar to Figure 1 of Belokurov et al. 2019 [23] in that it shows distributions of solar neighborhood stars in the space of V_ϕ vs. [Fe/H] for `m12i`. Unlike the figures in the previous sub-section, we have restricted ourselves to stars in the upper disc plane ($2 < |z|$ (kpc) < 3) in order to mimic the cuts in Belokurov et al. 2019 [23]. The upper left panel shows log-density. Of particular interest is the upper right panel of Figure 2.16, which shows row-normalized [Fe/H] distributions at fixed V_ϕ. Several features are boxed and numbered. Box 1 corresponds to a metal-rich thin-disc component. At slightly lower metallicity, box 2 identifies slowly-rotating thick-disc stars. Box 3 highlights a feature that has strong qualitative similarity to the Milky Way Splash [23]: a significant retrograde contribution at metallicities higher than the traditional stellar halo. Box 4 is reminiscent

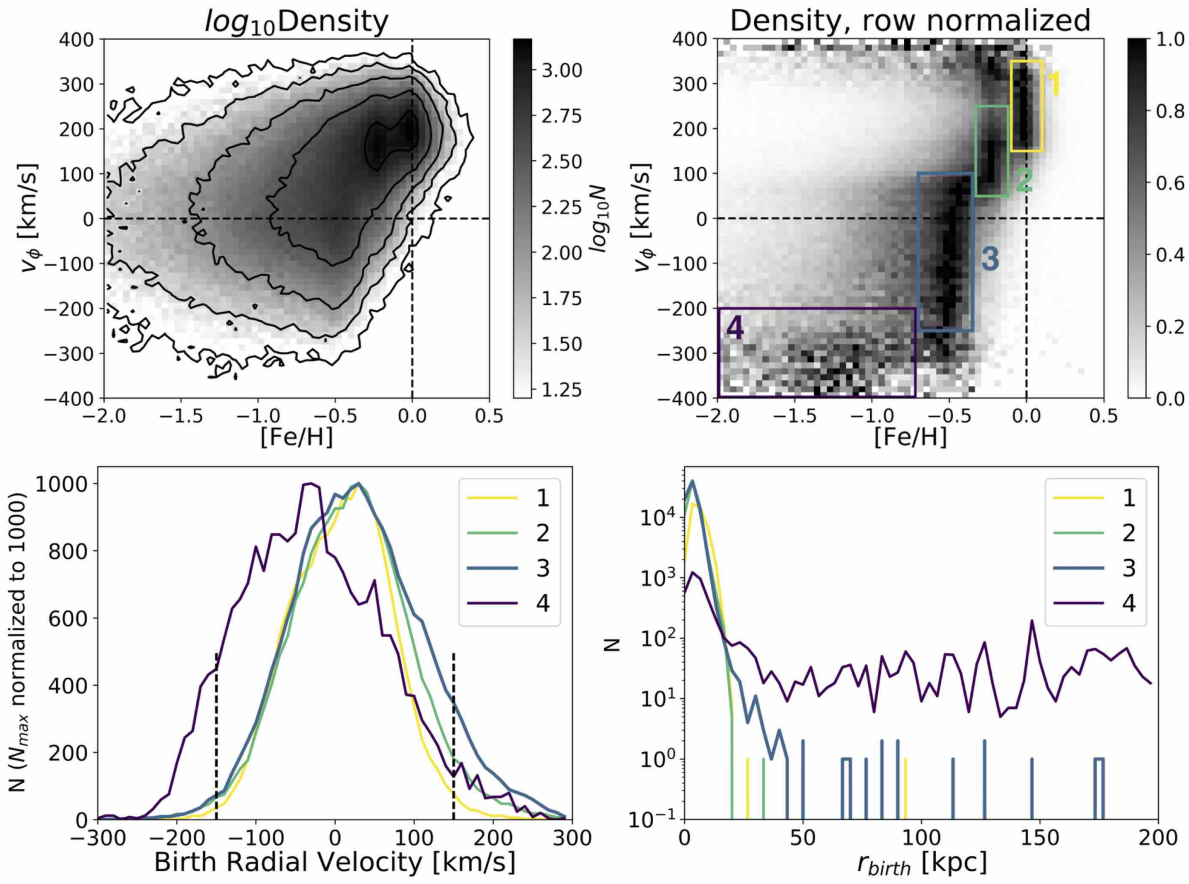

Figure 2.16: Phase-space signatures of stellar origins for stars within $2 < |z|(\text{kpc}) < 3$ of sun-like neighborhoods in `m12i`. The top row presents stars in the plane of V_ϕ -[Fe/H], mimicking Figure 1 of Belokurov et al. 2019 [23]. The left panel shows the logarithm of the stellar density. The right panel shows the row-normalized stellar density – that is, the [Fe/H] distribution at fixed V_ϕ. Note the four boxed regions here : Boxes 1 & 2 identify very metal-rich thin/thick disc components; Box 3 highlights a Splash-like metal-rich population with low and/or negative v_ϕ; Box 4 shows a highly retrograde Sequoia-like feature. The bottom row illustrates the distributions of birth radial velocities (left) and birth radii (right) of stars in different boxed regions. The Splash-like stars (3, blue) have birth velocities that are skewed positive and birth radii mostly confined to the central galaxy, indicative of an outflow contribution. Box 4 (purple) shows indications of an accreted population: birth velocities that are skewed negative and birth radii that extend well outside the central galaxy.

of the strongly retrograde Milky Way feature known as Sequoia [163], though its retrograde speed is faster.

The bottom row of Figure 2.16 presents information on the birth radial velocities (left) and birth radii (right) for stars associated with each of the four features (boxes) numbered in the upper-right panel. We see that the Sequoia-like retrograde feature (box 4, purple) contains stars that are indicative of accretion: a birth-velocity distribution that is skewed negative and birth radius distribution that extends well beyond the central galaxy. The thin-disc region (box 1, yellow) also looks as expected: a symmetric birth radial velocity distribution and birth radii that are all confined to the disc region ($r_{\rm birth} \lesssim 20$ kpc).

Now consider the birth properties of the Splash-like stars (box 3, blue). The birth radial-velocity distribution is skewed positive, indicative of a significant contribution from stars born in outflows. The birth radius distribution is also largely confined to the central galaxy. Overall, this mock-Splash feature appears to be made of both a heated disc component and a stellar outflow component. The disc-thickening event that created this feature involved starburst activity that included stellar outflows. The more traditionally identified thick-disc region (box 2, green) is similar, though the birth radial-velocity distribution is less skewed, and appears to be predominantly heated disc. Though not shown, the age distributions of stars in each of these four boxes is monotonic in metallicity. Box 4 stars are the oldest (9-12 Gyr), with box 3 (Splash-like) stars slightly younger (~ 8 Gyr). Our thin-disc (box 1) has a less extended star-formation history than that of the Milky way, spanning ages 0-5 Gyr, while the thick-disc feature (box 2) dates back to the end of the thin-disc phase (5-7 Gyr).

The above exercise illustrates the power of combining numerical simulations with high-dimensional phase-space data to provide insight into formation history of the Milky Way [6, 99]. More work in this direction is certainly warranted.

Summary of Outflow Fractions in Solar Neighborhoods

Figure 2.17 provides a summary of local kinematically-identified stellar halo outflow stars for all six of our host halos. We are specifically quoting the fraction of the local stellar halo identified as being born in stellar outflows, $M_{\rm outflow}(>X)/M_{\rm total}(>X)$, plotted as a function of X = [Fe/H] of the stars. We have adopted two methods for identifying stars as being born in outflows. First, the solid lines show the fraction calculated using the excess positive portion of the birth velocity distribution as illustrated in the right panel of Figure 2.14. The dashed lines adopt a simpler choice, which defines outflow stars to be those born with radial velocities greater than $150\,{\rm km\,s^{-1}}$. In most cases the results are similar, with rising outflow fractions towards increasing metallicity. However, the exact fraction does depends on the accretion history of the main galaxies. One of the exceptions is halo `m12b`, which has undergone a recent merger. The resultant birth-velocity distribution of kinematically-identified halo stars has very little skewness and produces a near-zero outflow fraction via the first definition.

How might we distinguish outflow stars from other stars in the local stellar halo? While Figure 2.14 demonstrates that the outflow fraction rises with increasing metallicity, stars born in outflows remain minority populations even at the highest metallicities. In Appendix A.2 we show that neither the $z = 0$ kinematics of halo stars nor chemical abundances alone provide a strong discriminant, mainly because the overall fraction of outflow stars is small enough that small differences in underlying distributions are washed out. A better determination can be made by exploring the joint distribution of metallicity and radial velocity. Figure 2.18 shows the fraction of stars born in outflows (color bar, using $V_{\rm rad}^{\rm birth} > 150\,{\rm km\,s^{-1}}$) as a function of both [Fe/H] and absolute value of current radial velocity. We see that the outflow fraction dominates for stars that are both fast *and* metal-rich. Metal-rich retrograde stars are also potential candidates (Figure 2.16).

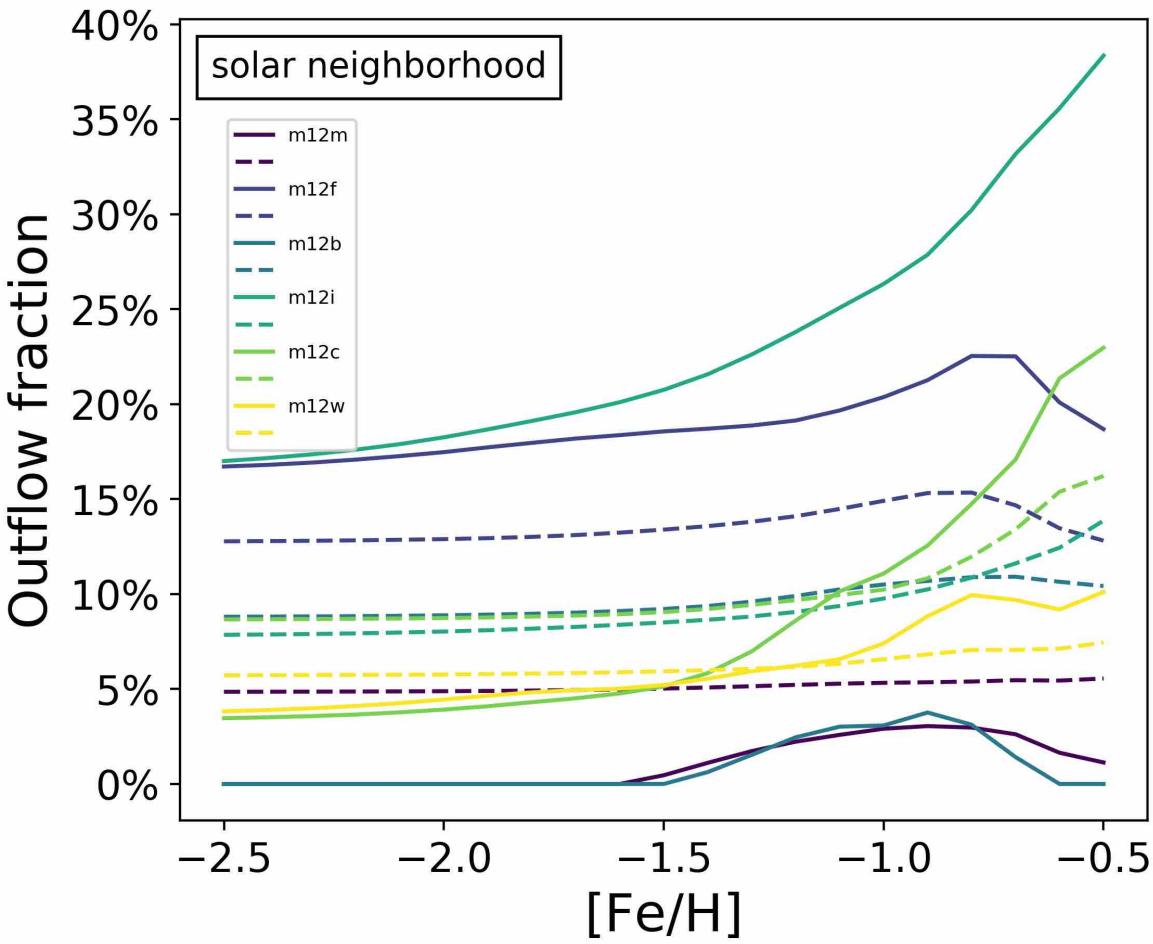

Figure 2.17: Fraction of the local stellar halo identified as being formed in outflows as a function of stellar metallicity in each of our simulations. Fractions include stars more metal-rich than the value of [Fe/H] shown on the horizontal axis. We have identified outflow fractions using two definitions. First, we associate the outflow fraction with the excess above a symmetric birth velocity distribution as illustrated in the right panel of Figure 2.15. Solid lines use this definition. In the second case (dashed) we use the fraction of stars born with radial velocities $> 150\,\mathrm{km\,s^{-1}}$. In most cases, the fraction rises towards higher metallicity, with as much as $\sim 40\%$ of the most metal-rich local stellar halo coming from outflows by this definition.

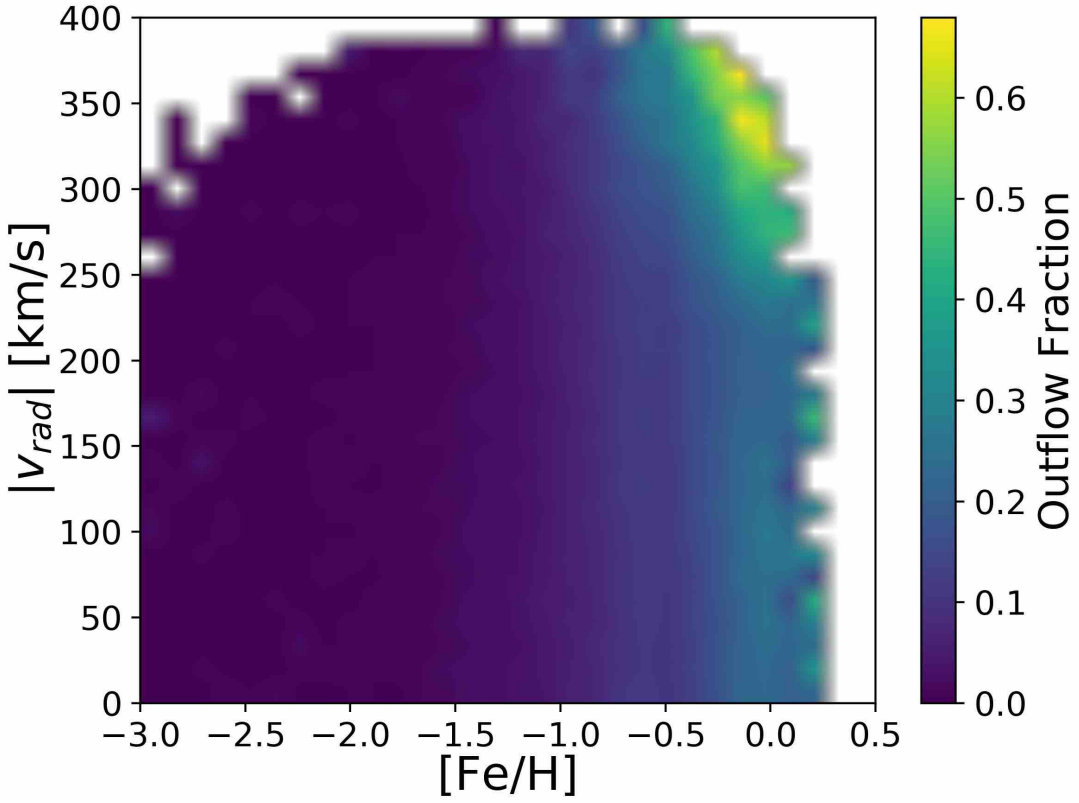

Figure 2.18: Fraction of local halo stars that were born in outflows (color bar) as a function of stellar current radial velocity and metallicity. We assume stars with $V_{\rm rad}^{\rm birth} > 150\,{\rm km\,s^{-1}}$ were born in outflows. We see that the majority of stars with both the highest velocities ($|V_{\rm rad}| \gtrsim 300\,{\rm km\,s^{-1}}$) *and* highest metallicities ([Fe/H] $\gtrsim -0.5$) were created in outflows.

2.6 Discussion

This paper introduces the possibility that galactic stellar halos may be populated by stars born in dense-gas outflows driven by feedback events. The idea that expanding supershells can trigger star formation has been with us for more than thirty years [159]. Recent observations have confirmed the existence of star formation triggered in expanding superbubbles [233, 140, 43, 66, 67], but to our knowledge ours is the first to explicitly connect this possibility with stellar halo formation. Our proposal is motivated both by an analysis of simulations and by spectroscopic evidence for star formation in outflows [153, 88]. Specifically, these outflow stars are born with velocities fast enough to take them far from galactic discs but slow enough that they remain bound to galactic halos. Anecdotally, the outflow scenario bares resemblance to the classic idea of [ELS 65], who suggested that halo stars formed in rapidly *infalling* gas clouds. Here we posit a phase-reversal of ELS: some fraction halo stars formed in rapidly outflowing gas.

Before summarizing our quantitative conclusions, it is important to qualify our results given the difficulty of the numerical problem we are considering. Accelerated cold clouds are subject to hydrodynamical instabilities that could destroy them on timescales shorter than those required for star formation [39, 204], though rapid re-cooling as outflows expand [221] or radiative shocks with the ambient medium [241, 191] can help explain the prevalence of cold, dense outflow material as observed. As discussed by Ferrara & Scannapieco 2016 [81], the degree to which dust grains survive and mix into the cool phase affects rapid molecule formation. Simple estimates of the timescales needed to grow dust grains by accretion of metals from the ISM suggest that dust destruction may not be a major problem in the dense gas that ends up forming stars [190]. Schneider et al. 2018[205] have used the Cholla Galactic Outflow Simulations to show that the highest velocity cool outflowing gas observed in starburst systems may have a dual origin, where clustered supernova feedback ejects gas out of the disc where it is subsequently accelerated by a hot wind. Though the episodes they

explore correspond to more extreme, high star-formation cases than our systems experience, this picture is qualitatively consistent what we see in our simulations.

With baryonic particle masses of $\sim 7000\ M_{\odot}$ and adaptive force softening down to ~ 1 pc, our simulations do seem to robustly predict the existence of outflows that consist of dense, relatively cold gas. This gas occasionally goes unstable for star formation after acceleration, resulting in stellar outflows. Star formation in our simulations requires gas to be sufficiently dense and Jeans unstable. Importantly, we find that stellar outflows are robust in our simulations for re-runs that require more stringent star formation criteria (see Appendix A.1 and Grudić et al. 2018[101]). It is worth noting that (although we do not quantitatively analyze these runs here) the qualitative phenomenon of star formation in outflows also appears across our previous FIRE-2 *and* FIRE-1 simulations using different numerical resolutions, including or excluding magnetic fields, changing the star formation criteria more broadly, and using an entirely different hydrodynamic method (SPH, in FIRE-1). Given this, we believe that our conclusions are physically plausible (and consistent with observed stellar outflow measurements). However, much higher resolution simulations that include a fair treatment of conduction and other micro-physics will be needed to test for robustness.

The broadest contribution of this work is in positing the possibility that outflow stars may populate the stellar halos of Milky Way-mass galaxies. The degree to which this happens will depend in detail on star formation and galaxy-formation physics; this means that local searches for such a population may offer a new way to test global galaxy formation models. One thing worth noting here is that the simulation presented here do not include systems that perfectly match the Milky Way in their non-axisymmetric mode or in their accretion history. This suggest that more simulations, including those that are targeted to reproduce known aspects of the Milky Way's merger and settling history (see e.g. Purcell et al. 2011 [184], for an example that neglects hydrodynamics) will be required to fully exploit this possibility. However, the results presented here do provide a starting point for such an endeavor. With

these caveats in mind, we can move on to conclude and summarize.

2.7 Conclusions

Using six zoom simulations of Milky Way-mass galaxies, we have found that stellar outflows associated with starburst activity contribute a significant fraction to the stellar halo of each galaxy. These stars form with large positive radial velocities ($\gtrsim$ 150 km s^{-1}, Figure 2.2) inside powerful galactic outflows (Figure 2.8). As shown in Figure 2.9, stellar outflows are more common during the early, bursty star formation phases of our galaxies ($z \gtrsim 0.3$). While the overall fraction of stars formed in outflows is small ($\sim 1\%$), during starbursts the outflow fraction ranges from $\sim 1 - 50\%$ of the overall star formation rate.

The majority of outflow stars fall back in on radial orbits that are similar to the bulk of the stellar halo at $z = 0$. Though the fraction varies from halo to halo, we find that $5 - 40\%$ of outer stellar halos ($r > 50$ kpc) of our galaxies formed in radial outflows (Figure 2.4). The rest of the outer halo is dominated by stars from accreted, disrupted satellites, which tend to be metal poor. If we restrict to the most metal rich ([Fe/H] > -1) outer-halo stars, an even higher fractions were born in outflows ($\sim 30 - 80\%$) owing to the fact that these outflow stars originated from the more metal rich gas in the massive central galaxy.

In the inner halo ($r \sim 8$ kpc), we find that outflows contribute substantially only the the most metal-rich portion, making up $\sim 10 - 40\%$ of [Fe/H] > -0.5 stellar halo material in the solar neighborhood (Figure 2.17). The lowest metallicity component of the local stellar halo in our simulations tends to be dominated by accretions, while the metal-rich portion is made of a combination of accreted stars, kicked-out (heated disc) stars, and *in-situ* stars born in outflows (Figure 2.14). As shown in Figure 2.16, outflow stars may provide a non-trivial contribution to high-metallicity retrograde stars, such as those identified in the Splash

feature by Belokurov et al. 2019 [23].

The outer stellar halo of the Milky Way and M31 hold some promise for finding evidence for outflow stars. Not only are the outflow stars more metal rich than the dominant, accreted stellar halo, they tend to be more smoothly distributed (Figure 2.10) and α-enhanced. They stand out clearly in [Mg/Fe]-[Fe/H] diagrams (Figure 2.11). Efforts such as the H3 Spectroscopic Survey for the Milky Way [48] and ongoing work using resolved stars around M31 from Keck [73, 74] may enable direct comparisons to these predictions.

Distinguishing between outflow stars and other halo components in the *local* stellar halo ($r \sim 8$ kpc) may be more difficult. The distributions of their current tangential velocities are almost identical. We find only small differences in the $z = 0$ velocity distributions or the chemical properties of outflow stars (see Appendix A.2). Indeed, outflow stars that have remained bound to the inner stellar halo appear to be quite similar to heated disc stars in everything other than their birth velocities. We find that outflow stars dominate the local halo population only among stars that are both high in radial velocity *and* high in metallicity (see Figure 2.18). This may be the space where outflow stars are most easily identified in the stellar halo.

Could an outflow event be directly observed? At least one of our six galaxies has a prominent visible plume of young stars born in an outflow that is visible at $z = 0$ (halo `m12w`). A stream of this kind could be observable in imaging of the nearby universe as a blue stream of young stars (see Figure 2.5, for example). A potential avenue of future work is to make predictions on the detection probability of such events and the expectations for the surface brightness of young plumes of outflow stars.

Stellar outflows may also provide a potential source for extreme-velocity or hypervelocity stars [38, 106]. The radius-velocity diagram of `m12w` shows that some outflow stars could have radial velocities as high as $\sim 300\,\mathrm{km\,s^{-1}}$ (Figure 2.10). We also find that a small

fraction ($\sim 5\%$) of outflow stars generated in outflow events are unbound. While most HVS discoveries are are metal-poor (and therefore are not good matches for the stellar outflows we predict in this scenario), there are HVS candidates that have metallicity higher than expected in the stellar halo [63]. These high-metallicity HVSs could potentially be sourced by outflows.

A related observational constraint will be to consider the direct rates of outflows predicted in our simulations compared to ongoing efforts to detect stellar outflows in spectroscopic surveys. As discussed in the introduction, Gallagher et al. 2019 [88] have used integral field MaNGA data to show that star formation inside outflows accounts for $5 - 30\%$ of the total star formation in their galaxies when detected. This is consistent with the rough estimate presented in Figure 2.9, but direct mock observations of the simulations would be required for accurate comparisons.

In work related to ours, Ma et al. 2019[145] have used FIRE-2 simulations of high-redshift galaxies to study star formation in clusters. They find star formation at the edges of shells in high density gas clouds, compressed by feedback-driven winds, which is quite similar to the physical conditions we find fundamental to launching outflow stars in this paper. It is encouraging that Ma et al. 2019[145] find similar results using a simulation suite that includes a run with ~ 70 times better mass resolution than our own.

Another implication for bubble-driven star formation outflow is that it may enable higher ionizing photon escape fractions than might otherwise be possible. Ma et al. 2020[148] have studied this effect in detail using FIRE-2 simulations to estimate the escape fraction of stars formed in this manner and find a large time-average escape fraction ($\gtrsim 10\%$), for several different star formation models. Specifically, stars formed at the edges of evacuated shells have much larger escape fractions. They also find age gradients for stars born at the shell front, which is again in agreement with the idea of an accelerating shell of star formation, consistent with the outflow picture presented here.

In summary, we have introduced the possibility that stellar outflows contribute a non-negligible fraction of stars to the hot, extended stellar halos of Milky Way-mass galaxies. Such a population is plausible given the evidence that dense molecular outflows and stellar outflows exist in nature [153, 88]. The characteristics of such a halo population are likely sensitive to the nature of feedback and star-formation physics (Section 2.6). Given this, we believe that local observational searches for stellar-halo outflow stars may provide yet another place where near-field cosmological probes can begin to test global models of galaxy formation.

Chapter 3

The bursty origin of the Milky Way thick disc

3.1 Introduction

Milky-Way-mass disc galaxies in the local Universe, including our own, are often characterised by a thin disc component embedded within a thicker disc, which accounts for $\sim$10$-$15% of total disc luminosity [226]. The Milky Way itself has a distribution of disc stars that can be decomposed into thin and thick components spatially [96, 126, 26, 32]. Thicker-disc stars tend to be older, more metal poor, and more alpha-enhanced [87, 27, 182, 138, 110, 188, 107, 151, 108, 210]. These characteristics may be loosely interpreted as evidence that thick disc stars formed early and rapidly, perhaps in a series of bursts [226]. Snaith et al. 2014[212] use elemental abundances of long-lived stars to derive a star-formation history a Milky Way thick disc population and conclude that these stars emerged during an early, elevated period of star formation, and that the Galactic thick disc may be comparable *in mass* (not luminosity) to the young ($<$ 8 Gyr old) thin disc.

While it is natural to think of the thin/thick disc dichotomy as reflecting the existence of two distinct and separate kinematic populations, the Milky Way appears to have a continuous distribution of disc thicknesses that vary smoothly with fixed abundance [33]. There is certainly a dichotomy in the the ratio of alpha to iron (at low iron) in the solar vicinity, though the relative distributions of high and low alpha elements vary smoothly with location in the disc [107, 228]. These trends may be explained without requiring a distinct thick disc component that emerged from a separate evolutionary path [209]. Nevertheless, it is useful to use the terms "thick disc" and "thin disc" as a shorthand classification to help us compare and contrast stars with more eccentric orbits that take them farther from the disc plane to those with more circular orbits that align tightly within it.

Despite years of study, an understanding of how thick and thin populations arise within the broader story of galaxy formation remains a key question. One of the most enduring ideas is that pre-existing thin discs are heated in mergers with small satellite galaxies to create a vertically extended component [186, 130, 185]. In fact, the phase-space structure of stars in the solar neighborhood provides some evidence that such a event – the Gaia-Enceladus Sausage merger – may have been significant enough to heat a proto Milky Way disc, under the assumption that a thin disc existed at this early time [20, 113].

However, the chemical abundance structure of the Milky Way disfavours the idea that thick-disc formation is associated with a single discrete event [86]. Rather, these data favour an "upside down" formation scenario – first predicted by cosmological simulations [34, 35, 36, 28] – where stars are born in relatively thick discs at early times, and only later form in thin discs.

Many recent cosmological simulations naturally produce $z = 0$ discs with young stars concentrated in a thinner component than old stars [147, 164, 98, 181, 29, 178]. These same simulations at high redshift produce discs that are systematically thicker and clumpier than those at low redshift, as observed in nearly all deep, high-resolution imaging studies of galax-

ies [70, 72, 208, 95, 177, 71]. The observed transition from thick irregular galaxies at high redshift to thin rotation-dominated discs at low redshift is well established, and often referred to as "disc settling" [128].

Whilst upside-down disc formation is seen regularly in simulations, the physical origin of this thick-to-thin transition has been hard to distill. One idea is that discs are born thick during an early period of gas-rich mergers [34]. At high redshift, high star-formation rate densities, high gas fractions, and feedback-induced turbulence can also contribute to an initially hot disc [139]. An alternative possibility is that stars are initially born in thin discs, but are quickly and continuously heated owing to chaotic accretion of gas [160]. In some simulations, most stars are born kinematically hotter at early times *and* subsequently heated after birth on a short timescale [147, 29].

In this paper, we explore the transition from thick to thin disc formation in twelve Milky-way-mass galaxies drawn from FIRE-2 cosmological zoom-in simulations. As seen in previous work [34, 28, 147, 164, 29, 178], our discs tend to form upside down, with the thick discs in place early and the thin disc forming at late times. One new finding in our work is that the transition from thick to thin-disc formation correlates with a transition in star formation mode, from an early, elevated bursty phase with highly time-variable star formation rate, to a late-time steady phase of near-constant star formation rate. Thin-disc stars tend to be born during the late-time steady phase, whilst thick-disc stars are associated with the latter part of the bursty phase. Galaxies with older thick-disc populations have an earlier transition from bursty to steady star formation. The earlier the transition time, the more dominant the thin disc is at $z = 0$.

A transition from bursty to steady star formation has been reported previously in the FIRE simulations, at $z = 0.5 - 1.5$ in Milky-Way-mass haloes [162, 213, 8, 9, 78]. In particular, Stern et al. 2021 [216] show that the transition to steady star formation coincides with the virialisation of the inner circumgalactic medium (CGM). Specifically, when haloes in FIRE

cross a characteristic mass scale ($\sim 10^{12}$ $M_\odot$), the cooling time of shocked gas in the inner halo (0.1 R_{vir}) exceeds the local free-fall time. This creates a hot confining medium, with high and nearly uniform thermal pressure. After this time, Stern et al. 2021 [216] observes that star formation becomes less bursty and gaseous discs become more rotationally supported. This steady, settled disc phase may be enabled by the hot, pressurised inner CGM itself, which may prevent supernova-driven outflows from repeatedly blowing out the interstellar medium (ISM) in a way that would otherwise might perturb disc structure [156].

Of particular relevance is work by Ma et al. 2017 [147], who used a slightly lower resolution FIRE-1 zoom-in simulation to show that disc stars at large scale-height (thick disc stars) form primarily during an early chaotic bursty mode, whilst younger stars were formed in a more stable disc. In what follows, we perform a more systematic analysis using a larger, higher resolution sample of FIRE-2 haloes and confirm that this result is more general. This motivates us to suggest that the physical transition from bursty to steady star formation also coincides with a shift from thick-disc to thin-disc formation in Milky-Way-mass galaxies. If this is true in the real Universe, then stellar archaeological studies of the Milky Way could provide a window into past star-formation modes, as well as the build-up of the Galactic CGM.

The outline of this chapter is as follows. In §3.2 we provide an overview of our simulations and present our kinematic definition of thin and thick disc stars. §3.3 presents results focusing for two illustrative cases (§3.3.1) and then on to explore general trends for all galaxies in our sample (§3.3.3). We conclude and discuss our results in the context of the Milky Way in §3.4.

3.2 Simulations and methods

3.2.1 FIRE-2 simulations of Milky-Way-mass galaxies

Our analysis utilises cosmological zoom-in simulations performed with the multi-method gravity plus hydrodynamics code GIZMO [116] from the Feedback In Realistic Environments (FIRE) project[1]. We rely on the FIRE-2 feedback implementation [120] and the mesh-free Lagrangian Godunov (MFM) method. The MFM approach provides adaptive spatial resolution and maintains conservation of mass, energy, and momentum. FIRE-2 includes radiative heating and cooling for gas across a temperature range of $10 - 10^{10}$K. Heating sources include an ionising background [79], stellar feedback from OB stars, AGB mass-loss, type Ia and type II supernovae, photoelectric heating, and radiation pressure – with inputs taken directly from stellar evolution models. The simulations self-consistently generate and track 11 elemental abundances (H, HE, C, N, O, Ne, Mg, Si, S, Ca, and Fe), and include sub-grid diffusion of these elements in gas via turbulence [117, 218, 75]. Star formation occurs in gas that is locally self-gravitating, sufficiently dense (> 1000 cm^{-3}), Jeans unstable and molecular (following Krumholz & Gnedin 2011 [137]). Locally, star formation efficiency is set to 100% per free-fall time; i.e., $SFR_{\rm particle} = m_{\rm particle} \cdot f_{\rm mol} \, / \, t_{\rm ff}$, where $f_{\rm mol}$ is the self-shielded molecular fraction of each gas particle and $t_{\rm ff}$ is the free-fall time. Gas particles are converted to stars at this rate stochastically [129]. Note that this does *not* imply that the global efficiency of star formation is 100% within a giant-molecular cloud (or across larger scales). Self-regulated feedback limits star formation to ∼1-10% per free-fall time [79, 118, 174].

In this work, we analyse 12 Milky-Way-mass galaxies (Table 3.1 and Table 3.2). These zoom simulations are initialised following Oñorbe et al. 2014[170]. Six of these galaxies (with names following the convention `m12*`) are isolated and part of the Latte suite [229, 93, 118,

[1] `https://fire.northwestern.edu/`

92]. Six, with names associated with famous duos (e.g. `Romeo` and `Juliet`), are part of the ELVIS on FIRE project [92, 94] and are set in Local-Group-like configurations, as in the ELVIS suite [91]. This suite includes three simulations, containing two MW/M31-mass galaxies each. The main haloes were selected so that they have similar relative separations and velocities as of the MW-M31 pair in the Local Group (LG). Table 3.1 lists the initial baryonic particle masses for each simulation. Latte gas and star particles have initial masses of 7070 $M_\odot$, whilst ELVIS on FIRE has $\approx 2\times$ better mass resolution ($m_\mathrm{i} = 3500 - 4000\,M_\odot$). Gas softening lengths are fully adaptive down to $\simeq 0.5-1$ pc. Star particle softening lengths are $\simeq 4$ pc physical and a dark matter force softening is $\simeq 40$ pc physical.

3.2.2 Defining thin and thick discs

There are multiple ways to separate a "thick disc" from a "thin disc" population in observations [155]. The physical characteristics authors use to define the thick disc include geometric morphology, kinematics, chemical abundances, and age. The geometric/morphological definition is the natural choice for distant galaxies, where detailed chemical and/or age information is harder to extract.

In this theoretical analysis, we elect to define thick and thin disc populations using a purely kinematic definition based on each star particle's circularity [2], which also produces disc populations that follow the qualitative geometric expectations for thin and thick discs (see below). Whilst it is common in Milky Way studies to use elemental abundances to divide thin and thick disc populations, we adopt this kinematic definition in order to fully decouple our selection from the nature of star formation. Specifically, alpha enhancement correlates with starburst activity, so we would like to avoid using abundance ratios when looking for distinct correlations related to the star formation history. The fact that we find correlations between kinetically-defined thick-disc populations and the mode of star formation suggests

Table 3.1: The simulations we employ in this work. We list the following: the name of the zoom-in target halo, the stellar mass ($M_\star$) within the central 20 kpc of the halo at $z = 0$, the radius (R_{90}) enclosing 90% of $M_\star$, the halo virial mass ($M_{\rm halo}$), the halo virial radius ($R_{\rm halo}$), the resolution of each simulation quantified by the initial baryonic particle mass ($m_{\rm i}$), and the reference that first introduced each halo at the quoted targeted resolution. We also list the lookback time to the end of the bursty phase/onset of the steady phase ($t_{\rm B}$). Hosts with names starting with 'm12' are isolated configurations selected from the Latte suite, whilst the rest are in LG-like pairs from the ELVIS on FIRE suite. The four galaxies marked with an asterisk correspond to short-lived, late-time bursts of star formation taking place after the onset of the steady phase. Three of these four bursts appear to be triggered by minor mergers. The exception is `Thelma`, which has late-time star formation in the "steady" regime (by our formal definition), but is still experiencing fairly variable star formation compared to most of our galaxies at late times. These bursts and/or mergers tend to influence t_{90} but do not significantly affect t_{50} nor $f_{\rm thin\ disc}$. The haloes are ordered by decreasing $t_{\rm B}$, from $t_{\rm B}$ = 6.52 Gyr (`Romeo`, top) to $t_{\rm B}$ = 0.0 Gyr (`m12w`, bottom).

Name	$M_\star$ $[M_\odot]$	R_{90} [kpc]	$M_{\rm halo}$ $[M_\odot]$	$R_{\rm halo}$ [kpc]	$m_{\rm i}$ $[M_\odot]$	$t_{\rm B}$ [Gyr]	Reference
`Romeo`	7.4×10^{10}	13.3	1.0×10^{12}	317	3500	6.52	A
`m12b`*	8.1×10^{10}	9.8	1.1×10^{12}	335	7070	6.32	A
`Remus`	5.1×10^{10}	12.3	9.7×10^{11}	320	4000	5.88	B
`Louise`	2.9×10^{10}	12.0	8.5×10^{11}	310	4000	5.56	A
`m12f`*	8.6×10^{10}	11.0	1.3×10^{12}	355	7070	5.01	C
`Romulus`	1.0×10^{11}	14.2	1.5×10^{12}	375	4000	4.90	B
`Juliet`	4.2×10^{10}	9.6	8.5×10^{11}	302	3500	4.40	A
`m12m`	1.1×10^{11}	11.3	1.2×10^{12}	342	7070	3.81	E
`m12c`*	6.0×10^{10}	9.7	1.1×10^{12}	328	7070	3.70	A
`m12i`	6.4×10^{10}	9.2	9.0×10^{11}	314	7070	3.14	D
`Thelma`*	7.9×10^{10}	12.4	1.1×10^{12}	332	4000	2.57	A
`m12w`	5.8×10^{10}	8.7	8.3×10^{11}	301	7070	0.0	F

Note: The references are: A: [92], B: [94] C: [93], D: [229], E: [120], F: [197].

Table 3.2: The simulations we employ in this work. We present derived quantities here: the lookback time to the end of the bursty phase/onset of the steady phase ($t_{\rm B}$), the mass-weighted thin-disc fraction ($f_{\rm thin\,disc\,m}$), the luminosity-weighted thin-disc fraction ($f_{\rm thin\,disc\,l}$), the median thick-disc age (t_{50}), and the 90% oldest star of the thick disc (t_{90}). The haloes are in the same order as in Table 3.1.

Name	$t_{\rm B}$ [Gyr]	$f_{\rm thin\ disc\ m}$ (M weighted)	$f_{\rm thin\ disc\ l}$ (L weighted)	thick disc t_{50} [Gyr]	thick disc t_{90} [Gyr]
Romeo	6.52	0.45	0.70	8.96	6.16
m12b*	6.32	0.37	0.64	7.34	2.72
Remus	5.88	0.36	0.62	8.22	4.88
Louise	5.56	0.32	0.65	8.11	4.06
m12f*	5.01	0.38	0.65	6.28	2.62
Romulus	4.90	0.37	0.69	7.37	4.92
Juliet	4.40	0.30	0.62	6.74	4.66
m12m	3.81	0.34	0.58	6.07	3.24
m12c*	3.70	0.32	0.62	5.39	2.30
m12i	3.14	0.32	0.59	6.18	3.50
Thelma*	2.57	0.27	0.57	4.73	1.95
m12w	0.0	0.24	0.43	4.38	1.13

that the correlation between thick disc formation and star formation activity is non-trivial. Previous work by Ma et al. 2017 [147] finds qualitatively similar results using more traditional observationally-oriented definitions of the thick disc based on a vertical density profile, suggesting that the result is insensitive to the precise definition.

Our categorisation is based on each star particle's circularity, $\epsilon = j_z/j_c(E)$, defined as the ratio of each particle's angular momentum to that of a circular orbit with the same energy [2]. The angular momentum direction $\hat{z}$ is set by total stellar angular momentum within 10 kpc of each galaxy's center. We categorise star particles with $\epsilon = 0.8 - 1$ as *thin disc* stars, and those with $\epsilon = 0.2 - 0.8$ as *thick disc* stars. Our classification is motivated by past explorations [2, 172, 133], which find that the circularity correlates well with standard morphological definitions of thin and thick disc populations.

The left and middle panels of Figure 3.1 illustrate our circularity-based definitions for two specific simulations: Romeo (top) and Juliet (bottom). The left panels show the mass-

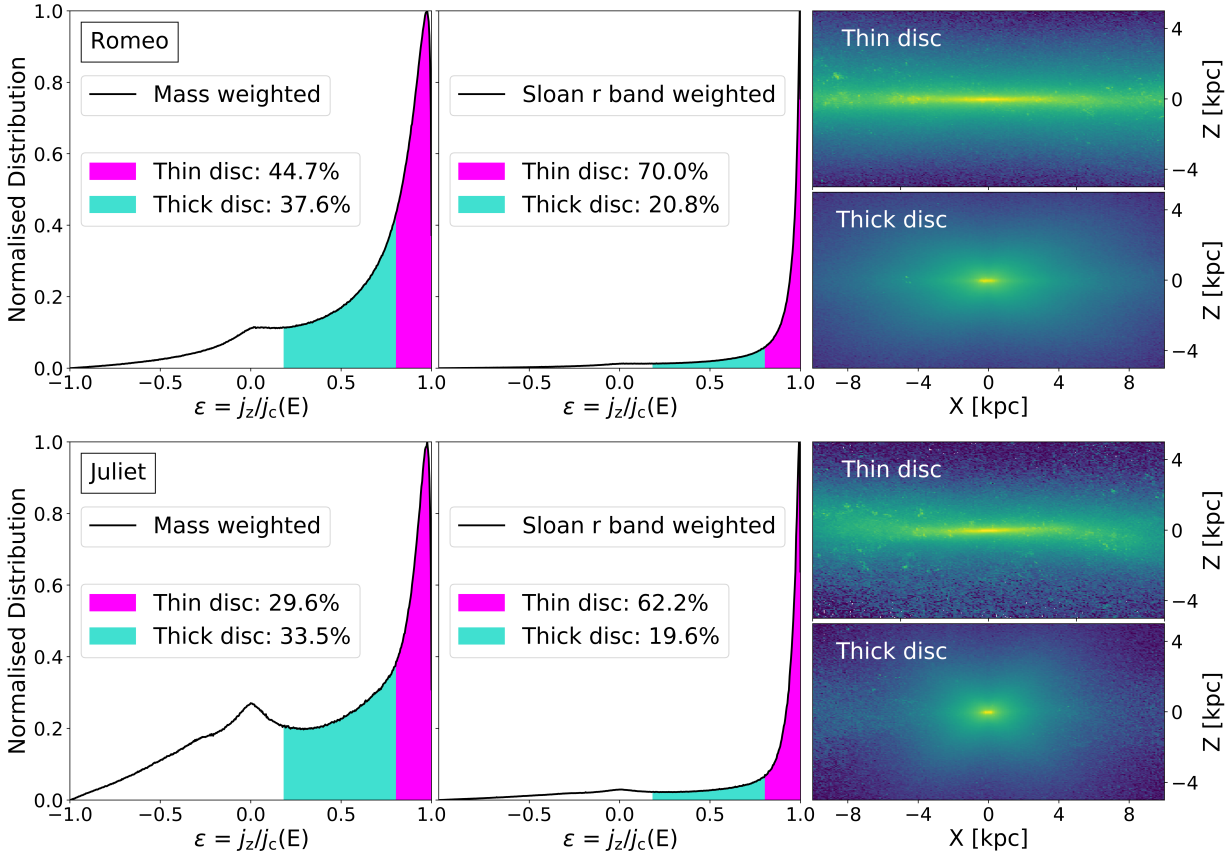

Figure 3.1: Circularity and spatial distributions of stars in `Romeo` (top set) and `Juliet` (bottom set). The **left panels** show the mass-weighted distribution of circularities ϵ of all the stars within R_{90} in the galaxies (13.3 kpc and 9.6 kpc, respectively). See §**??** for a description of ϵ. The magenta blocks mark thin disc stars, which we define as the stars with $\epsilon \geq 0.8$. The cyan blocks mark thick disc stars, which we define to be those with $0.8 > \epsilon \geq 0.2$. The fraction of stars in each block is shown in the legend. The **middle panels** show the same distributions but now weighted by the Sloan r band luminosity of each star particle. The luminosity-weighted distributions generally give a much higher thin-disc fraction. The percentages indicate mass- and luminosity-weighted fractions for each component. The **right panels** display $z = 0$ edge-on views (2D density weighted by Sloan r band luminosity) of the thin (upper) and thick (lower) disc stars. We see that these definitions produce disc components that qualitatively resemble geometrically-defined thin and thick discs.

weighted circularity distributions and the middle panels show the luminosity-weighted circularity distributions for each galaxy. By our definitions, the magenta regions correspond to thin-disc stars, whilst the cyan regions correspond to thick-disc stars. Note that whilst the mass-weighted distributions yield approximately equal thin and thick disc populations, the luminosity-weighted distributions assign $\sim$60$-$70% to the thin disc. The right panels show luminosity-weighted images of the thin and thick disc populations for each galaxy, which illustrate that our orbit-based definitions yield spatial distributions that look qualitatively like discs that are indeed thin and thick.

We find that our ϵ-based classification scheme results in thin and thick disc populations with vertical density profiles (in the z direction) resembling those of traditional morphologically identified thin and thick discs. Whilst some of our galaxies have vertical profiles better fit by exponential forms, the majority prefers $sech^2$ fits. At mock solar locations (8 kpc from the galactic centre), fits to the resultant thin-disc populations yield scale heights for our 12 galaxies that range from $\sim$250 pc to $\sim$800 pc for luminosity-density profiles (in Sloan r band); and from $\sim$500 pc to $\sim$950 pc for mass-density profiles. Similar fits to our thick-disc populations have scale heights that range from $\sim$1.2$-$1.5 kpc for luminosity-density profiles. These results are consistent with previous analyses of FIRE simulations [147, 200]. We find that dividing populations in this manner yields scale-height results in line with those we obtain with more traditional (purely spatially-based) two-component fits. We also find that our simple ϵ-based classification yields thick disc populations that are older, more metal poor, and more alpha enhanced than the thin discs we identify (not shown).

We note that there can be a non-trivial fraction of stars that exist at very low or negative circularities ($\epsilon < 0.2$), which would naturally be associated with a spheroidal component. For example, in Figure 3.1, for `Romeo` (`Juliet`), this component represents 17% (37%) of the mass and 6.8% (13%) of the light. We generally find that these spheroidal stars tend to form in the earliest periods of galaxy assembly, whilst thick-disc stars form later. Since

the focus of this paper is on thin/thick disc formation, we have largely ignored low/negative angular momentum stars in what follows, though further investigation into the origin of the inner spheroid as it relates to star formation in the early galaxy is warranted. Such an exploration would require a more sophisticated kinematic disc/spheroidal classifications of stars with overlapping ϵ ranges. We have performed a simple check of the sensitivity of our main results to the presence of bulge stars by neglecting all stars that sit within 1 kpc of the galactic center of each galaxy and find that this does not change our results substantially. The fraction of stars that have $\epsilon > 0.2$ and that sit within 1 kpc is relatively small in all of our galaxies and, when either excluded or included, have only a minor effect on the age distributions of our "thick disc" stars.

3.3 Results

3.3.1 Two Illustrative Cases: `Romeo` and `Juliet`

The top panels in Figure 3.2 show the star formation histories of `Romeo` (left) and `Juliet` (right) as a function of lookback time. The star formation rate [2] (SFR) displayed is averaged over both a short timescale of 10 Myr (SFR_{10}, blue) and a longer timescale of 500 Myr (SFR_{500}, red). The middle panel shows the variance in "instantaneous" SFR, σ_{10}, divided by the average SFR_{500} as a function of lookback time. We define $\sigma_{10}(t)$ as the variance in SFR_{10} over a time range spanning $t \pm 250$ Myr. We see that the relative variance is much larger at early times than at late times, consistent with previous studies [216, 83] that have shown that star formation in massive FIRE-2 galaxies tends to transition from bursty to steady as we approach the present day.

[2] These star formation histories are measured for all particles that were born within 20 kpc of the most massive progenitor.

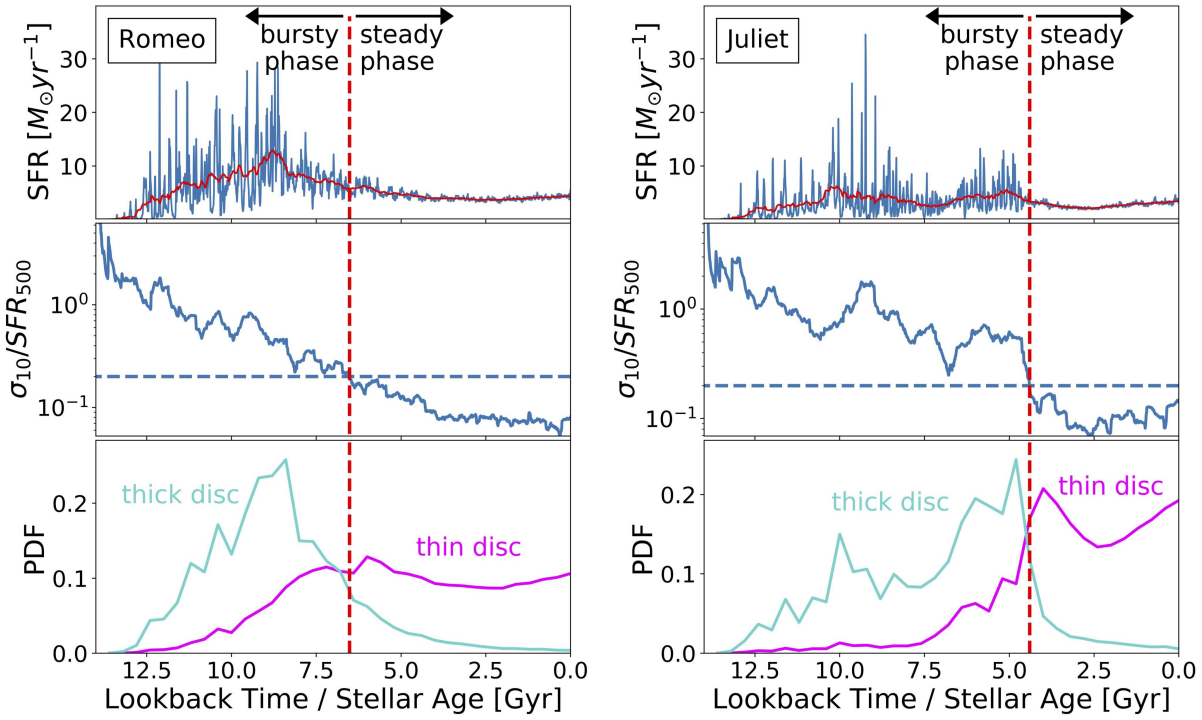

Figure 3.2: Star formation histories and thin/thick disc stellar age distributions for `Romeo` (left) and `Juliet` (right). The **top panels** show the star formation rate in the galaxy as a function of lookback time. The blue lines show the "instantaneous" star formation rate averaged over 10 Myr bins, while the red lines show the "smoothed" star formation rate averaged over 500 Myr bins. The **middle panels** shows the variance in instantaneous star formation rate divided by the smoothed star formation rate as a function of time. We see that the SFR variance in each galaxy generally decreases with time, from bursty to steady, as we approach the present day. For ease of description, we divide the star formation history of each galaxy into two distinct phases – an early bursty phase and a late steady phase – delineated a time $t_{\rm B}$ where the SFR variance falls below 0.2 times the smoothed star formation rate. This "bursty-phase lookback time" is marked by the vertical red dashed line in each upper panel. The **bottom panels** shows the age distribution of $z = 0$ stars that belong to the thick disc (cyan) and thin disc (magenta) in each galaxy. We see that thick-disc stars have ages that track closely the bursty period of star formation while thin-disc stellar ages correspond more closely to the steady phase.

While the transition from bursty to steady is not always sharp, the trend is quasi-monotonic, with the the ratio $\sigma_{10}/\mathrm{SFR}_{500}$ generally decreasing with time. For the sake of simplicity in this analysis, we find it useful to divide the star formation history of each galaxy into two distinct phases: an early bursty phase and a late-time steady phase. We define the bursty phase to end at a lookback time t_{B} when the variance in "instantaneous" star-formation rate first falls below $B = 0.2$ times the time-averaged star formation rate:

$$\frac{\sigma_{10}(t_{\mathrm{B}})}{\mathrm{SFR}_{500}(t_{\mathrm{B}})} \equiv B. \tag{3.1}$$

We use this definition to assign a specific bursty-phase timescale to each galaxy's star formation history. Our qualitative results are not sensitive to the precise choice of $B = 0.2$ on the right-hand side of Equation 3.1. Larger choices ($B > 0.2$) tend to push the bursty phase slightly earlier and smaller choices ($B < 0.2$) tend to push the burst phase slightly later. By our adopted definition, `Romeo` has a bursty-phase lookback time of $t_{\mathrm{B}} = 6.5$ Gyr and `Juliet` has a bursty phase that ends more recently at $t_{\mathrm{B}} = 4.4$ Gyr. The vertical, red-dashed lines in Figure 3.2 mark these times. Table 3.1 and Table 3.2 provide bursty-phase lookback times t_{B} for our simulated galaxies.

The bottom panels in Figure 3.2 show the age distributions of thick-disc stars (cyan) and thin-disc stars (magenta). Thick-disc ages tend to track the bursty-phase star formation, whilst the thin disc stars closely track the steady phase in each case. We emphasize again that in defining a specific value for t_{B} we do not mean to suggest that there is always a razor-sharp phase-change in star formation activity (or in disc thickness) but rather to assign a specific timescale to each galaxy that reasonably marks a qualitative transition. We note that age-overlap of thick and thin disc stars in `Romeo` is much more significant than it is in `Juliet`. This mirrors the more gradual decrease in relative SFR variance in `Romeo`, compared to the sharp transition near t_{B} seen in `Juliet`. Nevertheless, the broad tendency for typical

thick disc stellar ages to correlate with bursty-phase lookback times is seen for every galaxy in our sample (as we show in §3.3.3 below).

Morphology with time

Figure 3.3 and 3.4 show images of `Romeo` and `Juliet` at three specific times in the past: 8.4, 4.7, and 2.7 Gyr ago, which also illustrate how stars that formed at these epochs are spatially distributed today. The top row (a) shows the star formation rate versus time. The arrow symbols on the time axis indicate the specific lookback times visualized beneath. Row (b) shows luminosity-weighted images of the main progenitor of each galaxy at the specified times. Each snapshot is viewed edge-on with respect to the stellar angular momentum axis at that time. Row (c) includes images of the young stellar populations, corresponding to stars born within the last 100 Myr of the indicated times. Lastly, row (d) shows the current location ($z = 0$) of the young stars shown in (c). Note that rows (c) and (d) are similar to Figure 1 in Ma et al. 2017 [147].

Figure 3.3 shows that, 8.4 Gyr ago (prior to the end of the bursty phase) `Romeo` resembled a thick disc embedded within a significant spheroid. The stars forming at this time (panel c, far left) are not very well ordered into a thin disc, but do exhibit some coherence. Those stars today are arranged in a thick-disc like configuration (d, far left). Conversely, at 4.7 Gyr and 2.7 Gyr (after the steady phase has commenced) `Romeo`'s thin disc has fully emerged. Young stars at those times are situated in thin discs (c, middle and right) and remain in relatively thin configurations at $z = 0$ (d, middle and right).

Figure 3.4 shows that `Juliet` exhibits a transition from thick to thin, which happens later than `Romeo`'s. Concretely, whilst `Romeo` had a pronounced thin disc component 4.7 Gyr ago, `Juliet` had no thin disc at that time. Only in the most recent image (2.7 Gyr) does `Juliet` begin to resemble a thin disc. This difference in morphological structure with time

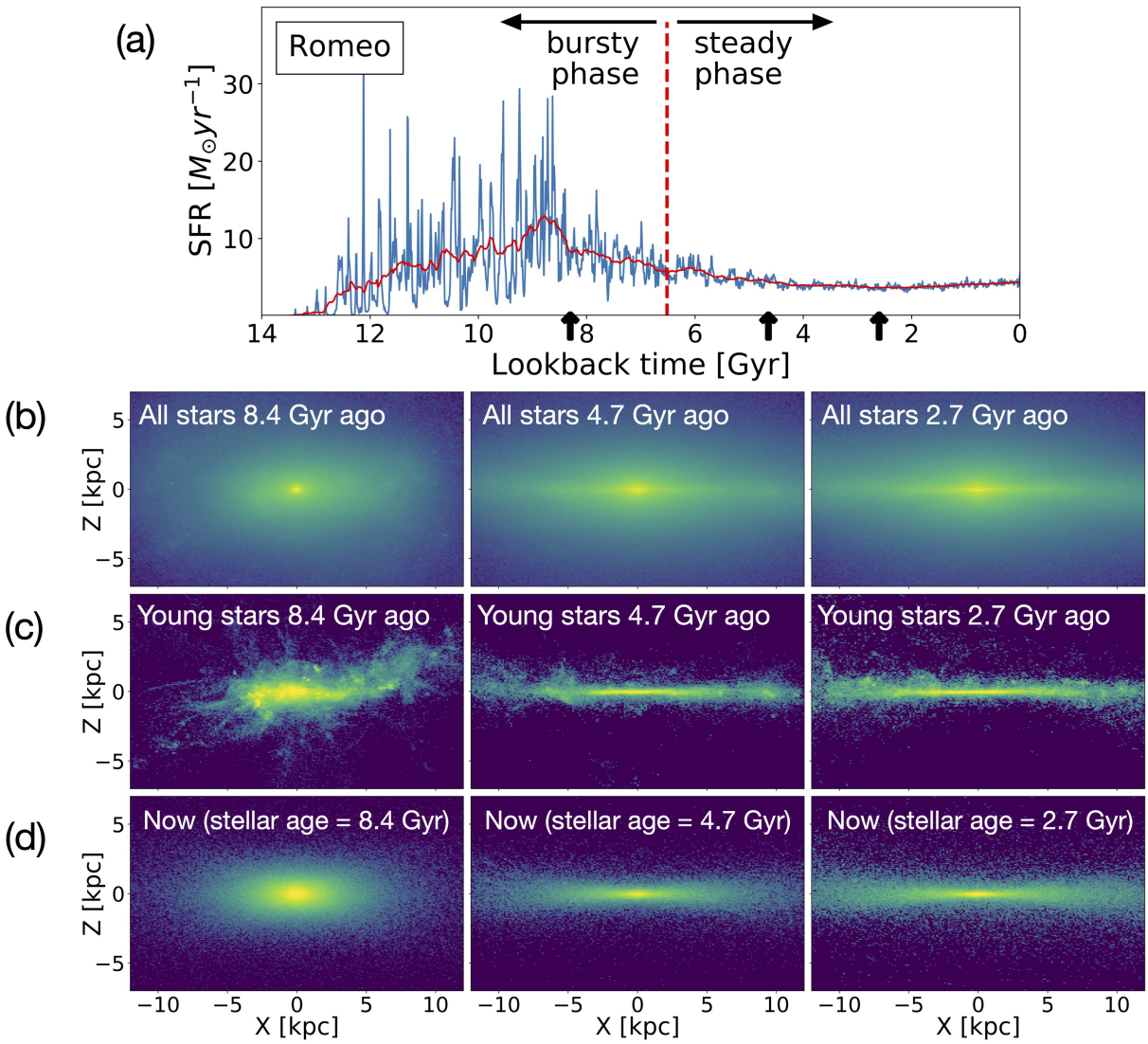

Figure 3.3: (a) Instantaneous (blue) and smoothed (red) star formation rate for `Romeo` plotted as a function of lookback time. The vertical red dashed line shows our adopted time that separates the bursty phase from the steady phase according to Equation 4.1. (b) Edge-on, luminosity-weighted images for `Romeo` at three different lookback times – from left to right: 8.4 Gyr, 4.7 Gyr, and 2.7 Gyr. The arrows along the time axis in top panel indicate these times. (c) Edge-on, luminosity-weighted images for the youngest population (formed within 100 Myr) at the same times. (d) Edge-on, luminosity-weighted images at $z = 0$ for the same stars shown in row c. Note that 8.4 Gyr ago, when the star formation was still bursty, the galaxy resembles a thick disc. At the later two times, in the steady phase, a thin-disc component emerges.

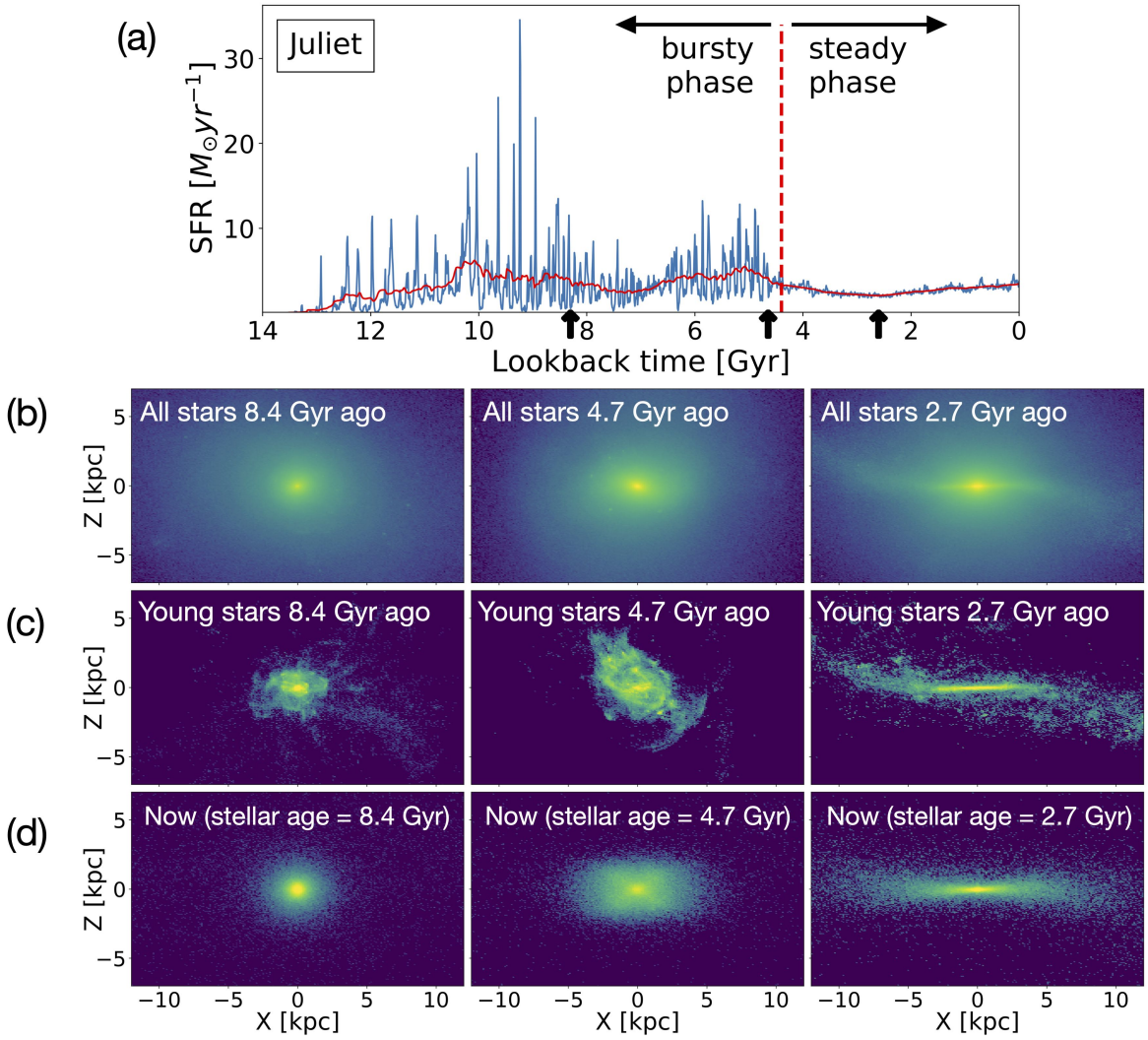

Figure 3.4: Same as Figure 3.3, now for `Juliet`. At 8.4 Gyr and 4.7 Gyr ago, when `Juliet`'s star formation was still bursty, there is no visible thin disc. Only in the 2.7 Gyr images, after the steady phase has started, is thin-disc morphology apparent.

mirrors the difference we see in the transition to steady star formation. `Juliet` has a bursty phase that ends only at a lookback time of $t_{\rm B} = 4.2$ Gyr, compared to `Romeo`, which ended its bursty phase $t_{\rm B} = 6.7$ Gyr ago. At 4.2 Gyr, `Juliet` happens to have just experienced a rapid inflow of cool gas, some of which has formed stars in the thick, rotating structure we see in row (c), middle panel. Those stars end up in a thick disc component at $z = 0$ (row d, bottom).

The 8.4 Gyr and 4.7 Gyr panels in Figure 3.4 for `Juliet` show differences in morphology with time that are representative across our larger simulated sample. Specifically, we find that the bursty phase itself can be further divided into two periods of morphological development: 1) a very early, chaotic bursty phase, where even the youngest stars (< 50 Myr) have angular momenta that are misaligned with the existing stars in the galaxy; and 2) a later, quasi-stable "bursty-disc" phase, where some short-lived angular momentum cohesion exists. As shown with an example in the next section, we find that stars that are born very early on, when the SFR is *very* bursty, tend to be born with spheroidal-type orbits (with peaks in the ϵ distribution ranging from $0 - 0.3$). Stars that are made during the later, quasi-stable bursty-disc phase, tend to be fairly coherent for a short period of time, with circularity distributions within $\sim$50 Myr of their birth that straddle thin/thick disc characteristics (peaking with $\epsilon \sim 0.6 - 0.8$). These bursty-disc stars are quickly heated to thicker-disc orbits within $\sim$100 Myr (similar to the behavior reported by Meng & Gnedin 2021[160]). This later heating appears to be a result of bursty feedback and chaotic accretion. Similar components could also be found based on stellar populations at $z = 0$ using a Gaussian mixture model [167].

Because this paper focuses on thin- and thick-disc formation, we have refrained from presenting results on early *in-situ* spheroid formation, though this would be an interesting topic for future work. It is worth noting that, when weighted by luminosity, the spheroidal components contribute minimally to the total light in our galaxies at $z = 0$.

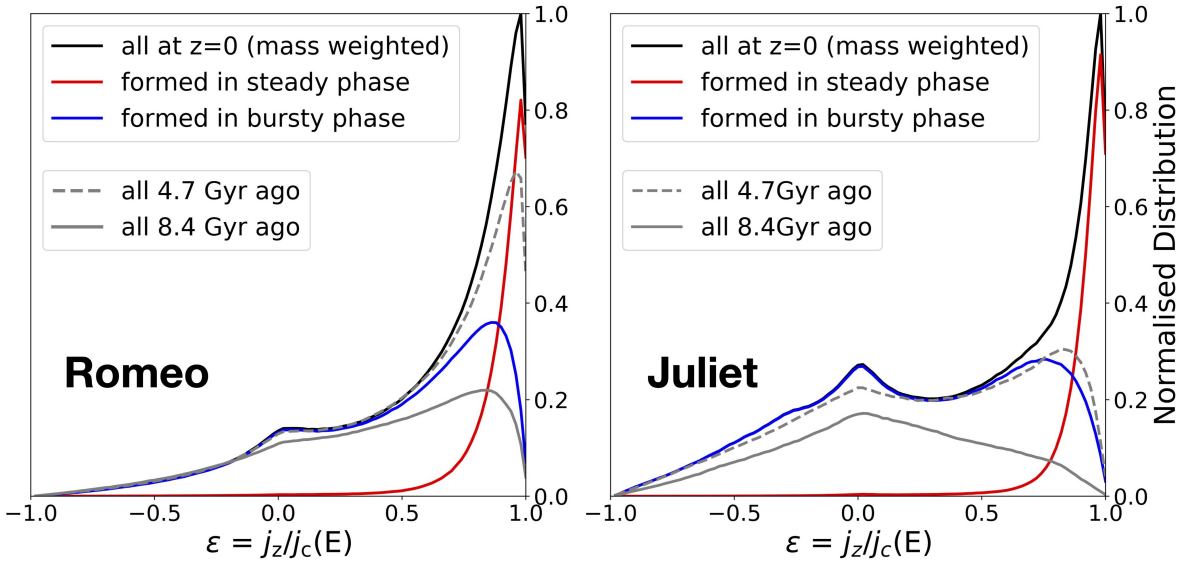

Figure 3.5: Circularity distributions for stars in `Romeo` (left) and `Juliet` (right). The solid black lines in each case show the mass-weighted distribution of stellar circularities (ϵ) for all stars within R_{90} of each galaxy (13.3 kpc and 9.6 kpc, respectively) at $z = 0$. The solid red and blue lines correspond to stars formed in the steady star formation phase and the bursty phase, respectively. In each galaxy, stars that formed during the steady phase have high circularities, peaked near $\epsilon = 1$. Stars formed during the bursty phase are much less ordered, with a coherent rotation peak at $\epsilon \lesssim 0.8$, indicative of thick-disc kinematics. The gray solid and dashed lines show *total* mass-weighted star-particle distributions for the main progenitors of each galaxy 8.4 Gyr ago and 4.7 Gyr ago, respectively. `Romeo` (left), which ended its bursty phase 6.5 Gyr ago, had already developed a fairly substantial high-angular momentum peak 4.7 Gyr ago (dashed line), whilst `Juliet` (right), which ended its bursty phase only 4.4 Gyr ago, had only a modest thick-disc like peak at the same time. Further back in time, 8.4 Gyr ago, `Romeo` was much less ordered than it is today, but still had a thick-disc-like peak in stellar circularity. `Juliet`, on the other hand, had mostly spheroid-like kinematics, with a circularity distribution centred on $\epsilon \sim 0$, at this time.

Kinematic classification with time

Figure 3.5 shows mass-weighted circularity distributions for star particles in `Romeo` (left) and `Juliet` (right). The black solid lines indicate distributions for *all* stars within R_{90} of each galaxy at $z = 0$. The blue lines indicate the $z = 0$ circularities for stars that formed during the early, bursty phase ($t_{\rm birth} < t_{\rm B}$), whilst the red lines refer to those formed during the later steady phase. Stars that formed during the steady phase are much more circular (thin-disc like) in each case, peaking close to $\epsilon = 1$. The stars that formed during the early

bursty phase show much less coherence in angular momentum, with high-ϵ peaks closer to $\epsilon \sim 0.8$, indicative of thick-disc kinematics. Note that the distributions are normalised such that the sum of the red and blue lines equals the black lines.

The gray curves in Figure 3.5 show the ϵ distributions for all stars in the main progenitor of each galaxy at two different lookback times: 8.4 Gyr ago (gray solid) and 4.7 Gyr ago (gray dashed). These are the same times visualised in the lower left and lower middle panels of Figures 3.3 and 3.4. `Romeo`, which had just finished its bursty phase by 4.7 Gyr ago, had a fairly prominent peak at high circularity at that time. `Juliet`, which was still in its bursty phase at that time, had a less well-ordered angular momentum distribution. Both galaxies were systematically less well-ordered 8.4 Gyr ago than they were 4.7 Gyr ago. Whilst `Romeo` had a small peak near $\epsilon \sim 0.8$, more characteristic of a thick disc component, `Juliet` had a distribution peaked near $\epsilon = 0$, as expected for a spheroidal system. These differences in angular momentum structure mirror the morphological differences between these two galaxies at the same times shown in Figures 3.3 and 3.4.

3.3.2 Late-time mergers and starbursts

Three of our twelve galaxies (`m12b`, `m12c`, and `m12f`) experience late-time mergers after the steady phase has commenced (see Appendix A.3 for details). We define a merger to be an event that impacts the central galaxy (< 20 kpc) with a satellite that had a total mass (baryons and dark matter) greater than $5 \times 10^{10} M_\odot$ when it crossed the inner 50 kpc. We record this as the merger time. Additionally, seven of our other galaxies have mergers of comparable sizes during the bursty phase, but these mergers do not correlate with disc properties in significant ways (see Appendix A.3).

Figure 3.6 illustrates the star formation histories (top panels), total mass (dark matter

[3]The fall-in directions are confirmed with the visualizations of the two simulations.

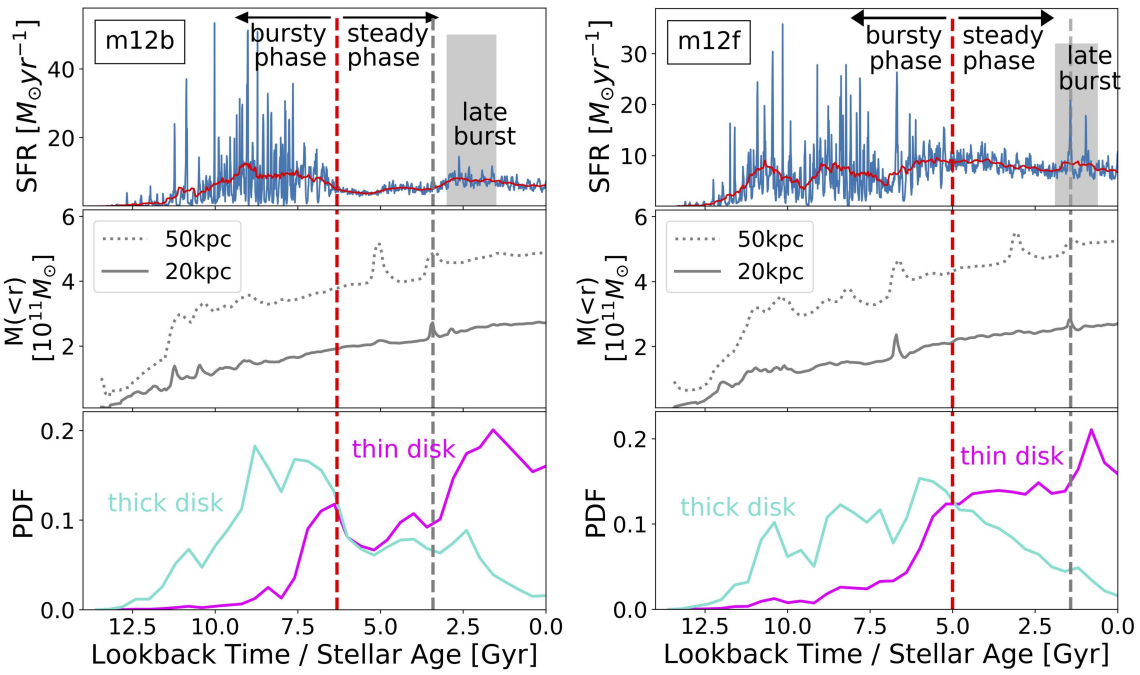

Figure 3.6: Star formation histories, mass assembly histories and thin/thick disc stellar age distributions for `m12b` (left) and `m12f` (right). These are examples of galaxies with late-time bursts triggered by minor mergers (shaded gray bars). The **top panels** show the star formation rate in each galaxy as a function of lookback time. The blue lines show the "instantaneous" star formation rated averaged over 10 Myr bins, while the red lines show the "smoothed" star formation rate averaged over 500 Myr bins. There are two distinct phases in the star formation history for each galaxy, an early bursty phase and a late steady phase. We divide the two at a time $t_{\rm B}$, which we define as the time when the variance in instantaneous star formation rate falls below 0.2 times the smoothed star-formation rate. This "bursty-phase lookback time" is marked by the vertical red dashed line in each upper panel. The gray bands indicate late-time bursts of star formation that occur during the steady phase. The **middle panels** show the total mass of central galaxies within 50kpc (grey dotted) and 20kpc (grey solid), respectively, as a function of lookback time. From the mass assembly history, we see that the fairly significant burst in `m12f` was triggered by a late-time, prograde, LMC-size merger. The smaller burst in `m12b` was also triggered by the final coalescence of a merger, of similar size, but this time on a polar orbit[3]. We record the first central impact time of this type of mergers and mark with grey dashed lines in the plot. The **bottom panels** show the age distribution of $z = 0$ stars that belong to the thick disc (cyan) and thin disc (magenta) in each galaxy. We see that thick disc stars have ages that track closely the bursty period of star formation while thin-disc stellar ages correspond more closely to the steady phase. Stars made in the late-time bursts appear to populate the thin disc primarily, but some stars end up in the thick disc as well. The burst age is proceeded by an enhanced tail of slightly older thick-disc stars, which is consistent with what would be expected from disc heating. These events do not change appreciably the median age of thick disc stars but do enhance the post-steady-phase tail of the thick-disc stellar age distributions compared to cases without late bursts (compare to Figure 3.2).

plus baryons within 50 kpc and 20 kpc) evolution (middle panels), and disc component age distributions (bottom panels) associated with `m12b` (left) and `m12f` (right). The bottom panel splits the age distribution into thin (cyan) and thick (magenta) disc stars. `m12b` experiences a polar-orbit merger with a gas-rich, LMC-size satellite ($\sim 10^{9.5}$ $M_\odot$ in baryons, $\sim 10^{11}$ $M_\odot$ in dark matter) that coalesces at the time of the late-burst marked. The more prominent late-burst in `m12f` is associated with a merger with a satellite of a similar mass, but this time on a prograde orbit.

These late-time mergers and associated bursts do not change broad correlations we find between bursty-phase lookback time and thin-disc fractions and *median* thick-disc ages. However, they do enhance the age distribution of the youngest thick-disc stars. The lower panels of Figure 3.6 include examples of this effect, where the thick-disc age distributions are not as sharply truncated after the bursty phase as they are in Figure 3.2. This seems mostly to arise from heating associated with the merger, but feedback from the burst could also contribute. Interestingly, the burst also coincides with a peak in the *thin-disc* stellar age distribution. Many of the stars that form in these bursts apparently retain thin-disc orbits. That gas-rich mergers can promote stellar-disc formation is a well-known phenomenon [193, 142, 141]. Santistevan et al. 2021 [201] use the same simulations we analyze here to show that existing metal-poor stars and low-metallicity gas deposited in LMC-size mergers can explain the existence of low-metallicity prograde stars in the Milky Way [207].

One of our twelve galaxies (`Thelma`) experiences a late-time burst ($\sim$1 Gyr lookback time) that is *not* associated with a merger. This appears to be a stochastic event associated with the fact that `Thelma` has only recently settled down to $\sigma_{10}/\mathrm{SFR}_{500} < 0.2$ at $t_\mathrm{B} = 2.6$ Gyr. Unlike the majority of our galaxies, `Thelma` does not settle down to a variance much smaller than 0.2; so the "burst" by our formal definition looks more like a stochastic event. Only one other galaxy in ours sample, `m12w`, never really settles down ($t_\mathrm{B} = 0.0$ Gyr) – its variance in instantaneous SFR around $z = 0$ is still ~ 0.3.

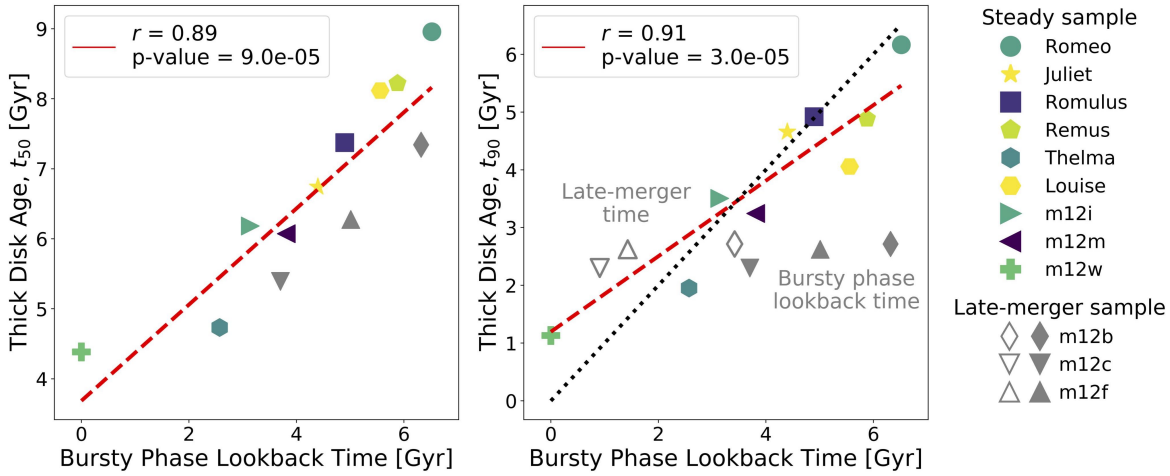

Figure 3.7: Correlation between the bursty-phase lookback time and thick disc age for our entire sample. The gray points correspond to galaxies that experience late-time minor mergers after the steady phase has begun. **Left:**. Median thick-disc age (t_{50}) versus the lookback time to the end of the bursty phase. The legend (far right) displays a unique symbol type per galaxy. The dashed-red line shows a linear fit to the relation. The Pearson correlation coefficient ($r = 0.89$) is boxed in the upper left. The typical age of a thick-disc star correlates quite strongly with the end of the bursty phase. **Right:** Age of ninetieth percentile youngest thick-disc star (t_{90}) versus the lookback time to the end of the bursty phase (solid points). The solid gray points – those with late-time mergers – clearly lie on a different relation than the coloured points, suggesting that the late bursts influence and populate the young-star tail of the thick disc population. The open points are the same galaxies, now depicted at the lookback time when the late-time merger occurred. These seem to align fairly closely to a one-to-one line (gray dotted), along with the coloured points. The red dashed line shows a linear fit to the open gray and coloured points.

3.3.3 Sample-wide trends

Thick disc age

Using four illustrative examples, Figures 3.2 and 3.6 suggest that the ages of kinematically-identified thick-disc stars at $z = 0$ tend to track the period of bursty star formation in these galaxies. The left panel of Figure 3.7 demonstrates that these trends hold for our entire sample. Displayed is the median age of thick-disc stars (t_{50}) versus the bursty-phase lookback time ($t_{\rm B}$) for each galaxy. The correlation is quite tight, with more recent bursty phases associated with younger thick-disc ages. Note that $t_{\rm B}$ along the horizontal axis is

determined entirely from the star formation history of the galaxy and includes no dynamical information whatsoever, and thus the observed correlation is nontrivial. For example, if thick discs were formed primarily from initially thin discs that were heated by mergers, we would expect no such correlation.

The typical (median) thick-disc star was formed approximately 3 Gyr prior to the end of the bursty phase. The red-dashed line shows the best-fit linear relation:

$$t_{50} = 3.7 + 0.69 t_{\rm B}, \tag{3.2}$$

where times are assumed to be in units of Gyr. The Pearson correlation coefficient for the points in the left panel is $r = 0.89$ with p-value $= 9.0 \times 10^{-5}$. Although not shown, we find that that the average age of thick disc stars produces a very similar trend with bursty-phase lookback time as the median age displayed here. Given that the thick-disc population is primarily born during the bursty phase, it is natural to ask if the youngest thick-disc stars allow us to age-date the end of the bursty phase in a one-to-one way. We find that this is true only for the nine of our twelve galaxies that *do not* have a late-time merger during the steady phase.

The right panel of Figure 3.7 shows the age of the ninetieth percentile youngest thick-disc star (t_{90}) versus the bursty-phase lookback time (solid points). The dotted gray line shows the one-to-one relation for reference. The gray symbols refer to galaxies with late-time mergers, which clearly deviate from the trend. The one galaxy in our sample that experiences a late-time burst not triggered by a merger (`Thelma`, coloured pentagon) does not deviate significantly. The open gray symbols use the lookback time to the late-time merger as the horizontal coordinate. With this choice, the points fall along a fairly tight relation (with Pearson correlation coefficient of $r = 0.91$ and p-value $= 3.0 \times 10^{-5}$). The dashed red line

shows a linear fit to the coloured and open points (with solid gray points ignored):

$$t_{90} = 1.2 + 0.65 t_{\rm B}, \tag{3.3}$$

where times are assumed to be in unites of Gyr.

The gray points in the left panel of Figure 3.7 represent galaxies with late-time mergers. This group tends to track the relation, but also tend to lie systematically below the average trend with respect to median age. This is consistent with the interpretation that the young-star tail of the thick-disc population has been populated by stars formed after the end of the bursty phase. Nevertheless, the fraction of stars populated in this way is small enough ($\lesssim 10\%$) that the broad trend with median age and bursty phase lookback time is preserved.

Given that the youngest thick-disc stars may be associated with either the end of the bursty phase or a late-time merger, it maybe be difficult to use the age of the youngest stars to easily date the end of the bursty phase. In principle, one could look for features in the age distribution of thick-disc stars to gain insight on these questions (see Figure 3.6 where the bursty lookback time does seem to imprint a feature in the age distribution of thick-disc stars). However, it will likely be more straightforward to use the typical age (median or average) of thick-disc stars to estimate the lookback time corresponding to the end of the bursty phase and the beginning of the steady phase (independent of the recent merger activities).

Thin disc fraction

Figure 3.8 shows the correlation between bursty-phase lookback time and thin-disc fraction, with each symbol type mapped to a specific galaxy name (far-right legend). The left panel employs a mass-weighted thin-disc fraction, whilst the right panel uses as luminosity-

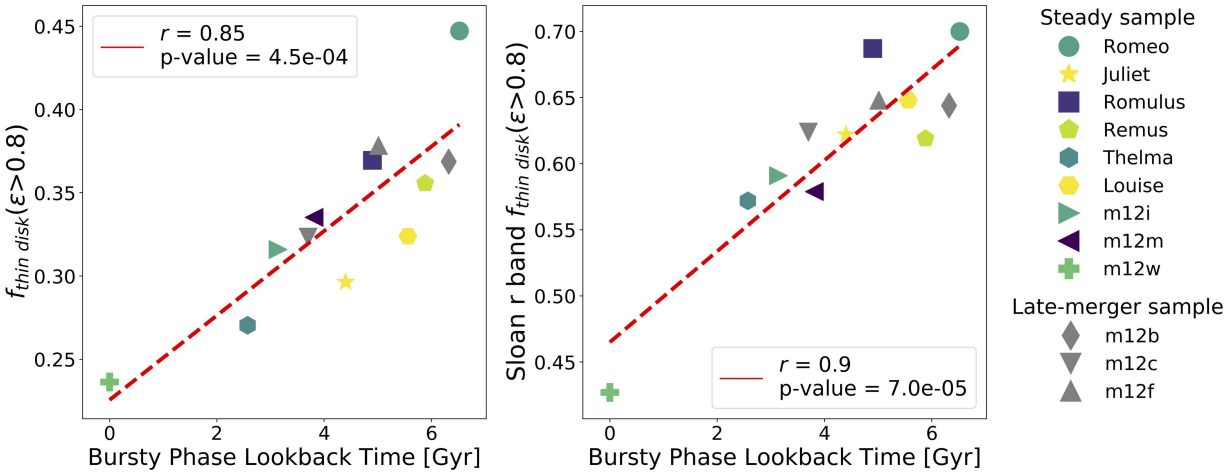

Figure 3.8: Correlations between the bursty-phase lookback time and the thin-disc fraction. **Left:** Mass-weighted thin-disc fraction versus bursty-phase lookback time for each run. The legend on the far-right relates each symbol to a unique galaxy in our sample, in the same manner as Figure 3.7. **Right:** Luminosity-weighted thin-disc fraction versus bursty-phase lookback time. In both panels, galaxies with longer lookback times to the bursty phases (and hence the longer-lasting steady phases) have more pronounced thin disc. The red-dashed line in each panel shows a linear fit to the points. The corresponding Pearson correlation coefficient is listed. The correlation is significant ($r > 0.8$) in each case, even though we have included no information on the relative average rate of star formation in the bursty (thick-disc) phase compared to the steady (thin-disc) phase. As in Figure 3.7, we present the runs that have a recent minor mergers in gray. There is no significant difference between these runs and the others in the thin-disc fraction at fixed bursty-phase lookback time.

weighted thin-disc fraction. The red lines show linear fits to the data points. In each case, the correlation is strong, but with scatter, with Pearson correlation coefficients of $r = 0.86$ (mass weighted) and $r = 0.88$ (luminosity weighted). Both p-values (3.9×10^{-4} and 1.6×10^{-4}, respectively) are much less than the significance level.

We see that the earlier the lookback time to the transition, the more prominent the thin disc is. It makes qualitative sense that the longer stars are created in the "settled" phase, the larger the fraction of thin disc stars we would see. At fixed thin-disc fraction, we see $2 - 3$ Gyr scatter in the lookback time to the bursty phase. It would be surprising, however, if this relation were any tighter, as it contains no information on the absolute star formation rates in either phase. Specifically, at fixed lookback time to the transition, the higher the average star formation rate during the thin-disc/steady phase compared to the thick-disc/bursty phase, the more prominent the thin disc would be. We see that this trend generally holds for our galaxies. For example, if we examine the star formation histories in Figure 3.6 for galaxies `m12b` and `m12f`, we see that `m12b` has a higher smoothed-average star formation rate during the bursty phase than it does during the steady phase. Conversely, `m12f` has a similar smoothed-average star formation rate before and after the transition. This means that `m12b` will be making fewer thin-disc stars per unit time during the steady phase than `m12f`. This explains why `m12b` has a thin-disc fraction (0.64 in luminosity) that is slightly *lower* than `m12f` (0.65), even though its steady phase lasts more than one billion years longer (7.34 Gyr vs. 6.28 Gyr).

CGM virialisation and steady star formation

The physical origin of the progression from early, bursty and less kinematically-ordered star formation to late-time, steady star formation in thin discs is not clear. An important clue comes from the work of Stern et al. 2021 [216], who used FIRE-2 simulations to show that the bursty to steady transition in galaxy star formation coincides with virialisation of the

inner CGM. They quantify inner CGM virialisation using the ratio of the cooling time of shocked gas $t_{\rm cool}^{\rm (s)}$ to the free-fall time $t_{\rm ff}$ at an inner radius $r = 0.1R_{\rm vir}$. When $t_{\rm cool}^{\rm (s)}/t_{\rm ff} \gtrsim 1$ the inner CGM is smooth and largely supported by thermal pressure. In contrast, when $t_{\rm cool}^{\rm (s)}/t_{\rm ff} \lesssim 1$, the inner CGM has large pressure fluctuations and is highly dynamic. Using a sample of sixteen zoom simulations with halo masses ranging from $\rm M_{halo} = 10^{10.6} - 10^{13}$ $\rm M_\odot$, Stern et al. 2021 [216] shows that gaseous discs become rotationally supported and star formation transitions from bursty to steady at roughly the time when the ratio first becomes $t_{\rm cool}^{\rm (s)}/t_{\rm ff} > 2$. Their sample included four of the twelve galaxies we consider here.

In this brief subsection, we extend the Stern et al. 2021 [216] analysis to the additional haloes in our sample and confirm their reported trends. Using the same definitions of free-fall time and cooling time described in section 2.1 of their paper, we show that inner CGM virialisation at the time when $t_{\rm cool}^{\rm (s)}/t_{\rm ff} = 2$ generally coincides with our bursty to steady SFR transition at $\sigma_{10}/\rm SFR_{500} = 0.2$ (Eq. 3.1). This is demonstrated in Figure 3.9, where we show the evolution of the inner virialisation parameter (right axis, orange line) and the burstiness parameter (left axis, blue line) as functions of lookback time for six example haloes. Not only do the transition timescales coincide in each case, but the monotonic progressions of each parameter tends to evolve inversely with the other in time. At early times, when gas flows are prone to cooling instabilities and clumpy accretion, the star formation is more bursty. At late times, when cooling times are long and the flow can be relatively smooth and well-mixed, star formation tends to be more constant. We find similar behaviors hold for every halo in our sample.

The proceeding analysis demonstrates that as the inner CGM of our galaxies virialises, the star formation becomes less bursty (Fig. 3.9). This is also the time when stars tend to be formed with thin-disc kinematics (Fig. 3.7). One hypothesis that explains this, suggested by Stern et al. 2021[216], is that a virialised inner CGM enables the formation of stable discs because a hot and uniform halo can pressure-confine disruptive superbubbles driven by

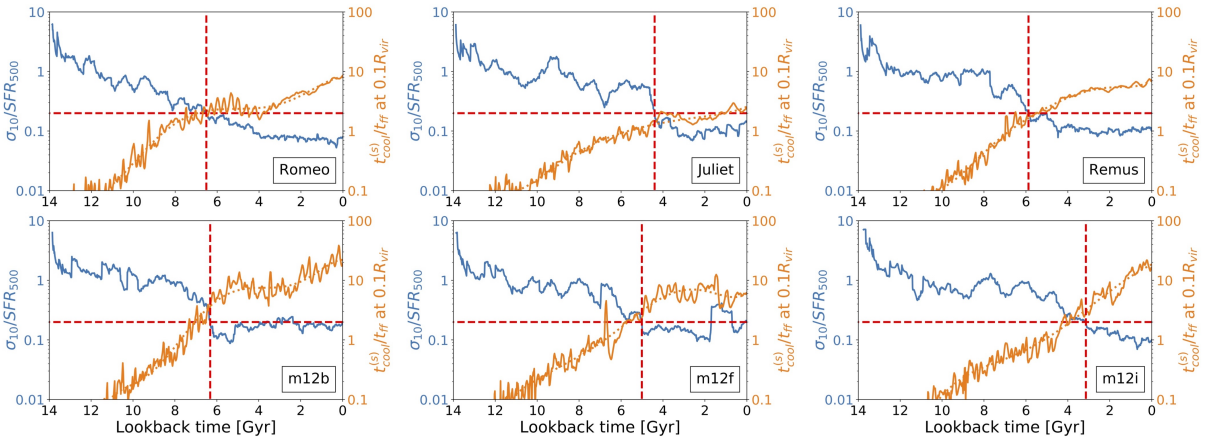

Figure 3.9: Parameters that track star-formation burstiness (blue) and inner CGM virialisation propensity (orange) as functions of lookback time for six of our haloes. As described in §3.3.3, the orange lines (right axis) show the cooling time to free-fall time ratio measured at $0.1R_{\rm vir}$ as a function of lookback time. The blue lines (left axis) shows the variance in instantaneous star formation rate divided by the smoothed star formation rate as a function of time. The horizontal red dashed line marks the threshold above which the inner CGM virialises, $t_{\rm cool}^{\rm (s)}/t_{\rm ff} \approx 2.0$, as defined in Stern et al. 2021 [216]. The axes are set so that the same line corresponds to $\sigma_{10}/{\rm SFR}_{500} = 0.2$, which we have adopted in this paper to define the end of the bursty phase. The bursty-phase lookback time $t_{\rm B}$ defined in this paper is marked by the vertical red dashed line. Note that the same time roughly corresponds to the time when the inner CGM becomes virialised.

clustered supernovae. Another possibility is that smooth and well-mixed accretion enables more coherently aligned angular momentum at the time of accretion onto the galaxy [104]. These issues are important topics for further exploration.

3.4 Discussion and Conclusions

We investigate the formation of the stellar thin and thick disc components using twelve FIRE-2 zoom-in simulations of Milky-Way-mass galaxies. Our main findings include the following:

- Each galaxy experiences an early period of bursty star formation that transitions into a steady phase, with a relatively constant star formation rate at late times. The transition time corresponds to the time when the inner CGM becomes sub-sonic and virialises (Figure 3.9).
- The transition from bursty to steady star formation correlates with a shift in the formation of stars with thick-disc kinematics to thin-disc kinematics (Figures 3.2, 3.3, and 3.4).
- The lookback time to the end of bursty phase ranges from $t_{\rm B} = 0.0 - 6.5$ Gyr in our sample. This time correlates strongly with the median age of thick disc stars at $z = 0$ (Figure 3.7).
- Galaxies with longer steady phases (larger $t_{\rm B}$) tend to have higher thin-disc fractions (Figure 3.8).

Three of our twelve simulations have appreciable late-time mergers that occur after the steady (thin-disc) phase has commenced. These mergers are not responsible for the bulk of

thick-disc stars, though they do heat some disc stars and populate the young-star tail of the thick disc population demonstrated in Figure 3.6 and the right panel of Figure 3.7.

The fact that our discs emerge thick and become thinner over cosmic time is consistent with previous findings of "upside-down" disc formation [34, 36, 28, 164, 29, 147, 178]. However, our result that the transition is associated with a transition in star formation activity – from bursty to steady – adds a new element to this discussion. That FIRE simulations of Milky-Way-mass haloes experience such a transition in star formation activity is not a new result [162, 213, 9, 78]. The onset of the steady phase appears to be related to the virialisation of the inner CGM [216, and Figure 3.9]. A hot, pressurised CGM may stabilise the disc against supernovae-driven outflows and enable thin-disc formation [216]. If correct, this interpretation opens the possibility of using stellar archaeology to learn about the origin of the Milky Way's CGM and its associated history of star-formation modes.

Whilst a more observationally-oriented comparison is required to interpret our results for the Milky Way confidently, it is tempting to explore some potential implications based on naïve comparisons to published estimates of the Galactic thick-disc age distribution [110, 212, 155, 108, 210]. Most estimates suggest that the Milky Way thick-disc has a median age of ~ 9 Gyr, with few stars younger than 6 Gyr. Such an age distribution is most similar to our `Romeo` simulation (Figure 3.2), which transitioned from bursty to steady star formation ~ 6.5 Gyr ago. This simple comparison would suggest that the Milky Way transitioned at a similar time, commensurate with the virialisation of its inner hot halo. If this is the case, then prior to that time, the Milky Way lacked a dominant thin disc component, was forming stars in a bursty manner, and had non-virialised inner CGM.

Related to our analysis, Bellardini et al. 2021 [19], using the same set of simulations, finds that gas disc metallicity in-homogeneity was dominated by azimuthal variations at high redshift but then transitioned to being dominated by radial gradients at lower redshifts, which has also been reported in the previous analysis in the FIRE-1 simulations across a much

wider galaxy mass range [146]. The transition epochs after which radial variations dominate over azimuthal scatter agree broadly well with our measurement of the transitions from bursty to steady phase. Although there is significant scatter and some time delay between the measurements of two transition times, it shows some potential observable implications of the bursty/steady transition for galactic archaeology.

Some cosmological galaxy formation simulations, including those that demonstrate upside-down disc formation [178], do not have early bursty star formation phases of the kind we witness in our models. This may partially be due to star formation threshold employed. Burstiness is suppressed in simulations with modest threshold densities (~ 10 cm^{-3}) for star formation, whereas our simulations require ~ 1000 cm^{-3} (see Benítez-Llambay et al. 2019 [25]; Dutton et al. 2019 [64] for a related discussion). Given this, chemical tracers among the various Galactic kinematic components may provide a means to test star formation prescriptions. Other factors like the ISM model, local star formation efficiency and the stellar feedback model might also play a role. Future work in this direction will be illuminating.

Chapter 4

Born this way: thin disc, thick disc, and classical bulge formation in Milky-Way-mass galaxy simulations

4.1 Introduction

Why some stars in galaxies are arranged in discs while others inhabit more spheroidal distributions stands among the most basic questions in galaxy formation. Remarkably, while easily formulated, a definitive answer to this question remains elusive. The Milky-Way (MW) mass scale is of particular interest: $M_\star \simeq 5 \times 10^{10} M_\odot$ sits near the crossover point, above which massive galaxies are typically early-type and spheroidal, and below which galaxies become more disc-dominated and late-type [16]. Indeed, the MW-mass regime demonstrate significant variance in morphological structure [85, 132, 3, 17].

Three broad morphological components of galaxies are thin discs, thick discs, and central bulges [55, 223, 42, 234, 226]. Bulges can be further delineated into flattened, mildly rotating

pseudo bulges or more spheroidal *classical bulges* [135, 90]. Most stars in classical bulges appear to be formed at high redshift, with only minor growth at late times [189]. Thin discs are systematically younger and more metal rich than both bulges and thick discs [235, 47].

One popular idea for explaining galaxy morphology is to posit that rotationally-supported disc galaxies emerge early in cosmic evolution [114, 192, 219, 136] and act as a universal starting point for subsequent morphological evolution. In this scenario, thick discs and bulges arise both from secular evolution and from mergers. A second possibility is that highly-ordered, thin-disc galaxies arise late in cosmic assembly, an "inside-out/upside-down" formation scenario [36, 28, 231, 236]. Here, discs first emerge thick and clumpy [72, 208, 95, 177, 71] and only later does star formation begin to occur primarily in extended thin discs [128]. Bulge formation in such a picture could arise from an early, turbulent phase of galaxy assembly [e.g., 70].

The rotational and structural properties of pseudo bulges are strongly indicative of a formation channel linked closely to disc formation and/or disc/bar evolution [58, 214, 134, 171]. Classical bulges, on the other hand, appear to be less connected to disc properties and it remains unclear if their formation is connected or completely disjoint from disc assembly. Specifically, while traditional scenarios posit that classical bulges emerge from the mergers of discs [225, 119, 127], there are growing indications that bulges can form in multiple ways and bulge mass does not appear to be linked closely to galaxy merger history [17]. Rapid gas inflow to the galaxy center could fuel classical bulge formation [202] directly, as could the migration of giant gaseous clumps at high redshifts [161, 44].

The Milky Way provides a detailed touchstone for testing these ideas. It has both thin and thick disc components [96, 126, 26, 32, 107] in addition to a small classical bulge and a more dominant pseudo bulges [97], which appears to resemble the thick disc in chemical properties and formation time [5, 109, 60]. Recently, chemo-dynamical data sets have started uncover exciting clues to the origin of the rotating components of the Galactic disk. Belokurov &

Kravtsov 2022 [22] used APOGEE and *Gaia* data to identify a characteristic "spin up" metallicity for Milky Way stars. Specifically, as a function of metallicity, *in-situ* stars show a rapid increase in rotation from a median tangential velocity of $\sim 0\mathrm{km\,s^{-1}}$ (typical of a spheroid) to $\sim 100\mathrm{km\,s^{-1}}$ (typical of a *thick* disk) at [Fe/H] $\simeq -1$. This feature may point to transition epoch from disordered kinematics to increasingly coherent rotation. Similarly, Conroy et al. 2022 [49] have used H3 Survey spectroscopy and *Gaia* astrometry to identify a transition time where star formation efficiency rapidly increased while simultaneously stellar kinematics become more disc-like.

The present work explores the formation and evolution of stellar disc (thin and thick) classical bulge populations using FIRE-2 zoom simulations of Milky Way size galaxies. It builds upon a series of papers examining the relationship between star formation burstiness, stellar kinematics, and the development of a hot gaseous halos in FIRE-2 simulations of galaxy formation [216, 236, 103, 104]. One striking discovery has been a connection between internal galaxy properties and the mode of gas deposition from the circum-galactic medium (CGM) into the interstellar medium (ISM) [216]. As galaxy halos evolve from low mass to high, the inner CGM virialises, star formation transitions from "bursty" to "steady", and stellar-driven galaxy-scale outflows are suppressed. The bulk of thick disc material forms prior to this transition, and this gives rise to a tight correlation between the ages of thick disk stars and the end of the bursty phase [236]. CGM virialisation also drives an abrupt change in the angular momentum coherence of accreting gas [104]. Only after this time do stars form along a single long-lived plane in circular orbits, making possible the formation of a *thin* disc [236, 104]. Conversely, during the earliest epochs, the ISM has a quasi-spheroidal morphology, and negligible rotation support [103]. Internal dynamics of this kind may naturally give rise to classical bulge formation.

4.2 Simulations and methods

4.2.1 FIRE-2 simulations of Milky-Way-mass galaxies

Our analysis utilises cosmological zoom-in simulations performed with the multi-method gravity plus hydrodynamics code GIZMO [116] from the Feedback In Realistic Environments (FIRE) project[1]. We rely on the FIRE-2 feedback implementation [120] and the mesh-free Lagrangian Godunov (MFM) method. The MFM approach provides adaptive spatial resolution and maintains conservation of mass, energy, and momentum. FIRE-2 includes radiative heating and cooling for gas across a temperature range of $10 - 10^{10}$K. Heating sources include an ionising background [79], stellar feedback from OB stars, AGB mass-loss, type Ia and type II supernovae, photoelectric heating, and radiation pressure – with inputs taken directly from stellar evolution models. The simulations self-consistently generate and track 11 elemental abundances (H, HE, C, N, O, Ne, Mg, Si, S, Ca, and Fe), and include sub-grid diffusion of these elements in gas via turbulence [117, 218, 75]. Star formation occurs in gas that is locally self-gravitating, sufficiently dense (> 1000 cm^{-3}), Jeans unstable and molecular (following Krumholz & Gnedin 2011 [137]). Locally, star formation efficiency is set to 100% per free-fall time; i.e., $\mathrm{SFR_{particle}} = \mathrm{m_{particle}} \cdot \mathrm{f_{mol}} \,/\, \mathrm{t_{ff}}$. Gas particles are converted to stars at this rate stochastically [129]. Note that this does *not* imply that the global efficiency of star formation is 100% within a giant-molecular cloud (or across larger scales). Self-regulated feedback limits star formation to ∼1-10% per free-fall time [79, 118, 174].

In this work, we analyse 5 Milky-Way-mass galaxies (Table 4.1) in detail. These zoom simulations are initialised following Oñorbe et al. 2014[170]. Three of these galaxies (with names following the convention `m12*`) are isolated and part of the Latte suite [229, 93, 118, 92]. Two, with names associated with the famous duo (`Romeo` and `Juliet`), are part of the ELVIS on FIRE project [92, 94] and are set in Local-Group-like configurations, as in the ELVIS suite

[1] `https://fire.northwestern.edu/`

Table 4.1: The simulations we employ in this work. We list the following: the name of the zoom-in target halo, the stellar mass ($M_\star$) within the central 20 kpc of the halo at $z = 0$, the radius (R_{90}) enclosing 90% of $M_\star$, the halo virial mass ($M_{\rm halo}$), the halo virial radius ($R_{\rm halo}$), the resolution of each simulation quantified by the initial baryonic particle mass ($m_{\rm i}$), and the reference that first introduced each halo at the quoted targeted resolution. We also present the derived quantity: the lookback time to the end of the bursty phase/onset of the steady phase ($t_{\rm B}$). Hosts with names starting with 'm12' are isolated configurations selected from the Latte suite, whilst the rest are in LG-like pairs from the ELVIS on FIRE suite. The two galaxies marked with an asterisk correspond to minor mergers taking place after the onset of the steady phase. The haloes are ordered by decreasing $t_{\rm B}$, from $t_{\rm B} = 6.52$ Gyr (`Romeo`, top) to $t_{\rm B} = 4.40$ Gyr (`Juliet`, bottom).

Simulation Name	$M_\star$ [$M_\odot$]	R_{90} [kpc]	$M_{\rm halo}$ [$M_\odot$]	$R_{\rm halo}$ [kpc]	$m_{\rm i}$ [$M_\odot$]	$t_{\rm B}$ [Gyr]	Reference
`Romeo`	7.4×10^{10}	13.3	1.0×10^{12}	317	3500	6.52	A
`m12b`*	8.1×10^{10}	9.8	1.1×10^{12}	335	7070	6.32	A
`m12i`	6.1×10^{10}	12.8	9.2×10^{11}	318	7070	5.11	C
`m12f`*	8.6×10^{10}	11.0	1.3×10^{12}	357	7070	4.36	B
`Juliet`	4.2×10^{10}	9.6	8.5×10^{11}	302	3500	4.40	A

Note: The references are: A: [92], B: [93], C: [229].

[91]. This suite includes three simulations in total, containing two MW/M31-mass galaxies each. The main haloes were selected so that they have similar relative separations and velocities as of the MW-M31 pair in the Local Group (LG). Table 4.1 lists the initial baryonic particle masses for each simulation. Latte gas and star particles have initial masses of $7070\,M_\odot$, whilst ELVIS on FIRE has $\approx 2\times$ better mass resolution ($m_{\rm i} = 3500\,M_\odot$). Gas softening lengths are fully adaptive down to $\simeq$0.5$-$1 pc. Star particle softening lengths are $\simeq$4 pc physical and a dark matter force softening is $\simeq$40 pc physical. This enables us to study the dense, multi-phase ISM gas in galaxies in a fully cosmological context.

4.2.2 Define Basic Parameters

Similar to Yu et al. 2021 ([236], hereafter Y21), we classify star particles into different categories using orbital circularity, $\epsilon = j_z/j_c(E)$, defined as the ratio of each particle's angular momentum in the $\hat{z}$ direction to that of a circular orbit with the same energy [2].

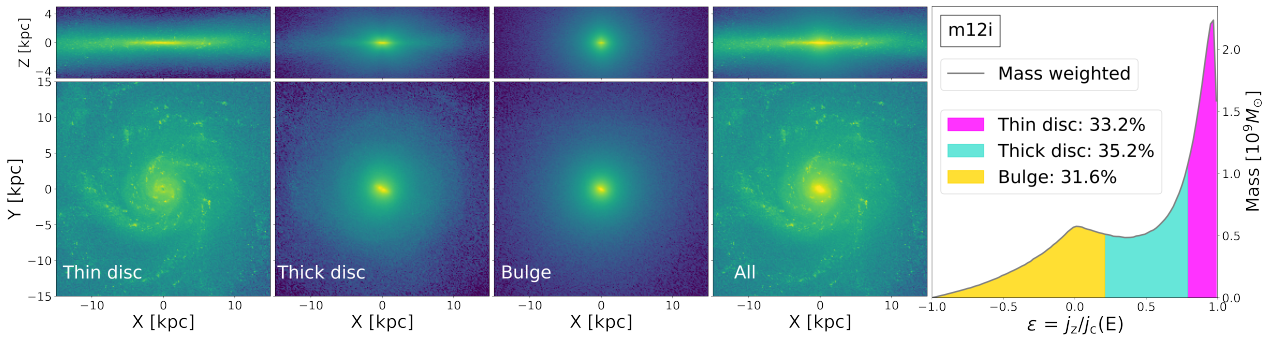

Figure 4.1: Definition and morphology of different components of `m12i` at $z = 0$. Left four panels show the edge-on (top) and face-on (bottom) views (2D density weighted by Sloan r band luminosity) of the thin disc, thick disc, bulge and all stars. Right panel shows the mass-weighted distribution of stellar circularities (ϵ) for all stars within R_{90} (12.8 kpc) at $z = 0$. The magenta block marks thin disc stars, which we define as the stars with $\epsilon \geq 0.8$. The cyan block marks thick disc stars, which we define to be those with $0.8 > \epsilon \geq 0.2$. The yellow block marks bulge stars with $\epsilon < 0.2$. The fraction of stars in each block is shown in the legend. We see that these definitions produce components that qualitatively resemble geometrically-defined discs and bulge.

The angular momentum direction $\hat{z}$ is set by total stellar angular momentum within 10 kpc of each galaxy's center. Stars with $\epsilon = 1$ are on a circular orbit in the plane of the disc; $\epsilon < 0$ implies counter-rotation. We categorise star particles with $\epsilon = 0.8 - 1$ as *thin disc* stars, those with $\epsilon = 0.2 - 0.8$ as *thick disc* stars, and those with $\epsilon = -1.0 - 0.2$ as *bulge* stars. As we show below, we find that circularity appears to be a useful parameter for keeping track of the dynamical evolution of stars over time.

The images shown in Figure 4.1 illustrate how these classifications manifest morphologically. While we have chosen to classify these components using familiar names, it is important to emphasize that those names are traditionally assigned to populations using morphological decomposition rather than dynamical assignment. Nevertheless, as can be seen in the left-most image, our *thin disc* component does indeed resemble thin discs as usually conceived (see Y21 [236] where we discuss scale heights, etc.). Our *thick disc* component consists of a clear vertically-extended disc-like structure, again in keeping with traditional expectations for that name. However, it also contains a central, bright, and mildly rotating distribution of stars that qualitatively resembles the observed characteristics of pseudo bulges [135]. Our

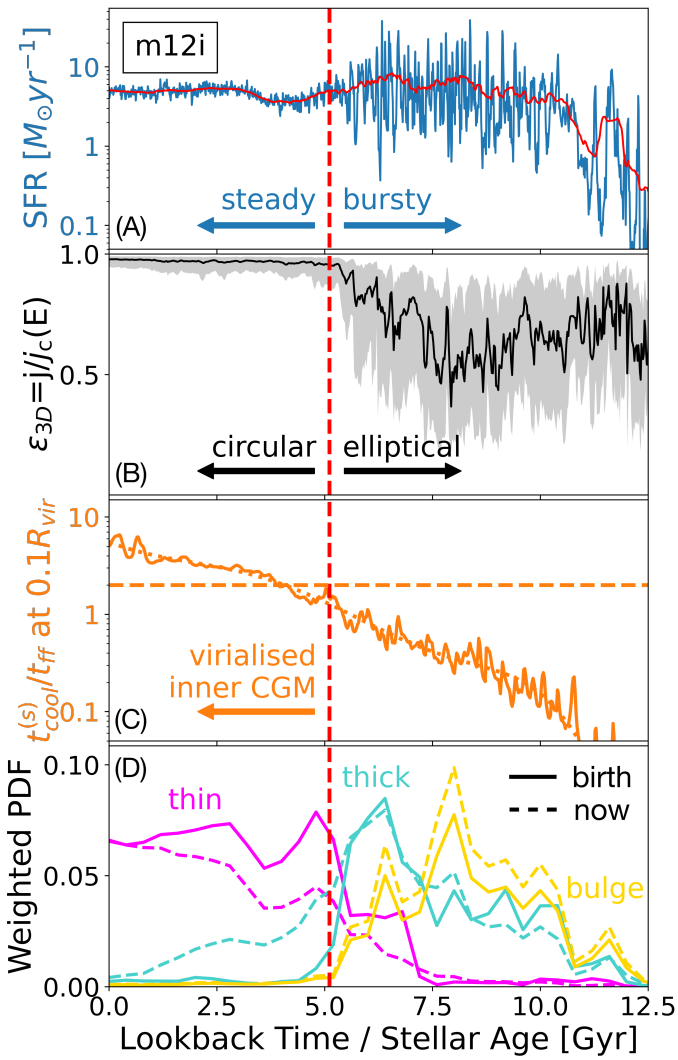

Figure 4.2: Different properties of `m12i` as functions of lookback time. **A:** Star formation rate in the galaxy as a function of lookback time. The blue lines show the "instantaneous" star formation rate averaged over 10 Myr bins, while the red lines show the "smoothed" star formation rate averaged over 500 Myr bins. **B:** The median of 3D orbital circularities $j/j_c(E)$ of stars younger than 100 Myr as a function of lookback time. The shaded region plots the 16th to 84th percentile range. **C:** the cooling time to free-fall time ratio measured at $0.1R_{\rm vir}$. **D:** Age distribution of stars that belong to the thin disc (magenta), thick disc (cyan) and bulge (yellow). Solid lines show the distribution of stars classified by circularity $\epsilon_{\rm birth} = j_z/j_c(E)$ measured at birth while dashed lines show the distribution of stars classified by circularity j_z/j_c measured at $z = 0$.

bulge classification (third from left image) resembles more closely a classical bulge, in that it is not flattened and has a spheroidal morphology (e.g., Gao et al. 2020 [90] and references therein). While we make no direct comparisons to observations in what follows, it is worth keeping in mind that our *bulge* component is most aptly associated with a classical bulge.

In order to make detail analysis on the evolution of the kinematics, we break down orbital circularity ϵ further into 3D orbital circularity, $\epsilon_{3D} = j/j_c(E)$, and alignment angle, $\theta = \arccos(j_z/j)$. Similar to circularity ϵ, 3D circularity ϵ_{3D} is defined as the ratio of each particle's total angular momentum to that of a circular orbit with the same energy. Since a circular orbit has maximal angular momentum for a given energy, 3D circularity ϵ_{3D} ranges between 0 and 1, with $\epsilon_{3D} = 1$ corresponding to perfectly circular orbits, and $\epsilon_{3D} = 0$ to purely radial orbits. Alignment angle θ is defined as the angle between each particle's angular momentum to the rotation axis of the galaxy. It describes how aligned the orbit is with respect to the galactic disc. $\theta = 0°$ corresponds to orbit that lies perfectly in the disc plane. $\theta = 90°$ means that star has a orbit perpendicular to the disc plane. And $\theta = 180°$ indicates that it is counter rotating. While orbital circularity ϵ works decently as a parameter for classification, in order to understand how different aspects of the kinematics change over time, we need the two supplementary parameters as well.

Figure 4.2 shows the evolution of `m12i` for example. The top panel tracks the star formation history of `m12i` as a function of lookback time. The star formation rate [2] (SFR) displayed is averaged over both a short timescale of 10 Myr (SFR_{10}, blue) and a longer timescale of 500 Myr (SFR_{500}, red). Similar to the middle panels in Figure 2 of Y21 [236], the relative variance is much larger at early times than at late times. This is consistent with many previous studies (e.g., [216, 83, 104, 103]) that have shown that star formation in massive FIRE-2 galaxies tends to transition from bursty to steady as we approach the present day. For the purpose of consistency, we use the same parameter, as described in Y21 [236], to

[2]These star formation histories are measured for all particles that were born within 20 kpc of the most massive progenitor.

evaluate the burstiness of the star formation and adopt the same threshold to divide the star formation history of each galaxy into an early bursty phase and a late-time steady phase. We mark the transition time from bursty star formation to steady star formation $t_{\rm B}$ with a vertical dashed red line in the plot.

We define the bursty phase to end at a lookback time $t_{\rm B}$ when the variance in "instantaneous" star-formation rate first falls below $B = 0.2$ times the time-averaged star formation rate:

$$\frac{\sigma_{10}(t_{\rm B})}{\rm SFR_{500}(t_{\rm B})} \equiv B. \tag{4.1}$$

We use this definition to assign a specific bursty-phase timescale to each galaxy's star formation history. Gurvich et al. 2022 [103] uses the running scatter in the SFH in 300 Myr windows, $\sigma_{300\ \rm Myr}(\log(\rm SFR))$, to quantify the fluctuations and define $t_{\rm B}$ as the time after which this quantity remains below 0.3 dex. The difference between different definitions of burstiness results in variations in $t_{\rm B}$ of a few hundreds of Myr. The discrepancy is relatively small compared to the cosmological timescales of the transition, hence we adopt the same method as described in Y21 [236].

The second panel in Figure 4.2 shows the 3D circularity $\epsilon_{\rm 3D}$ of newly-formed stars (ages < 100 Myr) as a function of lookback time. The black line marks the median value while the shaded region shows the 16th to 84th percentile range. Before the star formation settles down, stars form in relatively more radial orbits with large scatter. When star formation becomes steady, those young stars now are born in extremely circular orbit ($\epsilon_{\rm 3D} \sim 1$) with very little scatter.

The third panel in Figure 4.2 shows the inner CGM virialisation $t^{\rm (s)}_{\rm cool}/t_{\rm ff}$ propensity, defined in Stern et al. 2021 [216], as a function of lookback time. Using the same FIRE-2 simulations, Stern et al. 2021 [216] shows that when $t^{\rm (s)}_{\rm cool}/t_{\rm ff}$ is small, cooling time of the shocked gas is much smaller than free-fall time. Thus, shocked gas will cool immediately, lost pressure

support and free fall towards the galaxy. The inner CGM is highly dynamic and has large pressure fluctuations. When cooling time gets larger, compressional heating from the inflows could compensate their radiative losses. Therefore, the shocked gas would remain hot and the inner CGM becomes this smooth "hot halo". The inner CGM virialisation at the time when $t_{\rm cool}^{\rm (s)}/t_{\rm ff} = 2$ generally coincides with our bursty to steady SFR transition. At early time, when gas flows are dominated by different turbulence and clumpy accretion, the star formation is more bursty. Later over time, star formation settles down and gas flows also become relatively smooth and well-mixed.

The bottom panel in Figure 4.2 presents the age distributions of different components identified using circularity $\epsilon = j_z/j_c(E)$. The solid line shows the distribution for the stars classified using birth circularity $\epsilon_{\rm birth}$. We track the approximate birth circularity of each star particle in the simulated galaxy at the time of formation, by post-processing the snapshots saved from the simulation. We define $\epsilon_{\rm birth}$ as the circularity of the star particle in the host galaxy in the first snapshot after it is born. Note that, the angular momentum direction $\hat{z}$ of the galaxy at each snapshot is set by total stellar angular momentum within $0.1R_{\rm vir}$ of each galaxy's center at the time of the snapshot instead of $z = 0$. This method has been verified to produce a steadily evolving reference frame that changes from snapshot-to-snapshot typically on the order of a degree or less in orientation [103]. Using $\epsilon_{\rm birth}$, we find that almost all the thick-disc and bulge stars form in earliest periods of galaxy assembly, whilst thin-disc stars form later after the star formation settles down. The difference between thick-disc and bulge stars is subtle and overall bulge stars identified this way are a bit older than the thick-disc stars as we can see the distribution of thick-disc stars peaks around the time of transition. The dashed lines show the distribution of different populations classified using the circularity ϵ measured at $z = 0$, similar to the method adopted in Y21 [236]. The distributions of bulge stars are almost the same with slight difference in weight. For thick-disc stars, the truncation of the age distribution is more abrupt when using $\epsilon_{\rm birth}$ while there is an extended tail towards younger age for population classified by ϵ. This could

be potentially due to the disc heating effect that heats some thin-disc stars, and thus some stars born with thin-disc like orbits ($\epsilon_{\rm birth} > 0.8$) would end up be in the thick disc regime with $\epsilon = 0.2 - 0.8$. The overall trend from bulge formation to thick-disc formation to thin-disc formation stays the same. There is certain contribution from disk heating or torquing to change the kinematics of the newly-formed stars. But the effect is pretty minimal and negligible, as we quantity it later in §4.3.2.

4.3 Results

4.3.1 Morphology with time

In this section, we show how the morphologies of the simulated galaxies evolve with time and how it is connected to the transition in star formation mode.

Deep-field studies have revealed that galaxies formed at high redshift tend to have irregular morphologies and clumpy discs [70, 177, 176]. At $z = 0$ the vast majority of massive star-forming galaxies show dynamically cool discs, while at higher redshift, those star-forming galaxies are mostly clumpy and irregular. Similar to Figure 3 and Figure 4 in Y21 [236], Figure 4.3 and Figure 4.4 show images of `Romeo` and `Juliet` at five specific times in the past: 2.7, 4.7, 6.3, 8.4 and 10.3 Gyr ago, illustrating how stars that formed at these epochs are spatially distributed today. The top panels show 3D orbital circularity, $\epsilon_{\rm 3D}$, of young stars (ages < 100 Myr) as a function of lookback time. The red lines show the median value of $\epsilon_{\rm 3D}$ when stars form and the black lines show for the same quantity at $z = 0$. Shaded regions plot the 16th to 84th percentile range. The arrows indicate the specific lookback times visualized below and the vertical red dashed line marks the bursty phase lookback time $t_{\rm B}$. The middle and bottom panels display edge-on and face-on images (2D density weighted by Sloan r band luminosity) of the young stellar populations, corresponding to

stars born within the last 100 Myr of the indicated times. While the middle panels show where they were born, the bottom panels show where they are now.

Figure 4.3 shows that, 10.3 Gyr ago (far before the end of the bursty phase), young stars in `Romeo` resembled a significant spheroid. The stars forming at this time (middle panel, far right) are not well ordered and show little coherence, with median 3D circularity $\epsilon_{3D} \sim 0.6$ with large scatter. Those stars today are arranged in a bulge-like configuration (bottom panel, far right). And ~ 2 Gyr later, stars are still forming in a not very ordered way but start to exhibit some coherence. Their morphology today looks more like a thick disc, with median 3D circularity increasing to ~ 0.8. Furthermore, at 6.3 Gyr, 4.7 Gyr, and 2.7 Gyr (after the steady phase has commenced) `Romeo`'s thin disc now has fully developed. Young stars at those times are situated in very thin discs (middle, left three panels) and with extremely high 3D circularity ($\epsilon_{3D} \sim 1.0$). These stars remain in relatively thin configurations at $z = 0$. Their morphology looks like the classic thin disc and 3D circularities are still relatively high but do experience some drop, which we explore later in §4.3.2.

Figure 4.4 shows similar plots for `Juliet`. `Juliet` has experienced a longer bursty phase ($t_B = 4.40$ Gyr) compared to `Romeo`'s ($t_B = 6.52$ Gyr), and it results in the later emergence of the thin disc. While `Romeo` had a pronounced thin disc component already 6.3 Gyr ago, `Juliet` has no thin disc at that time. Only in the most recent snapshot (2.7 Gyr) does `Juliet` start to have young stars forming in a thin-disc like configuration.

The two sample galaxies we show here are representative across our larger simulated samples. We find that there are three stages in the evolution of the FIRE-2 Milky-Way-mass systems over time: 1) a very early, chaotic bursty phase; 2) a later quasi-stable "bursty-disc" phase; and 3) a stable thin-disc phase. The three stages are also marked in the bottom of Figure 4.3 and Figure 4.4. Stage 1 happens at the very early time of the galaxy evolution. Star formation is very bursty and most stars form in radial orbits. Their morphology resembles more a spheroidal system. Those stars now are in a classical-bulge-like configuration. Later,

as it gets more massive with deeper potential well, the host galaxy enters stage 2, where some short-lived angular momentum cohesion exists. Stars born at this stage have more circular orbits and we can see some coherence starting to build up. These stars today make up the thick disc. As star formation settles down, thin disc formation starts to dominate. In the stage 3, young stars are forming in extremely circular orbits ($\epsilon_{3D} \sim 1.0$) and in extremely thin disc. Their morphology today also looks much thinner than stage 2 and stage 3. Because of the longer steady star formation phase in `Romeo`, it also experiences a much shorter stage 3 and stage 2, resulting in a older thick disc and also a higher thin-disc fraction [236]. `Juliet`, instead, stays in stage 3 and stage 2 for a much longer time. Thus, it has a smaller thin disc fraction and a younger thick disc as well.

4.3.2 Kinematics with time

In this section, we quantify the change in the kinematics by tracking the newly-formed stars over time.

Figure 4.5 shows the median and 16th to 84th percentile range of orbital circularity ϵ of the newly-formed stars (ages < 100Myr) as a function of lookback time for `m12i`. The red lines show the median values of ϵ when stars form and the black lines show for the same quantity at $z = 0$. Shaded regions plot the 16th to 84th percentile range. The grey horizontal dashed lines marks the threshold we adopt to identify thin-disc stars. At early times, stars were born with low circularities with large fluctuations, which could be due to both the chaotic, bursty nature of star formation and the swift change in the galaxy's orientation [57]. And their current circularity distribution, after a long time of interaction and evolution, becomes centered around $\epsilon \sim 0$, similar to the distribution of a spheroidal component. This corresponds to the stage 1 of the early chaotic bursty phase discussed earlier in §4.3.1. And approximately 2 Gyr before star formation settles down, the coherence starts to build up

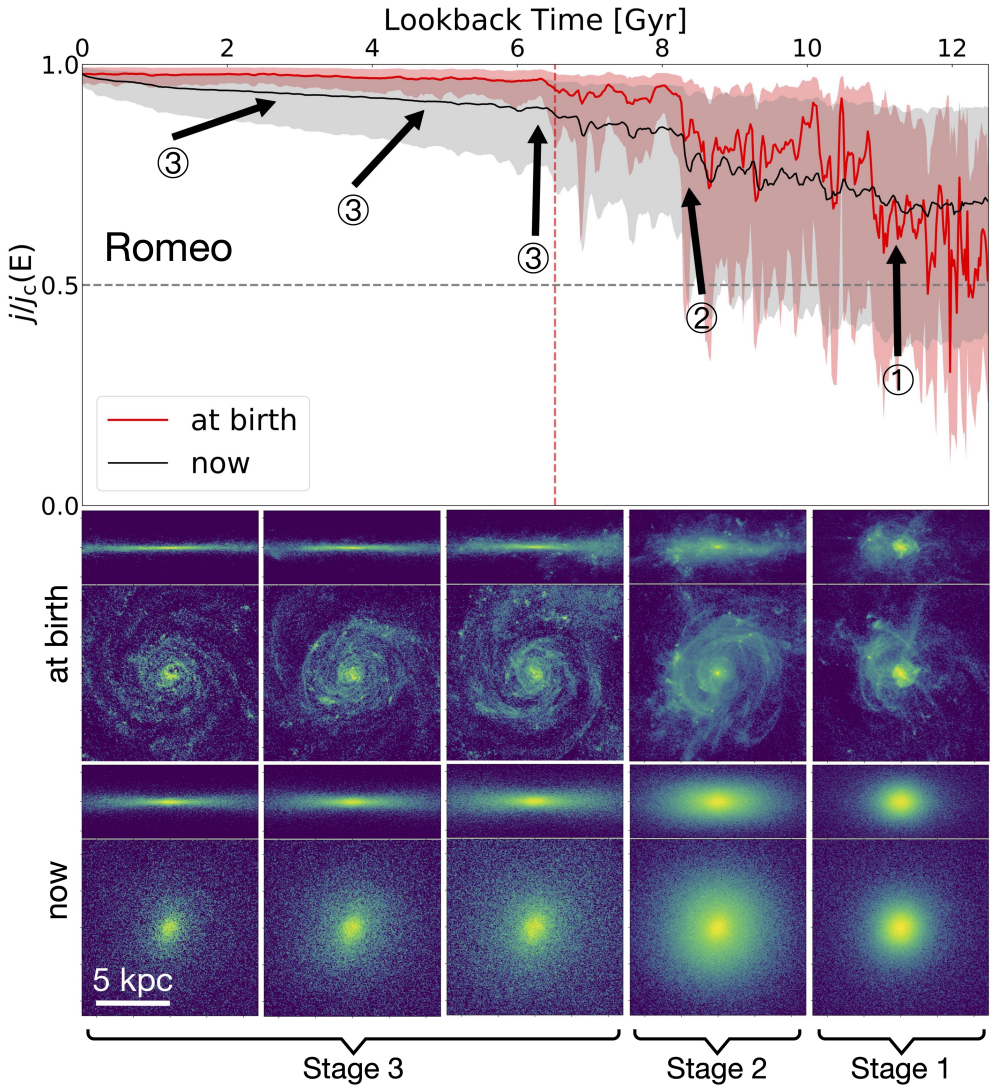

Figure 4.3: Young-star orbits and morphologies across cosmic time for `Romeo`. **Top:** The median and one-sigma range of 3D orbital circularities $\epsilon_{3D} = j/j_c$ of stars younger than 100 Myr as a function of lookback time. The vertical red dashed line shows the bursty phase lookback time. The solid red line and corresponding shaded area are showing for the distributions when they were born while the black line and the grey area are showing for their current distributions. 3D orbital circularities ϵ_{3D} is the ratio of the *total* specific angular momentum in units of the circular angular momentum at the same energy: 0 is purely radial and 1 is perfectly circular. **Middle:** Luminosity-weighted images, both edge-on (top) and face-on (bottom), for the youngest population (formed within 100 Myr) at five different lookback times - from left to right: 2.7 Gyr, 4.7 Gyr, 6.3 Gyr, 8.4 Gyr, and 10.3 Gyr. The arrows in the top panel indicates these times. **Bottom:** Luminosity-weighted images, both edge-on (top) and face-on (bottom), at $z = 0$ for the same stars shown in the middle panels. At early times, stars form on more radial orbits and show clumpy/disordered structures. Their spatial distribution today resembles more like the bulge component. At late times, stars form on circular orbits and show strong coherence. They remain in relatively thin configurations at $z = 0$ as well.

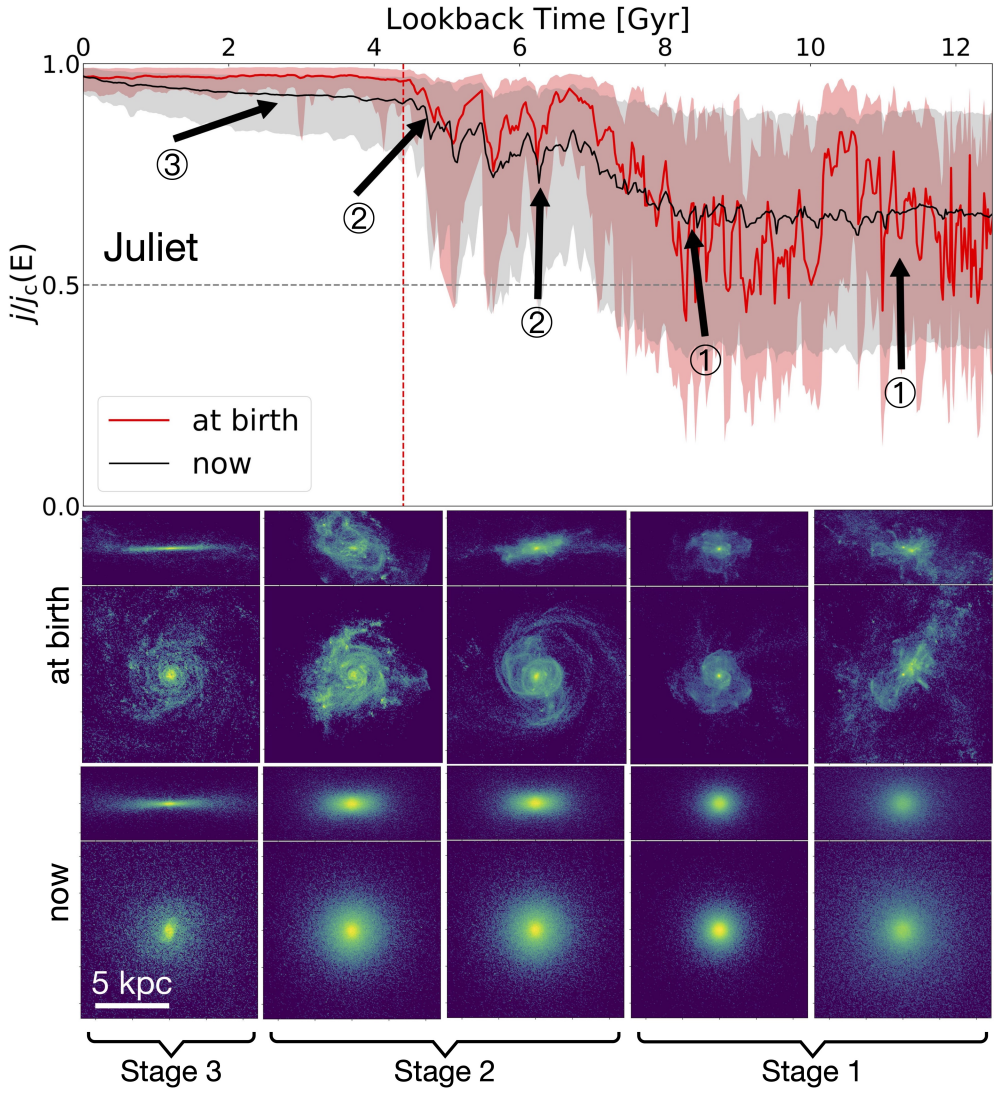

Figure 4.4: Same as Figure 4.3, now for `Juliet`. Note that `Juliet`'s star formation settled down much later than `Romeo`'s. Only in the 2.7 Gyr images, after the steady phase has started, do young stars show thin-disc like morphology.

and the median value of ϵ goes up with some of the stars already surpass our threshold for thin-disc component. The majority of the stars born during this period still fall under the categories of thick disc and central bulge. After the star formation becomes very steady, all the young stars are born in an extremely coherent manner with $\epsilon \sim 1$. The distribution of their current circularity drops a little in value and has larger scatter that straddles thin/thick disc characteristics. This later "thickening" appears to be a result of a combination of both dynamical heating and vertical torquing, which we illustrate later in Figure 4.7, 4.8, and 4.9.

Figure 4.6 shows how the evolution in circularity ϵ affects the classification of different structure components in the galaxy. The left panel is similar to the most right panel of Figure 4.1 but shows for birth circularity $\epsilon_{\rm birth}$ instead. Using the same threshold, stars are classified as thin-disc (magenta), thick-disc (cyan), and bulge (yellow) stars. The fractions of different components are listed in the plot and there are more stars identified as thin-disc when using $\epsilon_{\rm birth}$. In the right panels, we show the distribution of their circularities ϵ now. Stars that are born with high circularities ($\epsilon > 0.8$) tend to maintain their thin configurations today. Their circularity ϵ distribution today still peaks around 0.9 but has a more extended tail towards lower values, which could be due to heating or torquing effect after birth, which we explore more later. For stars identified as thick-disc, their current circularity distribution resembles more like a combination of thick disc and bulge with two peaks around 0.6 and 0. Ideally, bulge population would have symmetric circularity distribution around 0 (marked by grey dashed line in left panel). For the simplicity of this work, we have adopted the straightforward cut in circularity ϵ and it inevitably introduces some uncertainty in our sample classification. A fraction of stars identified as thick disc could actually be part of the bulge and thus contribute to this peak around $\epsilon = 0$. Bulge population has current circularity distribution symmetric around $\epsilon = 0$ and has almost 0 net rotation in the disc plane, which matches the expectation for a spheroidal component. The difference between including the stars with $\epsilon = 0.0 - 0.2$ is minimal since statistically only a very small fraction of stars fall in this region (yellow block above the grey dashed line) would be thick-disc stars.

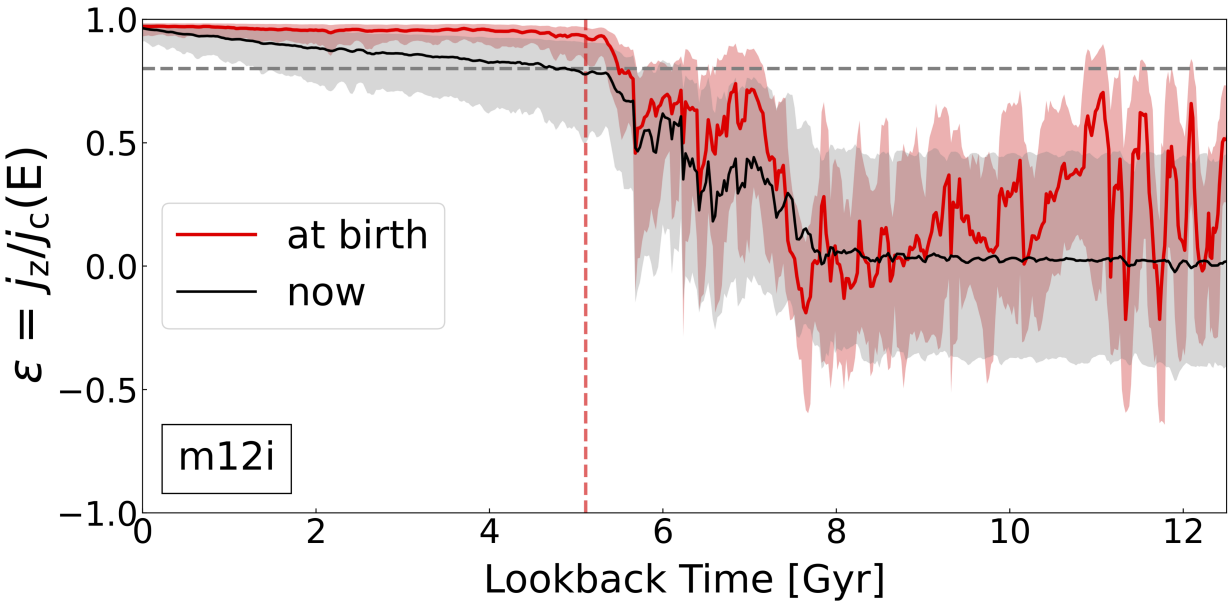

Figure 4.5: The median and one-sigma range of orbital circularities $\epsilon = j_z/j_c(E)$ of stars younger than 100 Myr as a function of lookback time for `m12i`. The vertical red dashed line shows the bursty phase lookback time. The solid red line and corresponding shaded area are showing for the distributions when they were born while the black line and the grey area are showing for their current distributions. The horizontal grey dashed line marks the threshold above which stars are classified as thin-disc stars. At early times, stars tend to be born with spheroidal-type orbits and stay in the same type of orbits with the median value of both birth and current circularity centered around 0. At late times, stars form on more thin-disc like orbits. Subsequently, some stars get heated, as we can see the black line locates a little lower than the red line and the grey bands are also wider than the red bands.

Overall, we observed the trend that stars born with bulge-like orbits tends to stay in the spheroidal configuration with little net rotation. And most of the thin-disc stars today, they were very likely born with even "thinner" orbits.

Figure 4.7 shows the evolution of circularity ϵ of different mono-age stellar populations in `Romeo`, `m12b`, `m12i`, and `m12f`. We trace star particles born within 100 Myr range and calculate the median value of circularity ϵ. Lines are coloured by the stellar age of the population and the dashed parts indicate that the host galaxy was still in its bursty phase at that time while solid parts show for the steady phase. The colorbars are set that all the populations formed during the bursty phase are colored red while the populations formed during the steady phase are colored blue. The two grey dashed lines mark our thresholds for

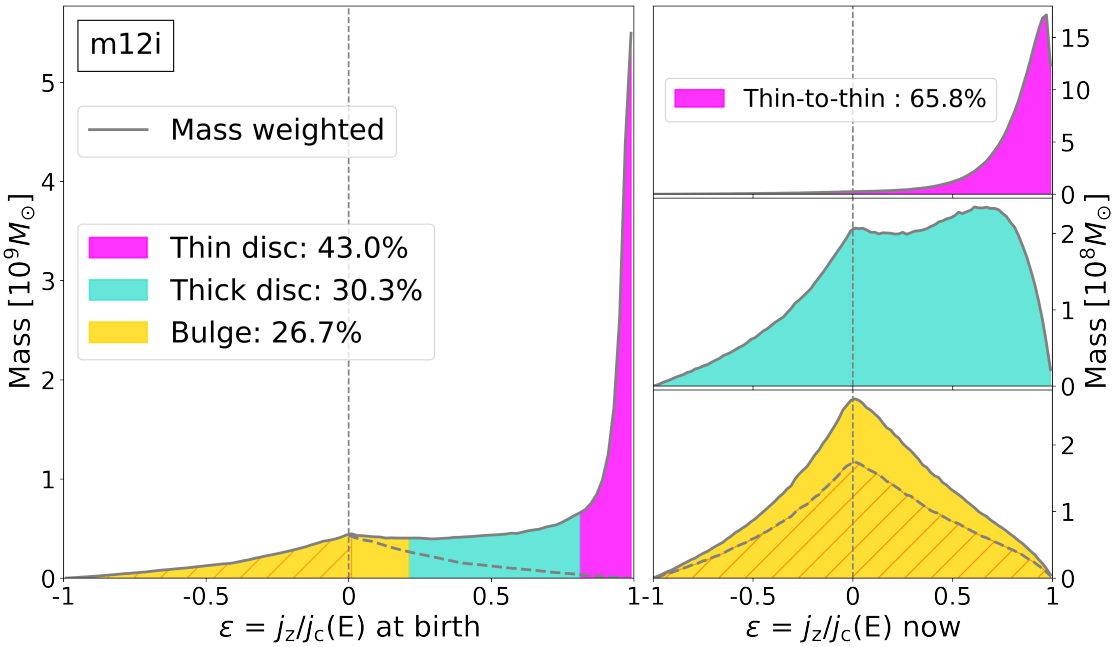

Figure 4.6: **Left:** Birth circularity $\epsilon_{\rm birth}$ distribution for stars within R_{90} (12.8kpc) for `m12i`. The magenta block marks thin disc stars, which we define as the stars with $\epsilon_{\rm birth} \geq 0.8$. The cyan block marks thick disc stars, which we define to be those with $0.8 > \epsilon_{\rm birth} \geq 0.2$. The yellow block marks bulge stars with $\epsilon_{\rm birth} < 0.2$. The fraction of stars in each block is shown in the legend. **Right:** Circularity ϵ distribution for different populations marked in the left panel. Most of the stars born with thin-disc like orbits stay thin. The distribution (magenta block) does have a longer tail towards lower circularity, which is possibly due to the disc heating effect but 65.8% of the stars still have current circularity greater than 0.8. The distribution of the stars identified as thick disc (cyan block) in the left panel resembles more of a combination of thin disc and bulge population. And the distribution of identified bulge stars is a nearly symmetric distribution around $\epsilon = 0$ with a slight preference on prograde orbits.

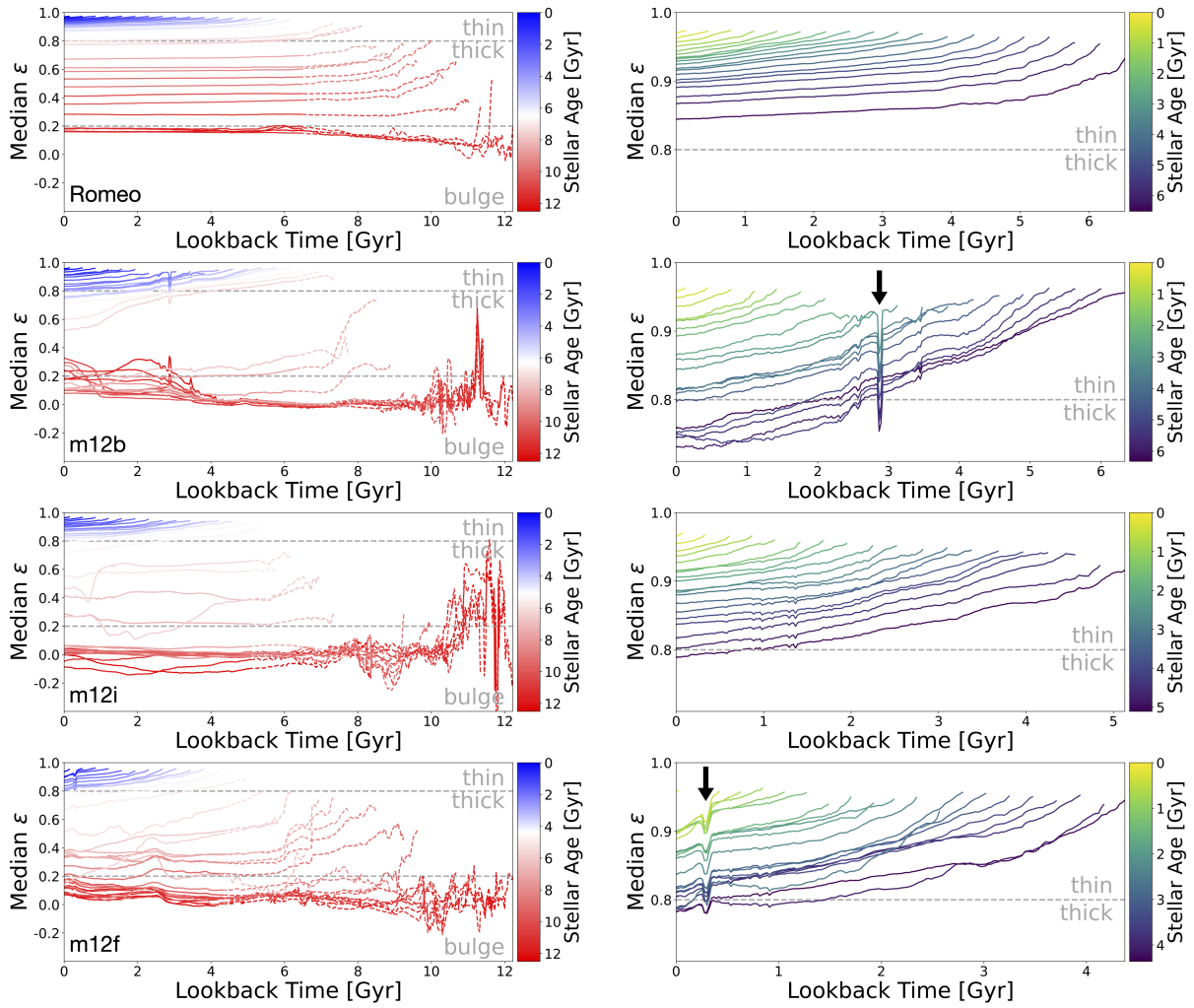

Figure 4.7: **Left:** Evolution of the population-median circularity $\epsilon = j_z/j_c(E)$ of all mono-age stellar populations for `Romeo`, `m12b`, `m12i`, and `m12f`. Each curve is coloured by stellar age of the population. The colorbars are set so that all the populations form during the bursty phase are colored red while the populations form during the steady phase are colored blue. Older populations (red lines) tend to settle down to more bulge-like orbits while younger populations (blue lines) form with much higher circularities. **Right:** Zoomed-in plots for only the populations form during the steady phase for each host galaxy. All the curves lie above the 0.8 thin-disc threshold, suggesting most stars form during this period show thin-disc like orbital properties. Note that, for `Romeo` and `m12i`, all populations form during the steady phase experience a drop in j_z/j_c but later plateau at a nearly constant value. For both `m12b` and `m12f` that have undergone recent merger events during the steady phase, there is an obvious dip during the time of merger, indicated by the arrows in the right panels.

the classification of three components. We observe this general trend in all four galaxies that most populations form during bursty phase (red lines) lie below our threshold of stellar bulge while populations born during steady phase (blue lines) are above the thin-disc threshold. We observe larger fluctuations for old populations at early times but later they all plateau at a nearly constant value around $\epsilon \sim 0$, making up the bulge component we see today.

We show a more zoomed-in version in the right panels of Figure 4.7, where we only select populations that form during the steady phase. The lines are coloured by the stellar age. Stars form during this period with extremely high circularity ($\epsilon \sim 1$). Then they slowly drops down but most of the stars still have fairly high circularity ($\epsilon \gtrsim 0.8$) at $z = 0$. We further explore the change in the circularity in Figure 4.10, where we try quantifying the change for populations form at different times.

Similar to Figure 4.7, Figure 4.8 shows the evolution of 3D circularity ϵ_{3D} and Figure 4.9 shows for alignment angle θ. These two figures complements Figure 4.7 in a way that breaks down the contribution to the change in circularity ϵ further into two aspects: dynamical heating and vertical torquing. 3D circularity ϵ_{3D} quantifies how circular the orbits are and the alignment angle θ quantifies the level of alignment of angular momentum in the stars with respect to the rotation axis of the galaxy disc. For stellar populations born during the bursty phase, their orbits are more radial-like with smaller ϵ_{3D} and the distribution of the alignment angle centered around 90°, indicating that their orbits are more isotropically distributed.

In the zoom-in panels for both 3D circularity ϵ_{3D} and alignment angle θ, we see that the value drops after birth, indicating that the change in orbital circularity ϵ is a result of both the introduction of non-circular motion from dynamical heating and the change of orientation of the orbits from vertical torquing. A more detailed analysis of possible mechanisms for the heating/torquing is deferred for future work.

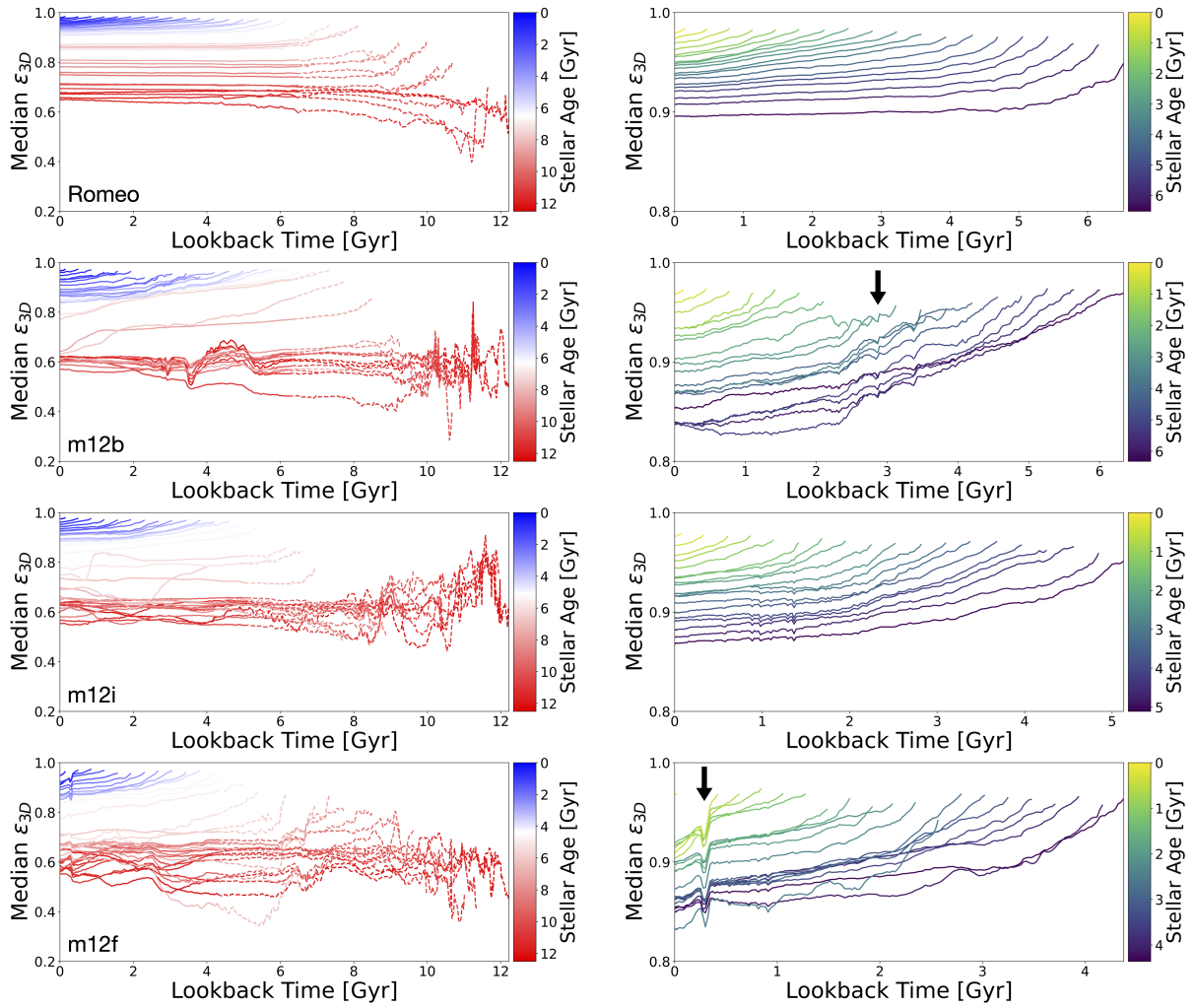

Figure 4.8: **Left:** Evolution of the population-median circularity $\epsilon_{3D} = j/j_c(E)$ of all mono-age stellar populations for `Romeo`, `m12b`, `m12i`, and `m12f`. Each curve is coloured by stellar age of the population. The colorbars are set so that all the populations form during the bursty phase are colored red while the populations form during the steady phase are colored blue. Younger populations (blue lines) tend to form in very circular orbits while older populations (red lines) are born in more radial orbits and stay in similar configuration. **Right:** Zoomed-in plots for only the populations form during the steady phase for each host galaxy. Most stars form during this period have very circular orbits and stay circular afterwards. Note that, all populations form during the steady phase do experience a drop in ϵ_{3D} but later plateau at a nearly constant value. Similar to before, the arrows in `m12b` and `m12f` indicate mergers.

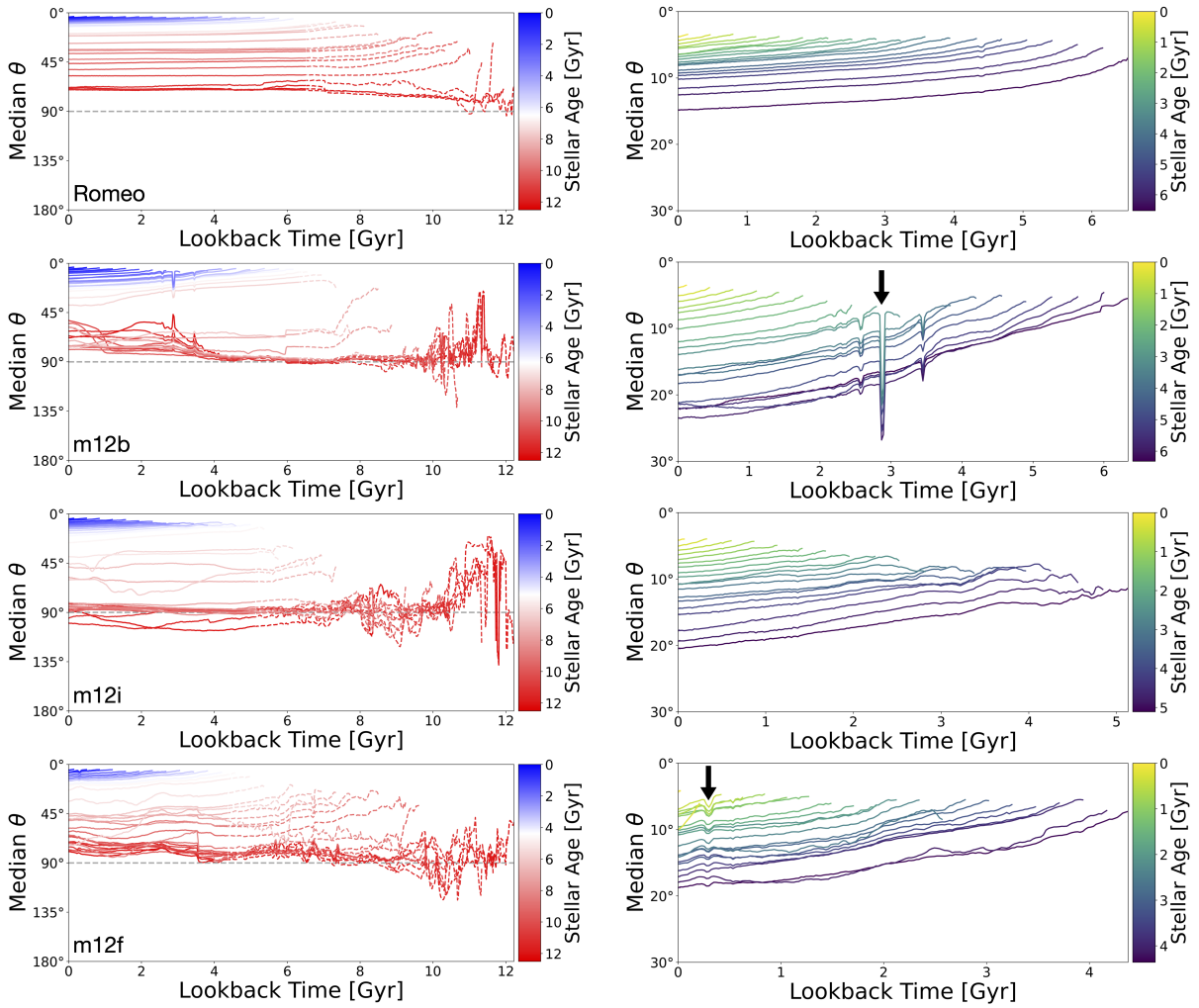

Figure 4.9: **Left:** Evolution of the population-median alignment angle $\theta = j_z/j$ of all mono-age stellar populations for `Romeo`, `m12b`, `m12i`, and `m12f`. Each curve is coloured by stellar age of the population. The colorbars are set so that all the populations form during the bursty phase are colored red while the populations form during the steady phase are colored blue. Orbits of older populations (red lines) tend to be in random directions with respect to the orientation of the galaxy while younger populations (blue lines) form more aligned with the disc. **Right:** Zoomed-in plots for only the populations form during the steady phase for each host galaxy. All populations form fairly aligned with the disc ($\theta \lesssim 10°$). They do experience a drop in θ but later plateau at a nearly constant value. Similar to before, the arrows in `m12b` and `m12f` indicate mergers.

Figure 4.10 explores the average change in these orbital properties of all mono-age stellar populations. The left panels show the average change in circularity ϵ per Gyr (calculated by dividing $\epsilon_{\rm now} - \epsilon_{\rm birth}$ by the stellar age). Red dots represent the populations form during bursty phase and blue dots show the ones born in steady phase. We estimate the amount of "thickening" needed for different populations that are born perfectly thin ($\epsilon = 1.0$) to become thick ($\epsilon \lesssim 0.8$) and draw the grey bands in the panels. However when interpreting this result, we need to remember that this estimation only makes sense when compared with stars born in steady phase since stars born during bursty phase are born with more thick-disc or even bulge-like orbits. Thus, the basic assumption of this estimation does not hold for these populations. And for most populations born in steady phase, the average "thickening" effect is simply not enough to turn stars born in thin disc into thick-disc like orbits (most blue dots lie below the grey bands). And we further explore the change in 3D circularity $\epsilon_{\rm 3D}$ and alignment angle θ to disentangle the effect from dynamical heating and vertical torquing. As we can see both mechanisms work to thicken the newly-born stars but the amount of heating and torquing is pretty minimal. The change in $\epsilon_{\rm 3D}$ is smaller than 0.05 per Gyr and the change in θ is smaller than 5° per Gyr. We do note that the average change is a little higher for the really young populations as we see the upticks around stellar age $\sim$ 0 Gyr. This is probably because all the heating/torquing happens at the very beginning right after they form, which we further explore in details in Figure A.8 and Figure A.9 in §A.5.

The overall trend here is that stars that are born on elliptical orbits are still living in a bulge today and stars that are born as a thin disk are mostly today still in a thin disk. Broadly speaking, stars in different component are simply "born that way". There is dynamical heating and torquing but they are not necessary things to have to form the thick disc or bulge. The thick disc and bulge formed in-situ at high redshift. These two components were already in place before the thin disc even started forming. And the amount of heating and torquing is simply not enough to completely change the kinematic status of the majority of the stars.

In §3.3.2, we have briefly explored the importance of mergers in shaping thin/thick disc formation in the simulations. In this analysis, we also include the two galaxies, `m12b`, and `m12f`, that have undergone recent merger events after star formation settles down. In Figure 4.7, Figure 4.8, and Figure 4.9, we mark the merger events with black arrows in the zoom-in panels. When a merger happens, we can see that there is a dip in all three parameters. This could be due to the way we calculate these parameters. When the merger happens, the satellite galaxy gets close to the host galaxy. And when we calculate the $\hat{z}$ direction (also the rotation axis) of the galaxy, since we simply include all the stars within $0.1R_{\rm vir}$ of each galaxy's center at the time of the snapshot, we inevitably also include the stars of the satellite galaxy in the calculation. Thus, it would change the $\hat{z}$ direction at that snapshot. And after the merger, it would go back to normal if the host galaxy is not disrupted. Another influence posted by the merger is the temporary change of the potential profile. It is not that the real potential of the galaxy changes. But when we calculate the potential energy of a particle, we simply sum up the total mass within certain radius. Thus, similarly, the existence of the satellite galaxy would change the potential energy by a comparably large amount compared to the natural mass growth. And after the interaction, the value would go back to normal. Therefore it would result in the dips we see in all three figures.

Although we cannot draw a conclusion here about whether mergers would drastically change the kinematics of newly-formed stars because of the caveats in our calculation. It not very likely that they would do so based on the fact that these parameters only get disturbed very shortly and then go back to steady afterwards. These mergers do not destroy or disrupt the disc. Again, this is consistent with our result in §3.3.2. These mergers are not responsible for the bulk of thick-disc or bulge stars. They may heat up some thin disc stars but even if they do so, it is not significant and only plays a secondary role in the formation of thick-disc and central bulge populations.

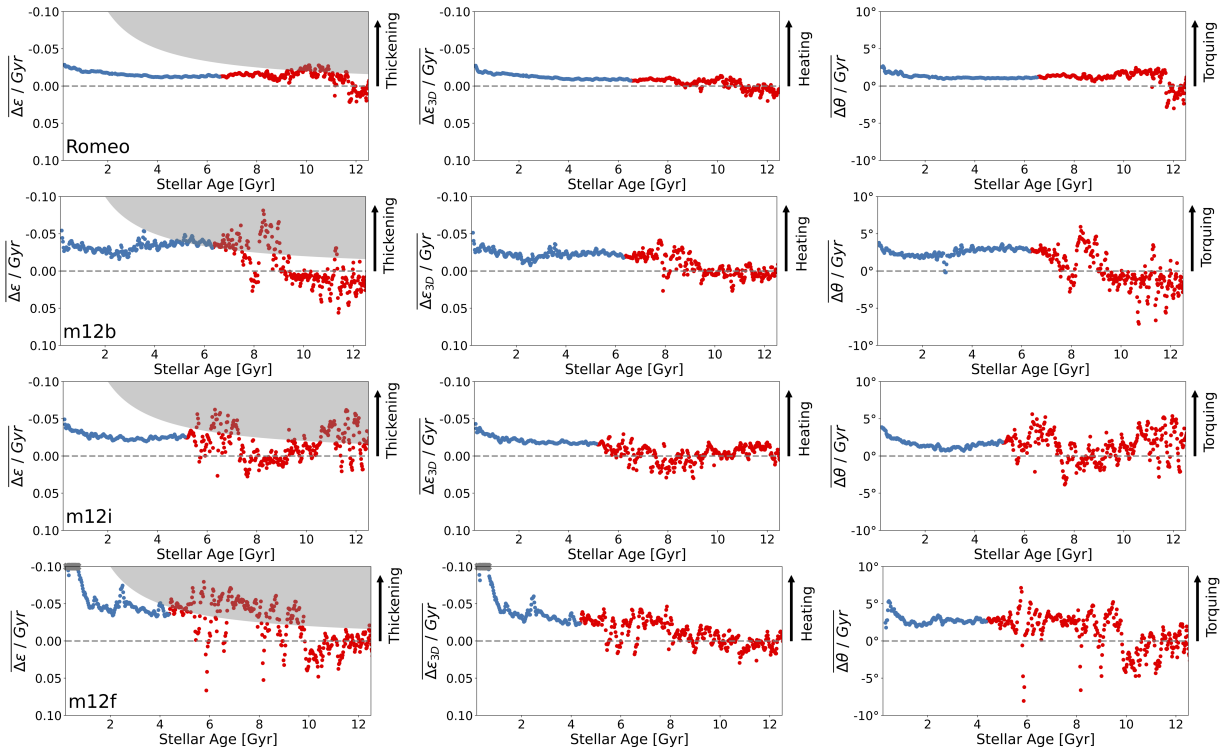

Figure 4.10: Average change in circularity ϵ per Gyr (left), 3D circularity ϵ_{3D} per Gyr (middle), and alignment angle θ per Gyr (right) of all mono-age stellar populations for `Romeo`, `m12b`, `m12i`, and `m12f`. It explores the average thickening effect for different stellar populations born at different times. The red dots represent populations born during bursty phase (stellar age¿$t_{\rm b}$) while blue dots show stars born after the star formation settles down. The grey bands in the left panel estimate the amount of "thickening" needed for stars born thin ($\epsilon_{\rm birth} = 1.0$) to become thick ($\epsilon_{\rm now} \leq 0.8$). Note that, this estimation only makes sense when compared with the population born in steady phase since stars born in bursty phase are already thick-disc/bulge like when they form. Middle panels and right panels show the kinematic heating and vertical torquing respectively. The changes in both quantities are minimal.

4.3.3 Sample-wide trend

In this section, we briefly explore the trend of the formation of different components among all of the simulated galaxies we have now.

Figure 4.11 illustrates kernel density estimate of stellar age distribution of different components when classified by circularity ϵ at $z = 0$ for all 12 galaxies. Curves are coloured by the bursty-phase lookback time $t_{\rm b}$. We smooth all lines with a Gaussian filter (using kalepy.density [131] with bandwidth = 0.2). The top, middle and bottom panel are showing thin-disc stars, thick-disc stars and bulge stars respectively. We plot quantities as a function of stellar age - $t_{\rm b}$ instead of stellar age, in order to highlight the correspondence between the transition from bursty to steady star formation and the formation of different components in the galaxy.

When offset by $t_{\rm b}$, the 12 different galaxies show remarkable overlap in the relative age distribution, especially for the bulge population. Almost all the bulge stars formed during the bursty phase (stellar age - $t_{\rm b} > 0$), while thin-disc stars dominate after star formation has settled down (stellar age - $t_{\rm b} < 0$). One galaxy in our sample, `m12w`, never really settles down ($t_{\rm b} = 0.0$ Gyr), and thus its thin disc also formed during the bursty phase. Its morphology also shows that its disc is thicker than all the other runs with a smaller thin-disc fraction as well [236].

Again, this agrees with our broad picture. The Milky-Way-mass galaxies start off first building the bulge structure and then forming the thick disc. Only later over time, the disc gets thinner and thinner and really dominates the structure formation.

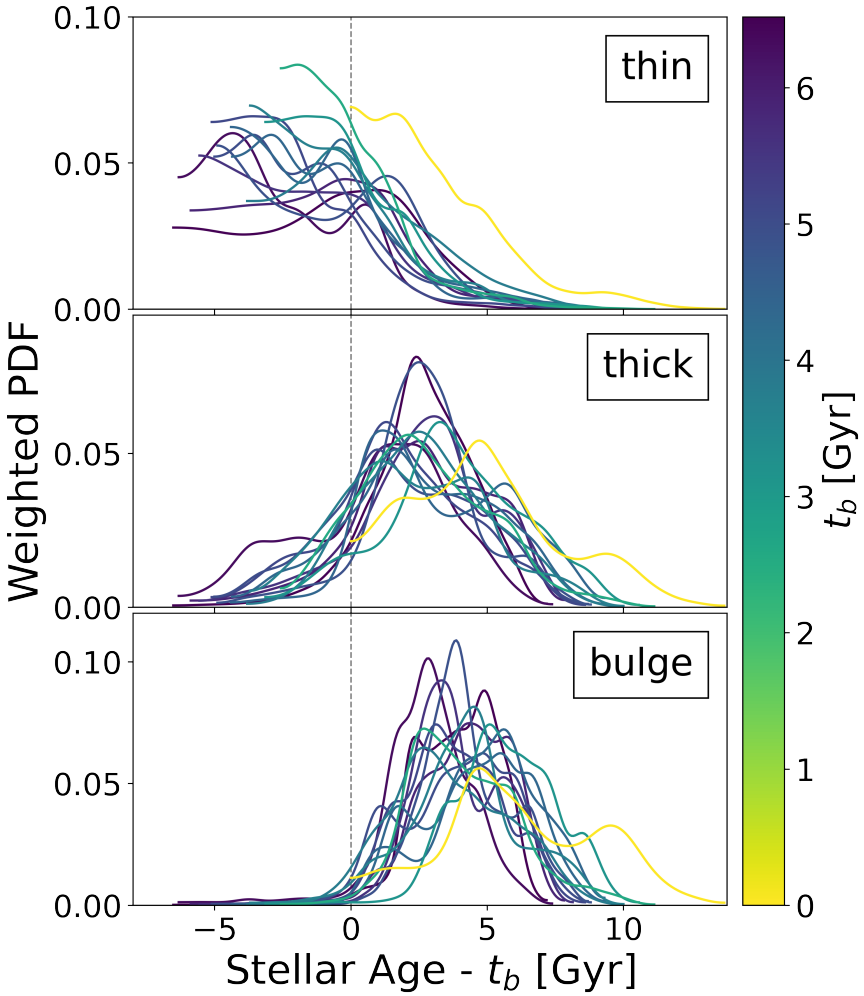

Figure 4.11: Kernel density estimate of ages of $z = 0$ stars that belong to different components in all 12 sample galaxies. The top, middle and bottom panel are showing thin disc stars, thick disc stars and bulge stars respectively. Different lines correspond to different host galaxies and are color coded by the bursty-phase lookback time $t_{\rm b}$. When offset by $t_{\rm b}$, the 12 different simulations show some overlap in the relative age distributions, especially for the bulge populations, whose formation almost completely shut down after $t_{\rm b}$ (stellar age - $t_{\rm b} < 0$).

4.4 Discussion and Conclusions

We dive deep into the evolution of the Milky-way-mass galaxies using five FIRE-2 zoom-in simulations. Our main findings include the following:

- Each galaxy experiences three different stages in the evolution: 1) a very early, chaotic bursty phase; 2) a later quasi-stable "bursty-disc" phase; and 3) a stable thin-disc phase.
- At high redshift, galaxies tend to exhibit clumpy, irregular morphologies and have bursty star formation with large temporal fluctuations about mean star formation rate while the inner CGM has not virialized yet. Stars are initially born in more radial orbits and form the central bulge component we see in the galaxy today.
- At low redshift, stars tend to form on extremely circular orbits when SFR is steady and the inner CGM is virialized. Galaxies are more rotationally-supported and exhibit morphologically thin discs.

All five simulations exhibit sufficient thin disk morphology embedded within a thick disc at $z = 0$. And our discs first emerge thick and become thinner over cosmic time. The central bulges in the galaxies appear to form first and consist of some of the oldest populations.

Two of our five simulations experience substantial late-time mergers during the steady phase. However, these mergers neither destroy the discs nor significantly alter the way how young stars form. This result is consistent with what we have discussed in §3.3.2. Mergers may heat the thin-disc stars and contribute to thick-disc populations but only play a secondary role in the formation of thick-disc and central bulge populations.

In addition to mergers, we also briefly explore the "thickening" effect. According to our analysis, most of the stars experience certain amount of heating/torquing right after they

form. But this turns out to be more of a temporary effect which eventually dies down and the kinematics of those stars become very stable. It is very unlikely that this kind of disc heating/torquing is capable of building up the whole thick-disc or bulge components.

We observe that the transition time of the inner CGM becoming virialised coincides with the transition time from bursty to steady star formation. And based on recent studies (e.g., [216, 103, 104]), we believe that these changes are tightly correlated. However, it is extremely difficult to disentangle the causal role of all of these different processes, as pointed out in Hopkins et al. *in prep.* They conduct a series of controlled studies designed to isolate different mechanisms and explore their effects on the disc formation. Their results suggest that one key condition for disk to form is to have a sufficiently centrally-concentrated potential profile, while the smooth star formation is more likely to be the result of the potential or escape velocity scale crossing a critical threshold. However, there is still no complete cosmological explanation for the whole set of transitions. This is important for not only understanding the galaxies, but also for constraining the physics models used in simulations. Future work in this direction will be exciting and inspiring.

Bibliography

[1] S. Aalto, S. Garcia-Burillo, S. Muller, J. M. Winters, E. Gonzalez-Alfonso, P. van der Werf, C. Henkel, F. Costagliola, and R. Neri. High resolution observations of HCN and HCO^+J = 3-2 in the disk and outflow of Mrk 231. Detection of vibrationally excited HCN in the warped nucleus. , 574:A85, Feb. 2015.

[2] M. G. Abadi, J. F. Navarro, M. Steinmetz, and V. R. Eke. Simulations of Galaxy Formation in a Λ Cold Dark Matter Universe. II. The Fine Structure of Simulated Galactic Disks. , 597(1):21–34, Nov. 2003.

[3] R. G. Abraham, S. van den Bergh, and P. Nair. A New Approach to Galaxy Morphology. I. Analysis of the Sloan Digital Sky Survey Early Data Release. , 588(1):218–229, May 2003.

[4] C. Allende Prieto, T. C. Beers, R. Wilhelm, H. J. Newberg, C. M. Rockosi, B. Yanny, and Y. S. Lee. A Spectroscopic Study of the Ancient Milky Way: F- and G-Type Stars in the Third Data Release of the Sloan Digital Sky Survey. , 636(2):804–820, Jan 2006.

[5] A. Alves-Brito, J. Meléndez, M. Asplund, I. Ramírez, and D. Yong. Chemical similarities between Galactic bulge and local thick disk red giants: O, Na, Mg, Al, Si, Ca, and Ti. , 513:A35, Apr. 2010.

[6] J. A. S. Amarante, L. Beraldo e Silva, V. P. Debattista, and M. C. Smith. The Splash without a Merger. , 891(2):L30, Mar. 2020.

[7] N. C. Amorisco. Contributions to the accreted stellar halo: an atlas of stellar deposition. , 464(3):2882–2895, Jan. 2017.

[8] D. Anglés-Alcázar, C.-A. Faucher-Giguère, D. Kereš, P. F. Hopkins, E. Quataert, and N. Murray. The cosmic baryon cycle and galaxy mass assembly in the FIRE simulations. , 470(4):4698–4719, Oct. 2017.

[9] D. Anglés-Alcázar, C.-A. Faucher-Giguère, E. Quataert, P. F. Hopkins, R. Feldmann, P. Torrey, A. Wetzel, and D. Kereš. Black holes on FIRE: stellar feedback limits early feeding of galactic nuclei. , 472(1):L109–L114, Nov. 2017.

[10] E. Applebaum, A. M. Brooks, C. R. Christensen, F. Munshi, T. R. Quinn, S. Shen, and M. Tremmel. Ultrafaint Dwarfs in a Milky Way Context: Introducing the Mint Condition DC Justice League Simulations. , 906(2):96, Jan. 2021.

[11] Astropy Collaboration, A. M. Price-Whelan, B. M. Sipőcz, H. M. Günther, P. L. Lim, S. M. Crawford, S. Conseil, D. L. Shupe, M. W. Craig, N. Dencheva, A. Ginsburg, J. T. VanderPlas, L. D. Bradley, D. Pérez-Suárez, M. de Val-Borro, T. L. Aldcroft, K. L. Cruz, T. P. Robitaille, E. J. Tollerud, C. Ardelean, T. Babej, Y. P. Bach, M. Bachetti, A. V. Bakanov, S. P. Bamford, G. Barentsen, P. Barmby, A. Baumbach, K. L. Berry, F. Biscani, M. Boquien, K. A. Bostroem, L. G. Bouma, G. B. Brammer, E. M. Bray, H. Breytenbach, H. Buddelmeijer, D. J. Burke, G. Calderone, J. L. Cano Rodríguez, M. Cara, J. V. M. Cardoso, S. Cheedella, Y. Copin, L. Corrales, D. Crichton, D. D'Avella, C. Deil, É. Depagne, J. P. Dietrich, A. Donath, M. Droettboom, N. Earl, T. Erben, S. Fabbro, L. A. Ferreira, T. Finethy, R. T. Fox, L. H. Garrison, S. L. J. Gibbons, D. A. Goldstein, R. Gommers, J. P. Greco, P. Greenfield, A. M. Groener, F. Grollier, A. Hagen, P. Hirst, D. Homeier, A. J. Horton, G. Hosseinzadeh, L. Hu, J. S. Hunkeler, Ž. Ivezić, A. Jain, T. Jenness, G. Kanarek, S. Kendrew, N. S. Kern, W. E. Kerzendorf, A. Khvalko, J. King, D. Kirkby, A. M. Kulkarni, A. Kumar, A. Lee, D. Lenz, S. P. Littlefair, Z. Ma, D. M. Macleod, M. Mastropietro, C. McCully, S. Montagnac, B. M. Morris, M. Mueller, S. J. Mumford, D. Muna, N. A. Murphy, S. Nelson, G. H. Nguyen, J. P. Ninan, M. Nöthe, S. Ogaz, S. Oh, J. K. Parejko, N. Parley, S. Pascual, R. Patil, A. A. Patil, A. L. Plunkett, J. X. Prochaska, T. Rastogi, V. Reddy Janga, J. Sabater, P. Sakurikar, M. Seifert, L. E. Sherbert, H. Sherwood-Taylor, A. Y. Shih, J. Sick, M. T. Silbiger, S. Singanamalla, L. P. Singer, P. H. Sladen, K. A. Sooley, S. Sornarajah, O. Streicher, P. Teuben, S. W. Thomas, G. R. Tremblay, J. E. H. Turner, V. Terrón, M. H. van Kerkwijk, A. de la Vega, L. L. Watkins, B. A. Weaver, J. B. Whitmore, J. Woillez, V. Zabalza, and Astropy Contributors. The Astropy Project: Building an Open-science Project and Status of the v2.0 Core Package. , 156(3):123, Sept. 2018.

[12] Astropy Collaboration, T. P. Robitaille, E. J. Tollerud, P. Greenfield, M. Droettboom, E. Bray, T. Aldcroft, M. Davis, A. Ginsburg, A. M. Price-Whelan, W. E. Kerzendorf, A. Conley, N. Crighton, K. Barbary, D. Muna, H. Ferguson, F. Grollier, M. M. Parikh, P. H. Nair, H. M. Unther, C. Deil, J. Woillez, S. Conseil, R. Kramer, J. E. H. Turner, L. Singer, R. Fox, B. A. Weaver, V. Zabalza, Z. I. Edwards, K. Azalee Bostroem, D. J. Burke, A. R. Casey, S. M. Crawford, N. Dencheva, J. Ely, T. Jenness, K. Labrie, P. L. Lim, F. Pierfederici, A. Pontzen, A. Ptak, B. Refsdal, M. Servillat, and O. Streicher. Astropy: A community Python package for astronomy. , 558:A33, Oct. 2013.

[13] E. Athanassoula. On the nature of bulges in general and of box/peanut bulges in particular: input from N-body simulations. , 358(4):1477–1488, Apr. 2005.

[14] W. Baade. A Search For the Nucleus of Our Galaxy. , 58(343):249–252, Aug. 1946.

[15] B. Barbuy, C. Chiappini, and O. Gerhard. Chemodynamical History of the Galactic Bulge. , 56:223–276, Sept. 2018.

[16] E. F. Bell, D. H. McIntosh, N. Katz, and M. D. Weinberg. The Optical and Near-Infrared Properties of Galaxies. I. Luminosity and Stellar Mass Functions. , 149(2):289–312, Dec. 2003.

[17] E. F. Bell, A. Monachesi, B. Harmsen, R. S. de Jong, J. Bailin, D. J. Radburn-Smith, R. D'Souza, and B. W. Holwerda. Galaxies Grow Their Bulges and Black Holes in Diverse Ways. , 837(1):L8, Mar. 2017.

[18] E. F. Bell, D. B. Zucker, V. Belokurov, S. Sharma, K. V. Johnston, J. S. Bullock, D. W. Hogg, K. Jahnke, J. T. A. de Jong, T. C. Beers, N. W. Evans, E. K. Grebel, Ž. Ivezić, S. E. Koposov, H.-W. Rix, D. P. Schneider, M. Steinmetz, and A. Zolotov. The Accretion Origin of the Milky Way's Stellar Halo. , 680:295–311, June 2008.

[19] M. A. Bellardini, A. Wetzel, S. R. Loebman, C.-A. Faucher-Giguère, X. Ma, and R. Feldmann. 3D gas-phase elemental abundances across the formation histories of Milky Way-mass galaxies in the FIRE simulations: initial conditions for chemical tagging. , 505(3):4586–4607, Aug. 2021.

[20] V. Belokurov, D. Erkal, N. W. Evans, S. E. Koposov, and A. J. Deason. Co-formation of the disc and the stellar halo. , 478(1):611–619, July 2018.

[21] V. Belokurov, S. E. Koposov, N. W. Evans, J. Peñarrubia, M. J. Irwin, M. C. Smith, G. F. Lewis, M. Gieles, M. I. Wilkinson, G. Gilmore, E. W. Olszewski, and M. Niederste-Ostholt. Precession of the Sagittarius stream. , 437(1):116–131, Jan. 2014.

[22] V. Belokurov and A. Kravtsov. From dawn till disk: Milky Way's turbulent youth revealed by the APOGEE+Gaia data. , May 2022.

[23] V. Belokurov, J. L. Sanders, A. Fattahi, M. C. Smith, A. J. Deason, N. W. Evans, and R. J. J. Grand. The biggest splash. , 494(3):3880–3898, May 2020.

[24] V. Belokurov, D. B. Zucker, N. W. Evans, G. Gilmore, S. Vidrih, D. M. Bramich, H. J. Newberg, R. F. G. Wyse, M. J. Irwin, M. Fellhauer, P. C. Hewett, N. A. Walton, M. I. Wilkinson, N. Cole, B. Yanny, C. M. Rockosi, T. C. Beers, E. F. Bell, J. Brinkmann, Ž. Ivezić, and R. Lupton. The Field of Streams: Sagittarius and Its Siblings. , 642(2):L137–L140, May 2006.

[25] A. Benítez-Llambay, C. S. Frenk, A. D. Ludlow, and J. F. Navarro. Baryon-induced dark matter cores in the EAGLE simulations. , 488(2):2387–2404, Sept. 2019.

[26] T. Bensby, A. Alves-Brito, M. S. Oey, D. Yong, and J. Meléndez. A First Constraint on the Thick Disk Scale Length: Differential Radial Abundances in K Giants at Galactocentric Radii 4, 8, and 12 kpc. , 735(2):L46, July 2011.

[27] T. Bensby, S. Feltzing, I. Lundström, and I. Ilyin. α-, r-, and s-process element trends in the Galactic thin and thick disks. , 433(1):185–203, Apr. 2005.

[28] J. C. Bird, S. Kazantzidis, D. H. Weinberg, J. Guedes, S. Callegari, L. Mayer, and P. Madau. Inside out and Upside down: Tracing the Assembly of a Simulated Disk Galaxy Using Mono-age Stellar Populations. , 773(1):43, Aug. 2013.

[29] J. C. Bird, S. R. Loebman, D. H. Weinberg, A. M. Brooks, T. R. Quinn, and C. R. Christensen. Inside out and upside-down: The roles of gas cooling and dynamical heating in shaping the stellar age-velocity relation. , 503(2):1815–1827, May 2021.

[30] A. Bonaca, C. Conroy, P. A. Cargile, R. P. Naidu, B. D. Johnson, D. Zaritsky, Y.-S. Ting, N. Caldwell, J. J. Han, and P. van Dokkum. Timing the Early Assembly of the Milky Way with the H3 Survey. , 897(1):L18, July 2020.

[31] A. Bonaca, C. Conroy, A. Wetzel, P. F. Hopkins, and D. Kereš. Gaia Reveals a Metal-rich, in situ Component of the Local Stellar Halo. , 845(2):101, Aug 2017.

[32] J. Bovy and H.-W. Rix. A Direct Dynamical Measurement of the Milky Way's Disk Surface Density Profile, Disk Scale Length, and Dark Matter Profile at 4 kpc <~R <~9 kpc. , 779(2):115, Dec. 2013.

[33] J. Bovy, H.-W. Rix, and D. W. Hogg. The Milky Way Has No Distinct Thick Disk. , 751(2):131, June 2012.

[34] C. B. Brook, D. Kawata, B. K. Gibson, and K. C. Freeman. The Emergence of the Thick Disk in a Cold Dark Matter Universe. , 612(2):894–899, Sept. 2004.

[35] C. B. Brook, D. Kawata, H. Martel, B. K. Gibson, and J. Bailin. Disk Evolution since z~1 in a CDM Universe. , 639(1):126–135, Mar. 2006.

[36] C. B. Brook, G. S. Stinson, B. K. Gibson, D. Kawata, E. L. House, M. S. Miranda, A. V. Macciò, K. Pilkington, R. Roškar, J. Wadsley, and T. R. Quinn. Thin disc, thick disc and halo in a simulated galaxy. , 426(1):690–700, Oct. 2012.

[37] T. M. Brown, K. Sahu, J. Anderson, J. Tumlinson, J. A. Valenti, E. Smith, E. J. Jeffery, A. Renzini, M. Zoccali, H. C. Ferguson, D. A. VandenBerg, H. E. Bond, S. Casertano, E. Valenti, D. Minniti, M. Livio, and N. Panagia. The WFC3 Galactic Bulge Treasury Program: Metallicity Estimates for the Stellar Population and Exoplanet Hosts. , 725(1):L19–L23, Dec. 2010.

[38] W. R. Brown, M. J. Geller, S. J. Kenyon, and M. J. Kurtz. Discovery of an Unbound Hypervelocity Star in the Milky Way Halo. , 622:L33–L36, Mar. 2005.

[39] M. Brüggen and E. Scannapieco. The Launching of Cold Clouds by Galaxy Outflows. II. The Role of Thermal Conduction. , 822(1):31, May 2016.

[40] J. S. Bullock and K. V. Johnston. Tracing Galaxy Formation with Stellar Halos. I. Methods. , 635:931–949, Dec. 2005.

[41] J. S. Bullock, A. V. Kravtsov, and D. H. Weinberg. Hierarchical Galaxy Formation and Substructure in the Galaxy's Stellar Halo. , 548:33–46, Feb. 2001.

[42] D. Burstein. Structure and origin of S0 galaxies. III. The luminosity distribution perpendicular to the plane of the disks in S0's. , 234:829–836, Dec. 1979.

[43] A. Camps-Fariña, J. Zaragoza-Cardiel, J. E. Beckman, J. Font, P. F. Velázquez, A. Rodríguez-González, and M. Rosado. Physical properties of superbubbles in the Antennae galaxies. , 468(4):4134–4142, Jul 2017.

[44] D. Ceverino, A. Dekel, D. Tweed, and J. Primack. Early formation of massive, compact, spheroidal galaxies with classical profiles by violent disc instability or mergers. , 447(4):3291–3310, Mar. 2015.

[45] W. Clarkson, K. Sahu, J. Anderson, T. E. Smith, T. M. Brown, R. M. Rich, S. Casertano, H. E. Bond, M. Livio, D. Minniti, N. Panagia, A. Renzini, J. Valenti, and M. Zoccali. Stellar Proper Motions in the Galactic Bulge from Deep Hubble Space Telescope ACS WFC Photometry. , 684(2):1110–1142, Sept. 2008.

[46] F. Combes and R. H. Sanders. Formation and properties of persisting stellar bars. , 96:164–173, Mar. 1981.

[47] S. Comerón, B. G. Elmegreen, J. H. Knapen, H. Salo, E. Laurikainen, J. Laine, E. Athanassoula, A. Bosma, K. Sheth, M. W. Regan, J. L. Hinz, A. Gil de Paz, K. Menéndez-Delmestre, T. Mizusawa, J.-C. Muñoz-Mateos, M. Seibert, T. Kim, D. M. Elmegreen, D. A. Gadotti, L. C. Ho, B. W. Holwerda, J. Lappalainen, E. Schinnerer, and R. Skibba. Thick Disks of Edge-on Galaxies Seen through the Spitzer Survey of Stellar Structure in Galaxies (S^4G): Lair of Missing Baryons? , 741(1):28, Nov. 2011.

[48] C. Conroy, A. Bonaca, P. Cargile, B. D. Johnson, N. Caldwell, R. P. Naidu, D. Zaritsky, D. Fabricant, S. Moran, J. Rhee, A. Szentgyorgyi, P. Berlind, M. L. Calkins, S. Kattner, and C. Ly. Mapping the Stellar Halo with the H3 Spectroscopic Survey. , 883(1):107, Sep 2019.

[49] C. Conroy, D. H. Weinberg, R. P. Naidu, T. Buck, J. W. Johnson, P. Cargile, A. Bonaca, N. Caldwell, V. Chandra, J. J. Han, B. D. Johnson, J. S. Speagle, Y.-S. Ting, T. Woody, and D. Zaritsky. Birth of the Galactic Disk Revealed by the H3 Survey. *arXiv e-prints*, page arXiv:2204.02989, Apr. 2022.

[50] A. P. Cooper, S. Cole, C. S. Frenk, S. D. M. White, J. Helly, A. J. Benson, G. De Lucia, A. Helmi, A. Jenkins, J. F. Navarro, V. Springel, and J. Wang. Galactic stellar haloes in the CDM model. , 406:744–766, Aug. 2010.

[51] S. Courteau, R. S. de Jong, and A. H. Broeils. Evidence for Secular Evolution in Late-Type Spirals. , 457:L73, Feb. 1996.

[52] E. C. Cunningham, A. J. Deason, C. M. Rockosi, P. Guhathakurta, Z. G. Jennings, E. N. Kirby, E. Toloba, and G. Barro. HALO7D I. The Line-of-sight Velocities of Distant Main-sequence Stars in the Milky Way Halo. , 876(2):124, May 2019.

[53] G. De Lucia. Milky Way simulations: The Galaxy, its stellar halo and its satellites - insights from a hybrid cosmological approach. *Astronomische Nachrichten*, 333(5-6):460, June 2012.

[54] G. De Lucia and A. Helmi. The Galaxy and its stellar halo: insights on their formation from a hybrid cosmological approach. , 391:14–31, Nov. 2008.

[55] G. de Vaucouleurs. Classification and Morphology of External Galaxies. *Handbuch der Physik*, 53:275, Jan. 1959.

[56] A. J. Deason, V. Belokurov, and J. L. Sanders. The total stellar halo mass of the Milky Way. , 490(3):3426–3439, Dec. 2019.

[57] A. Dekel, O. Ginzburg, F. Jiang, J. Freundlich, S. Lapiner, D. Ceverino, and J. Primack. A mass threshold for galactic gas discs by spin flips. , 493(3):4126–4142, Apr. 2020.

[58] T. Devergne, A. Cattaneo, F. Bournaud, I. Koutsouridou, A. Winter, P. Dimauro, G. A. Mamon, W. Vacher, and M. Varin. Bulge formation through disc instability. I. Stellar discs. , 644:A56, Dec. 2020.

[59] P. Di Matteo. The Disc Origin of the Milky Way Bulge. , 33:e027, June 2016.

[60] P. Di Matteo, F. Fragkoudi, S. Khoperskov, B. Ciambur, M. Haywood, F. Combes, and A. Gómez. Disk origin of the Milky Way bulge: the necessity of the thick disk. , 628:A11, Aug. 2019.

[61] P. Di Matteo, M. Haywood, A. Gómez, L. van Damme, F. Combes, A. Hallé, B. Semelin, M. D. Lehnert, and D. Katz. Mapping a stellar disk into a boxy bulge: The outside-in part of the Milky Way bulge formation. , 567:A122, July 2014.

[62] P. Di Matteo, M. Haywood, M. D. Lehnert, D. Katz, S. Khoperskov, O. N. Snaith, A. Gómez, and N. Robichon. The Milky Way has no in-situ halo other than the heated thick disc. Composition of the stellar halo and age-dating the last significant merger with Gaia DR2 and APOGEE. , 632:A4, Dec 2019.

[63] C. Du, H. Li, S. Liu, T. Donlon, and H. J. Newberg. The High-velocity Stars in the Local Stellar Halo from Gaia and LAMOST. , 863(1):87, Aug 2018.

[64] A. A. Dutton, A. V. Macciò, T. Buck, K. L. Dixon, M. Blank, and A. Obreja. NIHAO XX: the impact of the star formation threshold on the cusp-core transformation of cold dark matter haloes. , 486(1):655–671, June 2019.

[65] O. J. Eggen, D. Lynden-Bell, and A. R. Sandage. Evidence from the motions of old stars that the Galaxy collapsed. , 136:748, Nov. 1962.

[66] O. V. Egorov, T. A. Lozinskaya, A. V. Moiseev, and Y. A. Shchekinov. Complexes of triggered star formation in supergiant shell of Holmberg II. , 464(2):1833–1853, Jan 2017.

[67] O. V. Egorov, T. A. Lozinskaya, A. V. Moiseev, and G. V. Smirnov-Pinchukov. Star formation complexes in the 'galaxy-sized' supergiant shell of the galaxy HolmbergI. , 478(3):3386–3409, Aug 2018.

[68] K. El-Badry, J. Bland-Hawthorn, A. Wetzel, E. Quataert, D. R. Weisz, M. Boylan-Kolchin, P. F. Hopkins, C.-A. Faucher-Giguère, D. Kereš, and S. Garrison-Kimmel. Where are the most ancient stars in the Milky Way? , 480(1):652–668, Oct 2018.

[69] K. El-Badry, A. Wetzel, M. Geha, P. F. Hopkins, D. Kereš, T. K. Chan, and C.-A. Faucher-Giguère. Breathing FIRE: How Stellar Feedback Drives Radial Migration, Rapid Size Fluctuations, and Population Gradients in Low-mass Galaxies. , 820:131, Apr. 2016.

[70] B. G. Elmegreen and D. M. Elmegreen. Observations of Thick Disks in the Hubble Space Telescope Ultra Deep Field. , 650(2):644–660, Oct. 2006.

[71] B. G. Elmegreen, D. M. Elmegreen, B. Tompkins, and L. G. Jenks. Thick Disks in the Hubble Space Telescope Frontier Fields. , 847(1):14, Sept. 2017.

[72] D. M. Elmegreen, B. G. Elmegreen, S. Ravindranath, and D. A. Coe. Resolved Galaxies in the Hubble Ultra Deep Field: Star Formation in Disks at High Redshift. , 658(2):763–777, Apr. 2007.

[73] I. Escala, K. M. Gilbert, E. N. Kirby, J. Wojno, E. C. Cunningham, and P. Guhathakurta. Elemental Abundances in M31: A Comparative Analysis of Alpha and Iron Element Abundances in the the Outer Disk, Giant Stellar Stream, and Inner Halo of M31. , 889(2):177, Feb. 2020.

[74] I. Escala, E. N. Kirby, K. M. Gilbert, J. Wojno, E. C. Cunningham, and P. Guhathakurta. Elemental Abundances in M31: Properties of the Inner Stellar Halo. , 902(1):51, Oct. 2020.

[75] I. Escala, A. Wetzel, E. N. Kirby, P. F. Hopkins, X. Ma, C. Wheeler, D. Kereš, C.-A. Faucher-Giguère, and E. Quataert. Modelling chemical abundance distributions for dwarf galaxies in the Local Group: the impact of turbulent metal diffusion. , 474:2194–2211, Feb. 2018.

[76] A. Fattahi, V. Belokurov, A. J. Deason, C. S. Frenk, F. A. Gómez, R. J. J. Grand , F. Marinacci, R. Pakmor, and V. Springel. The origin of galactic metal-rich stellar halo components with highly eccentric orbits. , 484(4):4471–4483, Apr 2019.

[77] A. Fattahi, A. J. Deason, C. S. Frenk, C. M. Simpson, F. A. Gómez, R. J. J. Grand, A. Monachesi, F. Marinacci, and R. Pakmor. A tale of two populations: surviving and destroyed dwarf galaxies and the build-up of the Milky Way's stellar halo. , 497(4):4459–4471, Oct. 2020.

[78] C.-A. Faucher-Giguère. A model for the origin of bursty star formation in galaxies. , 473(3):3717–3731, Jan. 2018.

[79] C.-A. Faucher-Giguère, A. Lidz, M. Zaldarriaga, and L. Hernquist. A New Calculation of the Ionizing Background Spectrum and the Effects of He II Reionization. , 703(2):1416–1443, Oct. 2009.

[80] S. Feltzing and G. Gilmore. Age and metallicity gradients in the Galactic Bulge. A differential study using HST/WFPC2. , 355:949–965, Mar. 2000.

[81] A. Ferrara and E. Scannapieco. On the Formation of Molecular Clumps in QSO Outflows. , 833(1):46, Dec 2016.

[82] D. B. Fisher and N. Drory. An Observational Guide to Identifying Pseudobulges and Classical Bulges in Disc Galaxies. In E. Laurikainen, R. Peletier, and D. Gadotti, editors, *Galactic Bulges*, volume 418 of *Astrophysics and Space Science Library*, page 41, Jan. 2016.

[83] J. A. Flores Velázquez, A. B. Gurvich, C.-A. Faucher-Giguère, J. S. Bullock, T. K. Starkenburg, J. Moreno, A. Lazar, F. J. Mercado, J. Stern, M. Sparre, C. C. Hayward, A. Wetzel, and K. El-Badry. The time-scales probed by star formation rate indicators for realistic, bursty star formation histories from the FIRE simulations. , 501(4):4812–4824, Mar. 2021.

[84] A. S. Font, K. V. Johnston, A. M. N. Ferguson, J. S. Bullock, B. E. Robertson, J. Tumlinson, and P. Guhathakurta. The Stellar Content of Galaxy Halos: A Comparison between ΛCDM Models and Observations of M31. , 673(1):215–225, Jan 2008.

[85] K. C. Freeman. On the Disks of Spiral and S0 Galaxies. , 160:811, June 1970.

[86] J. K. C. Freudenburg, D. H. Weinberg, M. R. Hayden, and J. A. Holtzman. The Chemical Abundance Structure of the Inner Milky Way: A Signature of "Upside-down" Disk Formation. , 849(1):17, Nov. 2017.

[87] K. Fuhrmann. Nearby stars of the Galactic disk and halo. , 338:161–183, Oct. 1998.

[88] R. Gallagher, R. Maiolino, F. Belfiore, N. Drory, R. Riffel, and R. A. Riffel. Widespread star formation inside galactic outflows. , 485(3):3409–3429, May 2019.

[89] C. Gallart, E. J. Bernard, C. B. Brook, T. Ruiz-Lara, S. Cassisi, V. Hill, and M. Monelli. Uncovering the birth of the Milky Way through accurate stellar ages with Gaia. *Nature Astronomy*, 3:932–939, Jul 2019.

[90] H. Gao, L. C. Ho, A. J. Barth, and Z.-Y. Li. The Carnegie-Irvine Galaxy Survey. IX. Classification of Bulge Types and Statistical Properties of Pseudo Bulges. , 247(1):20, Mar. 2020.

[91] S. Garrison-Kimmel, M. Boylan-Kolchin, J. S. Bullock, and K. Lee. ELVIS: Exploring the Local Volume in Simulations. , 438(3):2578–2596, Mar. 2014.

[92] S. Garrison-Kimmel, P. F. Hopkins, A. Wetzel, J. S. Bullock, M. Boylan-Kolchin, D. Kereš, C.-A. Faucher-Giguère, K. El-Badry, A. Lamberts, E. Quataert, and R. Sand erson. The Local Group on FIRE: dwarf galaxy populations across a suite of hydrodynamic simulations. , 487(1):1380–1399, July 2019.

[93] S. Garrison-Kimmel, A. Wetzel, J. S. Bullock, P. F. Hopkins, M. Boylan-Kolchin, C.-A. Faucher-Giguère, D. Kereš, E. Quataert, R. E. Sanderson, A. S. Graus, and T. Kelley. Not so lumpy after all: modelling the depletion of dark matter subhaloes by Milky Way-like galaxies. , 471(2):1709–1727, Oct. 2017.

[94] S. Garrison-Kimmel, A. Wetzel, P. F. Hopkins, R. Sanderson, K. El-Badry, A. Graus, T. K. Chan, R. Feldmann, M. Boylan-Kolchin, C. C. Hayward, J. S. Bullock, A. Fitts, J. Samuel, C. Wheeler, D. Kereš, and C.-A. Faucher-Giguère. Star formation histories of dwarf galaxies in the FIRE simulations: dependence on mass and Local Group environment. , 489(4):4574–4588, Nov. 2019.

[95] R. Genzel, A. Burkert, N. Bouché, G. Cresci, N. M. Förster Schreiber, A. Shapley, K. Shapiro, L. J. Tacconi, P. Buschkamp, A. Cimatti, E. Daddi, R. Davies, F. Eisenhauer, D. K. Erb, S. Genel, O. Gerhard, E. Hicks, D. Lutz, T. Naab, T. Ott, S. Rabien, A. Renzini, C. C. Steidel, A. Sternberg, and S. J. Lilly. From Rings to Bulges: Evidence for Rapid Secular Galaxy Evolution at z ~2 from Integral Field Spectroscopy in the SINS Survey. , 687(1):59–77, Nov. 2008.

[96] G. Gilmore and N. Reid. New light on faint stars - III. Galactic structure towards the South Pole and the Galactic thick disc. , 202:1025–1047, Mar. 1983.

[97] O. A. Gonzalez and D. Gadotti. The Milky Way Bulge: Observed Properties and a Comparison to External Galaxies. In E. Laurikainen, R. Peletier, and D. Gadotti, editors, *Galactic Bulges*, volume 418 of *Astrophysics and Space Science Library*, page 199, Jan. 2016.

[98] R. J. J. Grand, S. Bustamante, F. A. Gómez, D. Kawata, F. Marinacci, R. Pakmor, H.-W. Rix, C. M. Simpson, M. Sparre, and V. Springel. Origin of chemically distinct discs in the Auriga cosmological simulations. , 474(3):3629–3639, Mar. 2018.

[99] R. J. J. Grand, D. Kawata, V. Belokurov, A. J. Deason, A. Fattahi, F. Fragkoudi, F. A. Gómez, F. Marinacci, and R. Pakmor. The dual origin of the Galactic thick disc and halo from the gas-rich Gaia-Enceladus Sausage merger. , 497(2):1603–1618, Sept. 2020.

[100] R. J. J. Grand, F. Marinacci, R. Pakmor, C. M. Simpson, A. J. Kelly, F. A. Gómez, A. Jenkins, V. Springel, C. S. Frenk, and S. D. M. White. Determining the full satellite population of a Milky Way-mass halo in a highly resolved cosmological hydrodynamic simulation. , 507(4):4953–4967, Nov. 2021.

[101] M. Y. Grudić, D. Guszejnov, P. F. Hopkins, A. Lamberts, M. Boylan-Kolchin, N. Murray, and D. Schmitz. From the top down and back up again: star cluster structure from hierarchical star formation. , 481(1):688–702, Nov 2018.

[102] Y. Guo, H. C. Ferguson, E. F. Bell, D. C. Koo, C. J. Conselice, M. Giavalisco, S. Kassin, Y. Lu, R. Lucas, N. Mandelker, D. H. McIntosh, J. R. Primack, S. Ravindranath, G. Barro, D. Ceverino, A. Dekel, S. M. Faber, J. J. Fang, A. M. Koekemoer, K. Noeske, M. Rafelski, and A. Straughn. Clumpy Galaxies in CANDELS. I. The Definition of

UV Clumps and the Fraction of Clumpy Galaxies at $0.5 < z < 3$. , 800(1):39, Feb. 2015.

[103] A. B. Gurvich, J. Stern, C.-A. Faucher-Giguère, P. F. Hopkins, A. Wetzel, J. Moreno, C. C. Hayward, A. J. Richings, and Z. Hafen. Rapid disc settling and the transition from bursty to steady star formation in Milky Way-mass galaxies. *arXiv e-prints*, page arXiv:2203.04321, Mar. 2022.

[104] Z. Hafen, J. Stern, J. Bullock, A. B. Gurvich, S. Yu, C.-A. Faucher-Giguere, D. B. Fielding, D. Angles-Alcazar, E. Quataert, A. Wetzel, T. Starkenburg, M. Boylan-Kolchin, J. Moreno, R. Feldmann, K. El-Badry, T. K. Chan, C. Trapp, D. Keres, and P. F. Hopkins. Hot-mode accretion and the physics of thin-disk galaxy formation. *arXiv e-prints*, page arXiv:2201.07235, Jan. 2022.

[105] C. R. Harris, K. J. Millman, S. J. van der Walt, R. Gommers, P. Virtanen, D. Cournapeau, E. Wieser, J. Taylor, S. Berg, N. J. Smith, R. Kern, M. Picus, S. Hoyer, M. H. van Kerkwijk, M. Brett, A. Haldane, J. F. del Río, M. Wiebe, P. Peterson, P. Gérard-Marchant, K. Sheppard, T. Reddy, W. Weckesser, H. Abbasi, C. Gohlke, and T. E. Oliphant. Array programming with NumPy. *Nature*, 585(7825):357–362, Sept. 2020.

[106] K. Hawkins and R. F. G. Wyse. The fastest travel together: chemical tagging of the fastest stars in Gaia DR2 to the stellar halo. , 481:1028–1040, Nov. 2018.

[107] M. R. Hayden, J. Bovy, J. A. Holtzman, D. L. Nidever, J. C. Bird, D. H. Weinberg, B. H. Andrews, S. R. Majewski, C. Allende Prieto, F. Anders, T. C. Beers, D. Bizyaev, C. Chiappini, K. Cunha, P. Frinchaboy, D. A. García-Herńand ez, A. E. García Pérez, L. Girardi, P. Harding, F. R. Hearty, J. A. Johnson, S. Mészáros, I. Minchev, R. O'Connell, K. Pan, A. C. Robin, R. P. Schiavon, D. P. Schneider, M. Schultheis, M. Shetrone, M. Skrutskie, M. Steinmetz, V. Smith, J. C. Wilson, O. Zamora, and G. Zasowski. Chemical Cartography with APOGEE: Metallicity Distribution Functions and the Chemical Structure of the Milky Way Disk. , 808(2):132, Aug. 2015.

[108] M. R. Hayden, A. Recio-Blanco, P. de Laverny, S. Mikolaitis, and C. C. Worley. The AMBRE project: The thick thin disk and thin thick disk of the Milky Way. , 608:L1, Nov. 2017.

[109] M. Haywood, P. Di Matteo, M. Lehnert, O. Snaith, F. Fragkoudi, and S. Khoperskov. Phylogeny of the Milky Way's inner disk and bulge populations: Implications for gas accretion, (the lack of) inside-out thick disk formation, and quenching. , 618:A78, Oct. 2018.

[110] M. Haywood, P. Di Matteo, M. D. Lehnert, D. Katz, and A. Gómez. The age structure of stellar populations in the solar vicinity. Clues of a two-phase formation history of the Milky Way disk. , 560:A109, Dec. 2013.

[111] M. Haywood, P. Di Matteo, M. D. Lehnert, O. Snaith, S. Khoperskov, and A. Gómez. In Disguise or Out of Reach: First Clues about In Situ and Accreted Stars in the Stellar Halo of the Milky Way from Gaia DR2. , 863(2):113, Aug. 2018.

[112] A. Helmi. The stellar halo of the Galaxy. , 15(3):145–188, June 2008.

[113] A. Helmi, C. Babusiaux, H. H. Koppelman, D. Massari, J. Veljanoski, and A. G. A. Brown. The merger that led to the formation of the Milky Way's inner stellar halo and thick disk. , 563(7729):85–88, Oct. 2018.

[114] J. A. Hodge, I. Smail, F. Walter, E. da Cunha, A. M. Swinbank, M. Rybak, B. Venemans, W. N. Brandt, G. Calistro Rivera, S. C. Chapman, C.-C. Chen, P. Cox, H. Dannerbauer, R. Decarli, T. R. Greve, K. K. Knudsen, K. M. Menten, E. Schinnerer, J. M. Simpson, P. van der Werf, J. L. Wardlow, and A. Weiss. ALMA Reveals Potential Evidence for Spiral Arms, Bars, and Rings in High-redshift Submillimeter Galaxies. , 876(2):130, May 2019.

[115] J. A. Holtzman, R. M. Light, W. A. Baum, G. Worthey, S. M. Faber, D. A. Hunter, J. O'Neil, Earl J., T. J. Kreidl, E. J. Groth, and J. A. Westphal. Wide Field Camera Observations of Baade's Window. , 106:1826, Nov. 1993.

[116] P. F. Hopkins. A new class of accurate, mesh-free hydrodynamic simulation methods. , 450:53–110, June 2015.

[117] P. F. Hopkins. A simple phenomenological model for grain clustering in turbulence. , 455(1):89–111, Jan. 2016.

[118] P. F. Hopkins. Anisotropic diffusion in mesh-free numerical magnetohydrodynamics. , 466:3387–3405, Apr. 2017.

[119] P. F. Hopkins, K. Bundy, D. Croton, L. Hernquist, D. Keres, S. Khochfar, K. Stewart, A. Wetzel, and J. D. Younger. Mergers and Bulge Formation in ΛCDM: Which Mergers Matter? , 715(1):202–229, May 2010.

[120] P. F. Hopkins, A. Wetzel, D. Kereš, C.-A. Faucher-Giguère, E. Quataert, M. Boylan-Kolchin, N. Murray, C. C. Hayward, S. Garrison-Kimmel, C. Hummels, R. Feldmann, P. Torrey, X. Ma, D. Anglés-Alcázar, K.-Y. Su, M. Orr, D. Schmitz, I. Escala, R. Sanderson, M. Y. Grudić, Z. Hafen, J.-H. Kim, A. Fitts, J. S. Bullock, C. Wheeler, T. K. Chan, O. D. Elbert, and D. Narayanan. FIRE-2 simulations: physics versus numerics in galaxy formation. , 480(1):800–863, Oct 2018.

[121] J. D. Hunter. Matplotlib: A 2d graphics environment. *Computing In Science & Engineering*, 9(3):90–95, 2007.

[122] R. A. Ibata, R. F. G. Wyse, G. Gilmore, M. J. Irwin, and N. B. Suntzeff. The Kinematics, Orbit, and Survival of the Sagittarius Dwarf Spheroidal Galaxy. , 113:634–655, Feb. 1997.

[123] K. V. Johnston. Origins of Stellar Halos. In A. Bragaglia, M. Arnaboldi, M. Rejkuba, and D. Romano, editors, *The General Assembly of Galaxy Halos: Structure, Origin and Evolution*, volume 317 of *IAU Symposium*, pages 1–8, Aug 2016.

[124] K. V. Johnston, J. S. Bullock, S. Sharma, A. Font, B. E. Robertson, and S. N. Leitner. Tracing Galaxy Formation with Stellar Halos. II. Relating Substructure in Phase and Abundance Space to Accretion Histories. , 689:936–957, Dec. 2008.

[125] E. Jones, T. Oliphant, P. Peterson, et al. SciPy: Open source scientific tools for Python, 2001. [Online; accessed 2015-08-25].

[126] M. Jurić, Ž. Ivezić, A. Brooks, R. H. Lupton, D. Schlegel, D. Finkbeiner, N. Padmanabhan, N. Bond, B. Sesar, C. M. Rockosi, G. R. Knapp, J. E. Gunn, T. Sumi, D. P. Schneider, J. C. Barentine, H. J. Brewington, J. Brinkmann, M. Fukugita, M. Harvanek, S. J. Kleinman, J. Krzesinski, D. Long, J. Neilsen, Eric H., A. Nitta, S. A. Snedden, and D. G. York. The Milky Way Tomography with SDSS. I. Stellar Number Density Distribution. , 673(2):864–914, Feb. 2008.

[127] R. Kannan, A. V. Macciò, F. Fontanot, B. P. Moster, W. Karman, and R. S. Somerville. From discs to bulges: effect of mergers on the morphology of galaxies. , 452(4):4347–4360, Oct. 2015.

[128] S. A. Kassin, B. J. Weiner, S. M. Faber, J. P. Gardner, C. N. A. Willmer, A. L. Coil, M. C. Cooper, J. Devriendt, A. A. Dutton, P. Guhathakurta, D. C. Koo, A. J. Metevier, K. G. Noeske, and J. R. Primack. The Epoch of Disk Settling: z ~1 to Now. , 758(2):106, Oct. 2012.

[129] N. Katz, D. H. Weinberg, and L. Hernquist. Cosmological Simulations with TreeSPH. , 105:19, Jul 1996.

[130] S. Kazantzidis, J. S. Bullock, A. R. Zentner, A. V. Kravtsov, and L. A. Moustakas. Cold Dark Matter Substructure and Galactic Disks. I. Morphological Signatures of Hierarchical Satellite Accretion. , 688(1):254–276, Nov. 2008.

[131] L. Z. Kelley. kalepy: a python package for kernel density estimation, sampling and plotting. *Journal of Open Source Software*, 6(57):2784, 2021.

[132] S. M. Kent. CCD surface photometry of field galaxies. II. Bulge/disk decompositions. , 59:115–159, Oct. 1985.

[133] A. Knebe, N. I. Libeskind, F. Pearce, P. Behroozi, J. Casado, K. Dolag, R. Dominguez-Tenreiro, P. Elahi, H. Lux, S. I. Muldrew, and J. Onions. Galaxies going MAD: the Galaxy-Finder Comparison Project. , 428(3):2039–2052, Jan. 2013.

[134] J. Kormendy. Internal and environmental secular evolution of disk galaxies. *Highlights of Astronomy*, 16:316–317, Mar. 2015.

[135] J. Kormendy and J. Kennicutt, Robert C. Secular Evolution and the Formation of Pseudobulges in Disk Galaxies. , 42(1):603–683, Sept. 2004.

[136] M. Kretschmer, A. Dekel, and R. Teyssier. On the origin of surprisingly cold gas discs in galaxies at high redshift. , 510(3):3266–3275, Mar. 2022.

[137] M. R. Krumholz and N. Y. Gnedin. A Comparison of Methods for Determining the Molecular Content of Model Galaxies. , 729(1):36, Mar 2011.

[138] Y. S. Lee, T. C. Beers, D. An, Ž. Ivezić, A. Just, C. M. Rockosi, H. L. Morrison, J. A. Johnson, R. Schönrich, J. Bird, B. Yanny, P. Harding, and H. J. Rocha-Pinto. Formation and Evolution of the Disk System of the Milky Way: [α/Fe] Ratios and Kinematics of the SEGUE G-dwarf Sample. , 738(2):187, Sept. 2011.

[139] M. D. Lehnert, P. Di Matteo, M. Haywood, and O. N. Snaith. The Milky Way as a High-redshift Galaxy: The Importance of Thick Disk Formation in Galaxies. , 789(2):L30, July 2014.

[140] A. Leroy, A. Bolatto, F. Walter, and L. Blitz. Molecular Gas in the Low-Metallicity, Star-forming Dwarf IC 10. , 643(2):825–843, Jun 2006.

[141] J. Lian, D. Thomas, C. Maraston, T. C. Beers, C. Moni Bidin, J. G. Fernández-Trincado, D. A. García-Hernández, R. R. Lane, R. R. Munoz, C. Nitschelm, A. Roman-Lopes, and O. Zamora. The age-chemical abundance structure of the Galactic disc - II. α-dichotomy and thick disc formation. , 497(2):2371–2384, Sept. 2020.

[142] J. Lian, D. Thomas, C. Maraston, O. Zamora, J. Tayar, K. Pan, P. Tissera, J. G. Fernández-Trincado, and D. A. Garcia-Hernandez. The age-chemical abundance structure of the Galaxy I: evidence for a late-accretion event in the outer disc at z $\sim$ 0.6. , 494(2):2561–2575, May 2020.

[143] T. C. Licquia and J. A. Newman. Improved Estimates of the Milky Way's Stellar Mass and Star Formation Rate from Hierarchical Bayesian Meta-Analysis. , 806(1):96, Jun 2015.

[144] B. Lindblad. On the Cause of Star-Streaming. , 62:191, Oct. 1925.

[145] X. Ma, M. Y. Grudić, E. Quataert, P. F. Hopkins, C.-A. Faucher-Giguère, M. Boylan-Kolchin, A. Wetzel, J.-h. Kim, N. Murray, and D. Kereš. Self-consistent proto-globular cluster formation in cosmological simulations of high-redshift galaxies. , 493(3):4315–4332, Apr. 2020.

[146] X. Ma, P. F. Hopkins, R. Feldmann, P. Torrey, C.-A. Faucher-Giguère, and D. Kereš. Why do high-redshift galaxies show diverse gas-phase metallicity gradients? , 466(4):4780–4794, Apr. 2017.

[147] X. Ma, P. F. Hopkins, A. R. Wetzel, E. N. Kirby, D. Anglés-Alcázar, C.-A. Faucher-Giguère, D. Kereš, and E. Quataert. The structure and dynamical evolution of the stellar disc of a simulated Milky Way-mass galaxy. , 467(2):2430–2444, May 2017.

[148] X. Ma, E. Quataert, A. Wetzel, P. F. Hopkins, C.-A. Faucher-Giguère, and D. Kereš. No missing photons for reionization: moderate ionizing photon escape fractions from the FIRE-2 simulations. , 498(2):2001–2017, Oct. 2020.

[149] L. A. MacArthur, S. Courteau, and J. A. Holtzman. Structure of Disk-dominated Galaxies. I. Bulge/Disk Parameters, Simulations, and Secular Evolution. , 582(2):689–722, Jan. 2003.

[150] J. T. Mackereth and J. Bovy. Weighing the stellar constituents of the galactic halo with APOGEE red giant stars. , 492(3):3631–3646, Mar. 2020.

[151] J. T. Mackereth, J. Bovy, R. P. Schiavon, G. Zasowski, K. Cunha, P. M. Frinchaboy, A. E. García Perez, M. R. Hayden, J. Holtzman, S. R. Majewski, S. Mészáros, D. L. Nidever, M. Pinsonneault, and M. D. Shetrone. The age-metallicity structure of the Milky Way disc using APOGEE. , 471(3):3057–3078, Nov. 2017.

[152] J. T. Mackereth, R. P. Schiavon, J. Pfeffer, C. R. Hayes, J. Bovy, B. Anguiano, C. Allende Prieto, S. Hasselquist, J. Holtzman, J. A. Johnson, S. R. Majewski, R. O'Connell, M. Shetrone, P. B. Tissera, and J. G. Fernández-Trincado. The origin of accreted stellar halo populations in the Milky Way using APOGEE, Gaia, and the EAGLE simulations. , 482(3):3426–3442, Jan 2019.

[153] R. Maiolino, H. R. Russell, A. C. Fabian, S. Carniani, R. Gallagher, S. Cazzoli, S. Arribas, F. Belfiore, E. Bellocchi, L. Colina, G. Cresci, W. Ishibashi, A. Marconi, F. Mannucci, E. Oliva, and E. Sturm. Star formation inside a galactic outflow. , 544:202–206, Mar. 2017.

[154] D. Maoz and C. Badenes. The supernova rate and delay time distribution in the Magellanic Clouds. , 407:1314–1327, Sept. 2010.

[155] M. Martig, I. Minchev, M. Ness, M. Fouesneau, and H.-W. Rix. A Radial Age Gradient in the Geometrically Thick Disk of the Milky Way. , 831(2):139, Nov. 2016.

[156] D. Martizzi. Global simulations of galactic discs: violent feedback from clustered supernovae during bursts of star formation. , 492(1):79–95, Feb. 2020.

[157] T. Matsuno, W. Aoki, and T. Suda. Origin of the Excess of High-energy Retrograde Stars in the Galactic Halo. , 874(2):L35, Apr 2019.

[158] A. W. McConnachie, M. J. Irwin, R. A. Ibata, J. Dubinski, L. M. Widrow, N. F. Martin, P. Côté, A. L. Dotter, J. F. Navarro, A. M. N. Ferguson, T. H. Puzia, G. F. Lewis, A. Babul, P. Barmby, O. Bienaymé, S. C. Chapman, R. Cockcroft, M. L. M. Collins, M. A. Fardal, W. E. Harris, A. Huxor, A. D. Mackey, J. Peñarrubia, R. M. Rich, H. B. Richer, A. Siebert, N. Tanvir, D. Valls-Gabaud, and K. A. Venn. The remnants of galaxy formation from a panoramic survey of the region around M31. , 461:66–69, Sept. 2009.

[159] R. McCray and M. Kafatos. Supershells and Propagating Star Formation. , 317:190, Jun 1987.

[160] X. Meng and O. Y. Gnedin. Evolution of disc thickness in simulated high-redshift galaxies. , 502(1):1433–1440, Mar. 2021.

[161] I. Minchev and B. Famaey. A New Mechanism for Radial Migration in Galactic Disks: Spiral-Bar Resonance Overlap. , 722(1):112–121, Oct. 2010.

[162] A. L. Muratov, D. Kereš, C.-A. Faucher-Giguère, P. F. Hopkins, E. Quataert, and N. Murray. Gusty, gaseous flows of FIRE: galactic winds in cosmological simulations with explicit stellar feedback. , 454(3):2691–2713, Dec. 2015.

[163] G. C. Myeong, E. Vasiliev, G. Iorio, N. W. Evans, and V. Belokurov. Evidence for two early accretion events that built the Milky Way stellar halo. , 488(1):1235–1247, Sep 2019.

[164] J. F. Navarro, C. Yozin, N. Loewen, A. Benítez-Llambay, A. Fattahi, C. S. Frenk, K. A. Oman, J. Schaye, and T. Theuns. The innate origin of radial and vertical gradients in a simulated galaxy disc. , 476(3):3648–3660, May 2018.

[165] L. Necib, B. Ostdiek, M. Lisanti, T. Cohen, M. Freytsis, S. Garrison-Kimmel, P. F. Hopkins, A. Wetzel, and R. Sanderson. Evidence for a Vast Prograde Stellar Stream in the Solar Vicinity. *arXiv e-prints*, page arXiv:1907.07190, Jul 2019.

[166] M. Ness and D. Lang. The X-shaped Bulge of the Milky Way Revealed by WISE. , 152(1):14, July 2016.

[167] F. Nikakhtar, R. E. Sanderson, A. Wetzel, S. Loebman, S. Sharma, R. Beaton, J. T. Mackereth, V. J. Poovelil, G. Zasowski, A. Bonaca, S. Martell, H. Jönsson, and C.-A. Faucher-Giguère. New Families in our Solar Neighborhood: Applying Gaussian Mixture Models for Objective Classification of Structures in the Milky Way and in Simulations. , 921(2):106, Nov. 2021.

[168] P. E. Nissen and W. J. Schuster. Two distinct halo populations in the solar neighborhood. Evidence from stellar abundance ratios and kinematics. , 511:L10, Feb. 2010.

[169] C. A. Norman, J. A. Sellwood, and H. Hasan. Bar Dissolution and Bulge Formation: an Example of Secular Dynamical Evolution in Galaxies. , 462:114, May 1996.

[170] J. Oñorbe, S. Garrison-Kimmel, A. H. Maller, J. S. Bullock, M. Rocha, and O. Hahn. How to zoom: bias, contamination and Lagrange volumes in multimass cosmological simulations. , 437(2):1894–1908, Jan. 2014.

[171] T. Okamoto. The origin of pseudo-bulges in cosmological simulations of galaxy formation. , 428(1):718–728, Jan. 2013.

[172] T. Okamoto, C. S. Frenk, A. Jenkins, and T. Theuns. The properties of satellite galaxies in simulations of galaxy formation. , 406(1):208–222, July 2010.

[173] J. H. Oort. Some peculiarities in the motion of stars of high velocity. , 1:133, Sept. 1922.

[174] M. E. Orr, C. C. Hayward, P. F. Hopkins, T. K. Chan, C.-A. Faucher-Giguère, R. Feldmann, D. Kereš, N. Murray, and E. Quataert. What FIREs up star formation: the emergence of the Kennicutt-Schmidt law from feedback. , 478(3):3653–3673, Aug 2018.

[175] S. Ortolani, A. Renzini, R. Gilmozzi, G. Marconi, B. Barbuy, E. Bica, and R. M. Rich. Near-coeval formation of the Galactic bulge and halo inferred from globular cluster ages. , 377(6551):701–704, Oct. 1995.

[176] C. Osborne, S. Salim, I. Damjanov, S. M. Faber, M. Huertas-Company, D. C. Koo, K. B. Mantha, D. H. McIntosh, J. R. Primack, and S. Tacchella. CANDELS Meets GSWLC: Evolution of the Relationship between Morphology and Star Formation Since z = 2. , 902(1):77, Oct. 2020.

[177] R. A. Overzier, T. M. Heckman, D. Schiminovich, A. Basu-Zych, T. Gonçalves, D. C. Martin, and R. M. Rich. Morphologies of Local Lyman Break Galaxy Analogs. II. A Comparison with Galaxies at z ~= 2-4 in ACS and WFC3 Images of the Hubble Ultra Deep Field. , 710(2):979–991, Feb. 2010.

[178] M. J. Park, S. K. Yi, S. Peirani, C. Pichon, Y. Dubois, H. Choi, J. Devriendt, S. Kaviraj, T. Kimm, K. Kraljic, and M. Volonteri. Exploring the Origin of Thick Disks Using the NewHorizon and Galactica Simulations. , 254(1):2, May 2021.

[179] F. Pedregosa, G. Varoquaux, A. Gramfort, V. Michel, B. Thirion, O. Grisel, M. Blondel, A. Müller, J. Nothman, G. Louppe, P. Prettenhofer, R. Weiss, V. Dubourg, J. Vanderplas, A. Passos, D. Cournapeau, M. Brucher, M. Perrot, and É. Duchesnay. Scikit-learn: Machine Learning in Python. *arXiv e-prints*, page arXiv:1201.0490, Jan. 2012.

[180] F. Pérez and B. E. Granger. IPython: a system for interactive scientific computing. *Computing in Science and Engineering*, 9(3):21–29, May 2007.

[181] A. Pillepich, D. Nelson, V. Springel, R. Pakmor, P. Torrey, R. Weinberger, M. Vogelsberger, F. Marinacci, S. Genel, A. van der Wel, and L. Hernquist. First results from the TNG50 simulation: the evolution of stellar and gaseous discs across cosmic time. , 490(3):3196–3233, Dec. 2019.

[182] J. X. Prochaska, S. O. Naumov, B. W. Carney, A. McWilliam, and A. M. Wolfe. The Galactic Thick Disk Stellar Abundances. , 120(5):2513–2549, Nov. 2000.

[183] C. W. Purcell, J. S. Bullock, and S. Kazantzidis. Heated disc stars in the stellar halo. , 404:1711–1718, June 2010.

[184] C. W. Purcell, J. S. Bullock, E. J. Tollerud, M. Rocha, and S. Chakrabarti. The Sagittarius impact as an architect of spirality and outer rings in the Milky Way. , 477(7364):301–303, Sep 2011.

[185] C. W. Purcell, S. Kazantzidis, and J. S. Bullock. The Destruction of Thin Stellar Disks Via Cosmologically Common Satellite Accretion Events. , 694(2):L98–L102, Apr. 2009.

[186] P. J. Quinn, L. Hernquist, and D. P. Fullagar. Heating of Galactic Disks by Mergers. , 403:74, Jan. 1993.

[187] N. Raha, J. A. Sellwood, R. A. James, and F. D. Kahn. A dynamical instability of bars in disk galaxies. , 352(6334):411–412, Aug. 1991.

[188] A. Recio-Blanco, P. de Laverny, G. Kordopatis, A. Helmi, V. Hill, G. Gilmore, R. Wyse, V. Adibekyan, S. Randich, M. Asplund, S. Feltzing, R. Jeffries, G. Micela, A. Vallenari, E. Alfaro, C. Allende Prieto, T. Bensby, A. Bragaglia, E. Flaccomio, S. E. Koposov, A. Korn, A. Lanzafame, E. Pancino, R. Smiljanic, R. Jackson, J. Lewis, L. Magrini, L. Morbidelli, L. Prisinzano, G. Sacco, C. C. Worley, A. Hourihane, M. Bergemann, M. T. Costado, U. Heiter, P. Joffre, C. Lardo, K. Lind, and E. Maiorca. The Gaia-ESO Survey: the Galactic thick to thin disc transition. , 567:A5, July 2014.

[189] A. Renzini. Origin of Bulges. In C. M. Carollo, H. C. Ferguson, and R. F. G. Wyse, editors, *The Formation of Galactic Bulges*, page 9, Jan. 1999.

[190] A. J. Richings and C.-A. Faucher-Giguère. Radiative cooling of swept-up gas in AGN-driven galactic winds and its implications for molecular outflows. , 478(3):3100–3119, Aug 2018.

[191] A. J. Richings and C.-A. Faucher-Giguère. The origin of fast molecular outflows in quasars: molecule formation in AGN-driven galactic winds. , 474(3):3673–3699, Mar 2018.

[192] F. Rizzo, S. Vegetti, D. Powell, F. Fraternali, J. P. McKean, H. R. Stacey, and S. D. M. White. A dynamically cold disk galaxy in the early Universe. , 584(7820):201–204, Aug. 2020.

[193] B. Robertson, J. S. Bullock, T. J. Cox, T. Di Matteo, L. Hernquist, V. Springel, and N. Yoshida. A Merger-driven Scenario for Cosmological Disk Galaxy Formation. , 645(2):986–1000, July 2006.

[194] B. Robertson, J. S. Bullock, A. S. Font, K. V. Johnston, and L. Hernquist. Λ Cold Dark Matter, Stellar Feedback, and the Galactic Halo Abundance Pattern. , 632(2):872–881, Oct 2005.

[195] B. Rodríguez del Pino, S. Arribas, J. Piqueras López, M. Villar-Martín, and L. Colina. Properties of ionized outflows in MaNGA DR2 galaxies. , 486(1):344–359, Jun 2019.

[196] K. Sakamoto, S. Aalto, D. J. Wilner, J. H. Black, J. E. Conway, F. Costagliola, A. B. Peck, M. Spaans, J. Wang, and M. C. Wiedner. P Cygni Profiles of Molecular Lines Toward Arp 220 Nuclei. , 700:L104–L108, Aug. 2009.

[197] J. Samuel, A. Wetzel, E. Tollerud, S. Garrison-Kimmel, S. Loebman, K. El-Badry, P. F. Hopkins, M. Boylan-Kolchin, C.-A. Faucher-Giguère, J. S. Bullock, S. Benincasa, and J. Bailin. A profile in FIRE: resolving the radial distributions of satellite galaxies in the Local Group with simulations. , 491(1):1471–1490, Jan. 2020.

[198] R. E. Sanderson, S. Garrison-Kimmel, A. Wetzel, T. Keung Chan, P. F. Hopkins, D. Kereš, I. Escala, C.-A. Faucher-Giguère, and X. Ma. Reconciling Observed and Simulated Stellar Halo Masses. , 869(1):12, Dec 2018.

[199] R. E. Sanderson, A. Wetzel, S. Loebman, S. Sharma, P. F. Hopkins, S. Garrison-Kimmel, C.-A. Faucher-Giguère, D. Kereš, and E. Quataert. Synthetic Gaia surveys from the FIRE cosmological simulations of Milky-Way-mass galaxies. *arXiv e-prints*, page arXiv:1806.10564, Jun 2018.

[200] R. E. Sanderson, A. Wetzel, S. Loebman, S. Sharma, P. F. Hopkins, S. Garrison-Kimmel, C.-A. Faucher-Giguère, D. Kereš, and E. Quataert. Synthetic Gaia Surveys from the FIRE Cosmological Simulations of Milky Way-mass Galaxies. , 246(1):6, Jan. 2020.

[201] I. B. Santistevan, A. Wetzel, R. E. Sanderson, K. El-Badry, J. Samuel, and C.-A. Faucher-Giguére. The origin of metal-poor stars on prograde disk orbits in FIRE simulations of Milky Way-mass galaxies. , May 2021.

[202] C. Scannapieco, S. D. M. White, V. Springel, and P. B. Tissera. The formation and survival of discs in a ΛCDM universe. , 396(2):696–708, June 2009.

[203] K. C. Schlaufman, C. M. Rockosi, C. Allende Prieto, T. C. Beers, D. Bizyaev, H. Brewington, Y. S. Lee, V. Malanushenko, E. Malanushenko, D. Oravetz, K. Pan, A. Simmons, S. Snedden, and B. Yanny. Insight into the Formation of the Milky Way Through Cold Halo Substructure. I. The ECHOS of Milky Way Formation. , 703(2):2177–2204, Oct. 2009.

[204] E. E. Schneider and B. E. Robertson. Hydrodynamical Coupling of Mass and Momentum in Multiphase Galactic Winds. , 834(2):144, Jan 2017.

[205] E. E. Schneider, B. E. Robertson, and T. A. Thompson. Production of Cool Gas in Thermally Driven Outflows. , 862(1):56, Jul 2018.

[206] L. Searle and R. Zinn. Compositions of halo clusters and the formation of the galactic halo. , 225:357–379, Oct. 1978.

[207] F. Sestito, N. F. Martin, E. Starkenburg, A. Arentsen, R. A. Ibata, N. Longeard, C. Kielty, K. Youakim, K. A. Venn, D. S. Aguado, R. G. Carlberg, J. I. González Hernández, V. Hill, P. Jablonka, G. Kordopatis, K. Malhan, J. F. Navarro, R. Sánchez-Janssen, G. Thomas, E. Tolstoy, T. G. Wilson, P. A. Palicio, S. Bialek, R. Garcia-Dias, R. Lucchesi, P. North, Y. Osorio, L. R. Patrick, and L. Peralta de Arriba. The Pristine survey - X. A large population of low-metallicity stars permeates the Galactic disc. , 497(1):L7–L12, Sept. 2020.

[208] K. L. Shapiro, R. Genzel, N. M. Förster Schreiber, L. J. Tacconi, N. Bouché, G. Cresci, R. Davies, F. Eisenhauer, P. H. Johansson, D. Krajnović, D. Lutz, T. Naab, N. Arimoto, S. Arribas, A. Cimatti, L. Colina, E. Daddi, O. Daigle, D. Erb, O. Hernandez,

X. Kong, M. Mignoli, M. Onodera, A. Renzini, A. Shapley, and C. Steidel. Kinemetry of SINS High-Redshift Star-Forming Galaxies: Distinguishing Rotating Disks from Major Mergers. , 682(1):231–251, July 2008.

[209] S. Sharma, M. R. Hayden, and J. Bland-Hawthorn. Chemical enrichment and radial migration in the Galactic disc - the origin of the [αFe] double sequence. , 507(4):5882–5901, Nov. 2021.

[210] S. Sharma, D. Stello, J. Bland-Hawthorn, M. R. Hayden, J. C. Zinn, T. Kallinger, M. Hon, M. Asplund, S. Buder, G. h. M. De Silva, V. D'Orazi, K. Freeman, J. Kos, G. F. Lewis, J. Lin, K. Lind, S. Martell, J. D. Simpson, R. A. Wittenmyer, D. B. Zucker, T. Zwitter, T. R. Bedding, B. Chen, K. Cotar, J. Esdaile, J. Horner, D. Huber, P. R. Kafle, S. Khanna, T. Li, Y.-S. Ting, D. M. Nataf, T. Nordlander, M. H. M. Saadon, G. Traven, D. Wright, and R. F. G. Wyse. The K2-HERMES Survey: age and metallicity of the thick disc. , 490(4):5335–5352, Dec. 2019.

[211] I. T. Simion, V. Belokurov, and S. E. Koposov. Common origin for Hercules-Aquila and Virgo Clouds in Gaia DR2. , 482:921–928, Jan. 2019.

[212] O. N. Snaith, M. Haywood, P. Di Matteo, M. D. Lehnert, F. Combes, D. Katz, and A. Gómez. The Dominant Epoch of Star Formation in the Milky Way Formed the Thick Disk. , 781(2):L31, Feb. 2014.

[213] M. Sparre, C. C. Hayward, R. Feldmann, C.-A. Faucher-Giguère, A. L. Muratov, D. Kereš, and P. F. Hopkins. (Star)bursts of FIRE: observational signatures of bursty star formation in galaxies. , 466(1):88–104, Apr. 2017.

[214] L. V. Spiegel and E. V. Polyachenko. Pseudobulge formation in the Milky Way type galaxies as a result of buckling instability. *INASAN Science Reports*, 4:381–388, Oct. 2019.

[215] J. Stebbins and A. E. Whitford. Six-Color Photometry of Stars. V. Infrared Radiation from the Region of the Galactic Center. , 106:235, Sept. 1947.

[216] J. Stern, C.-A. Faucher-Giguère, D. Fielding, E. Quataert, Z. Hafen, A. B. Gurvich, X. Ma, L. Byrne, K. El-Badry, D. Anglés-Alcázar, T. K. Chan, R. Feldmann, D. Kereš, A. Wetzel, N. Murray, and P. F. Hopkins. Virialization of the Inner CGM in the FIRE Simulations and Implications for Galaxy Disks, Star Formation, and Feedback. , 911(2):88, Apr. 2021.

[217] E. Sturm, E. González-Alfonso, S. Veilleux, J. Fischer, J. Graciá-Carpio, S. Hailey-Dunsheath, A. Contursi, A. Poglitsch, A. Sternberg, R. Davies, R. Genzel, D. Lutz, L. Tacconi, A. Verma, R. Maiolino, and J. A. de Jong. Massive Molecular Outflows and Negative Feedback in ULIRGs Observed by Herschel-PACS. , 733:L16, May 2011.

[218] K.-Y. Su, P. F. Hopkins, C. C. Hayward, C.-A. Faucher-Giguère, D. Kereš, X. Ma, and V. H. Robles. Feedback first: the surprisingly weak effects of magnetic fields, viscosity, conduction and metal diffusion on sub-L* galaxy formation. , 471:144–166, Oct. 2017.

[219] T. Tamfal, L. Mayer, T. R. Quinn, A. Babul, P. Madau, P. R. Capelo, S. Shen, and M. Staub. The Dawn of Disk Formation in a Milky Way-sized Galaxy Halo: Thin Stellar Disks at z ¿ 4. , 928(2):106, Apr. 2022.

[220] D. M. Terndrup. The Structure and Stellar Population of the Galactic Nuclear Bulge. , 96:884, Sept. 1988.

[221] T. A. Thompson, E. Quataert, D. Zhang, and D. H. Weinberg. An origin for multiphase gas in galactic winds and haloes. , 455(2):1830–1844, Jan 2016.

[222] A. L. Tiley, S. Gillman, L. Cortese, A. M. Swinbank, U. Dudzevičiūtė, C. M. Harrison, I. Smail, D. Obreschkow, S. M. Croom, R. M. Sharples, and A. Puglisi. The KMOS galaxy evolution survey (KGES): the angular momentum of star-forming galaxies over the last 10 Gyr. , 506(1):323–342, Sept. 2021.

[223] V. Tsikoudi. Photometry and structure of lenticular galaxies. I - NGC 3115. , 234:842–853, Dec. 1979.

[224] E. Valenti, M. Zoccali, A. Renzini, T. M. Brown, O. A. Gonzalez, D. Minniti, V. P. Debattista, and L. Mayer. Stellar ages through the corners of the boxy bulge. , 559:A98, Nov. 2013.

[225] F. C. van den Bosch. The Formation of Disk-Bulge-Halo Systems and the Origin of the Hubble Sequence. , 507(2):601–614, Nov. 1998.

[226] P. C. van der Kruit and K. C. Freeman. Galaxy Disks. , 49(1):301–371, Sept. 2011.

[227] S. Veilleux, G. Cecil, and J. Bland-Hawthorn. Galactic Winds. , 43:769–826, Sept. 2005.

[228] D. H. Weinberg, J. A. Holtzman, S. Hasselquist, J. C. Bird, J. A. Johnson, M. Shetrone, J. Sobeck, C. Allende Prieto, D. Bizyaev, R. Carrera, R. E. Cohen, K. Cunha, G. Ebelke, J. G. Fernandez-Trincado, D. A. García-Hernández, C. R. Hayes, H. Jönsson, R. R. Lane, S. R. Majewski, V. Malanushenko, S. Mészáros, D. L. Nidever, C. Nitschelm, K. Pan, H.-W. Rix, J. Rybizki, R. P. Schiavon, D. P. Schneider, J. C. Wilson, and O. Zamora. Chemical Cartography with APOGEE: Multi-element Abundance Ratios. , 874(1):102, Mar. 2019.

[229] A. R. Wetzel, P. F. Hopkins, J.-h. Kim, C.-A. Faucher-Giguère, D. Kereš, and E. Quataert. Reconciling Dwarf Galaxies with ΛCDM Cosmology: Simulating a Realistic Population of Satellites around a Milky Way mass Galaxy. , 827:L23, Aug. 2016.

[230] E. Wisnioski, N. M. Förster Schreiber, S. Wuyts, E. Wuyts, K. Bandara, D. Wilman, R. Genzel, R. Bender, R. Davies, M. Fossati, P. Lang, J. T. Mendel, A. Beifiori, G. Brammer, J. Chan, M. Fabricius, Y. Fudamoto, S. Kulkarni, J. Kurk, D. Lutz, E. J. Nelson, I. Momcheva, D. Rosario, R. Saglia, S. Seitz, L. J. Tacconi, and P. G. van Dokkum. The KMOS^{3D} Survey: Design, First Results, and the Evolution of Galaxy Kinematics from 0.7 ¡= z ¡= 2.7. , 799(2):209, Feb. 2015.

[231] S. Wuyts, N. M. Förster Schreiber, R. Genzel, Y. Guo, G. Barro, E. F. Bell, A. Dekel, S. M. Faber, H. C. Ferguson, M. Giavalisco, N. A. Grogin, N. P. Hathi, K.-H. Huang, D. D. Kocevski, A. M. Koekemoer, D. C. Koo, J. Lotz, D. Lutz, E. McGrath, J. A. Newman, D. Rosario, A. Saintonge, L. J. Tacconi, B. J. Weiner, and A. van der Wel. Smooth(er) Stellar Mass Maps in CANDELS: Constraints on the Longevity of Clumps in High-redshift Star-forming Galaxies. , 753(2):114, July 2012.

[232] S. Wuyts, N. M. Förster Schreiber, A. van der Wel, B. Magnelli, Y. Guo, R. Genzel, D. Lutz, H. Aussel, G. Barro, S. Berta, A. Cava, J. Graciá-Carpio, N. P. Hathi, K.-H. Huang, D. D. Kocevski, A. M. Koekemoer, K.-S. Lee, E. Le Floc'h, E. J. McGrath, R. Nordon, P. Popesso, F. Pozzi, L. Riguccini, G. Rodighiero, A. Saintonge, and L. Tacconi. Galaxy Structure and Mode of Star Formation in the SFR-Mass Plane from z ~2.5 to z ~0.1. , 742(2):96, Dec. 2011.

[233] R. Yamaguchi, N. Mizuno, T. Onishi, A. Mizuno, and Y. Fukui. Molecular Clouds in the Supergiant Shell LMC 4: Evidence for Triggered Cluster Formation. , 553(2):L185–L188, Jun 2001.

[234] P. Yoachim and J. J. Dalcanton. Structural Parameters of Thin and Thick Disks in Edge-on Disk Galaxies. , 131(1):226–249, Jan. 2006.

[235] P. Yoachim and J. J. Dalcanton. Lick Indices in the Thin and Thick Disks of Edge-On Disk Galaxies. , 683(2):707–721, Aug. 2008.

[236] S. Yu, J. S. Bullock, C. Klein, J. Stern, A. Wetzel, X. Ma, J. Moreno, Z. Hafen, A. B. Gurvich, P. F. Hopkins, D. Kereš, C.-A. Faucher-Giguère, R. Feldmann, and E. Quataert. The bursty origin of the Milky Way thick disc. , 505(1):889–902, July 2021.

[237] A. Zanella, A. Pallottini, A. Ferrara, S. Gallerani, S. Carniani, M. Kohandel, and C. Behrens. Early galaxy growth: mergers or gravitational instability? , 500(1):118–137, Jan. 2021.

[238] M. Zoccali, A. Renzini, S. Ortolani, L. Greggio, I. Saviane, S. Cassisi, M. Rejkuba, B. Barbuy, R. M. Rich, and E. Bica. Age and metallicity distribution of the Galactic bulge from extensive optical and near-IR stellar photometry. , 399:931–956, Mar. 2003.

[239] A. Zolotov, B. Willman, A. M. Brooks, F. Governato, C. B. Brook, D. W. Hogg, T. Quinn, and G. Stinson. The Dual Origin of Stellar Halos. , 702:1058–1067, Sept. 2009.

[240] A. H. Zonoozi, H. Mahani, and P. Kroupa. Was the Milky Way a chain galaxy? Using the IGIMF theory to constrain the thin-disc star formation history and mass. , 483(1):46–56, Feb 2019.

[241] K. Zubovas and A. R. King. Galaxy-wide outflows: cold gas and star formation at high speeds. , 439(1):400–406, Mar 2014.

Appendix A

Appendix

A.1 Outflow stars with more conservative star formation criteria

In order to test the robustness of our stellar outflow predictions to star formation recipe, we have rerun simulation `m12w` over a period spanning a lookback time from 1.4 to 1.25 Gyr using stricter star formation criteria. The results are shown in Figure A.1, which shows the star formation histories as in Figure 2.9 with global star formation rate vs. time on top and outflow star formation rate on the bottom.

The standard FIRE-2 star formation criterion (labeled "SF = 0") demands that star formation occurs within gas clouds that are locally self-gravitating. In our re-runs, we also require that the thermal Jeans mass be below $1000 M_{\odot}$, that the gas be part of a convergent flow, and that the gas be gravitationally bound as evaluated from the usual virial parameter, but smoothed over 0.125 local freefall times (labeled "SF = 3" [101]). The top panel shows the total star formation rate averaged over 2.8 Myr for the two runs and the bottom panels show

the stellar outflow star formation rate. Here outflows are defined as stars that were formed with $V_{\rm rad}^{\rm birth} > 150\,{\rm km\,s^{-1}}$.

The number of total new stars and outflow stars formed during this period is approximately the same for the two criterion. The difference between global and outflow star formation is smaller than 2%. Although the detailed star formation histories for the two runs are different, the general trend seems very similar. The outflow events correlate with starburst activity in the main galaxy. This is consistent with the idea that these events are triggered by clustered supernova feedback.

A.2 Observable properties of inner stellar halo stars: outflow stars vs. bulk

In §2.5.3, we discussed the contribution of stars made in outflows to the kinematically-identified local stellar halos of our simulated galaxies. We found that the bulk of the local halo was comprised of heated stars and accreted stars, with a minority coming from stars born in outflows. Here we show that it may be difficult to distinguish between outflow stars and other local halo stars using either chemical properties (Figure A.2) or kinematic properties (Figure A.3) separately. In §2.5.3, we showed that the joint combination of high metallicty and high radial velocity helps to single out stars that were born in outflows.

Figure A.2 shows the densities of stars in `m12i` identified as being born in outflows (right, defined as $V_{\rm rad}^{\rm birth} > 150\,{\rm km\,s^{-1}}$) and other stars (left) in the space of [Mg/Fe] versus [Fe/H]. Note that the number of stars made in outflows is relatively small compared to the other stars. There are no obvious differences between the two population.

In Figure A.3, we make similar comparison between the same population for their current

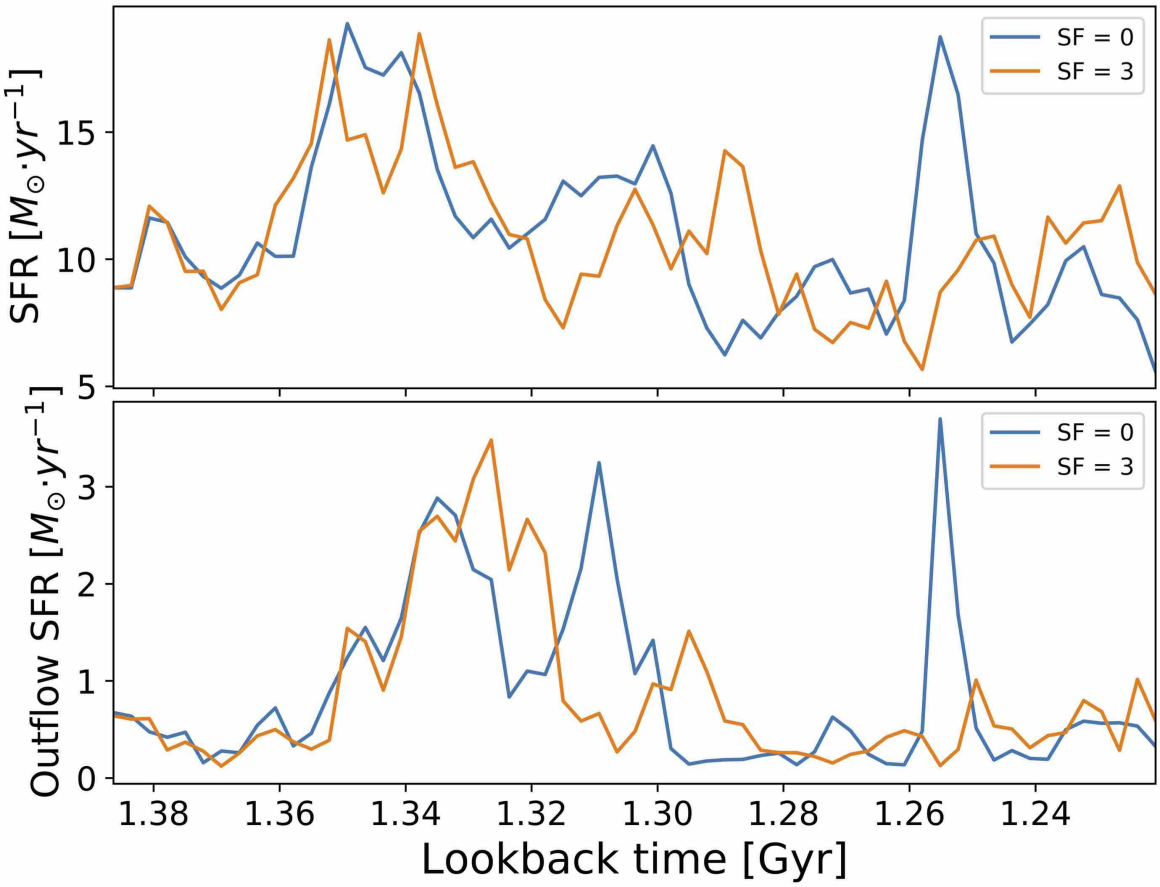

Figure A.1: Instantaneous star formation rates for total stars (top panels) compared to stellar outflow star formation rate (bottom panels) for two reruns of `m12w` with different star formation criterion. Star formation rates are averaged over 2.8 Myr. Outflows are defined as stars that were formed with $V_{\rm rad}^{\rm birth} > 150\,{\rm km\,s^{-1}}$. Lines labeled "SF=0" use the standard FIRE-2 star formation criteria. Lines labeled "SF=3" are more conservative, demanding convergent flow, completely zero star formation in any unbound regions and that the thermal Jeans mass be below $1000 M_\odot$ (see Grudić et al. 2018 [101]).

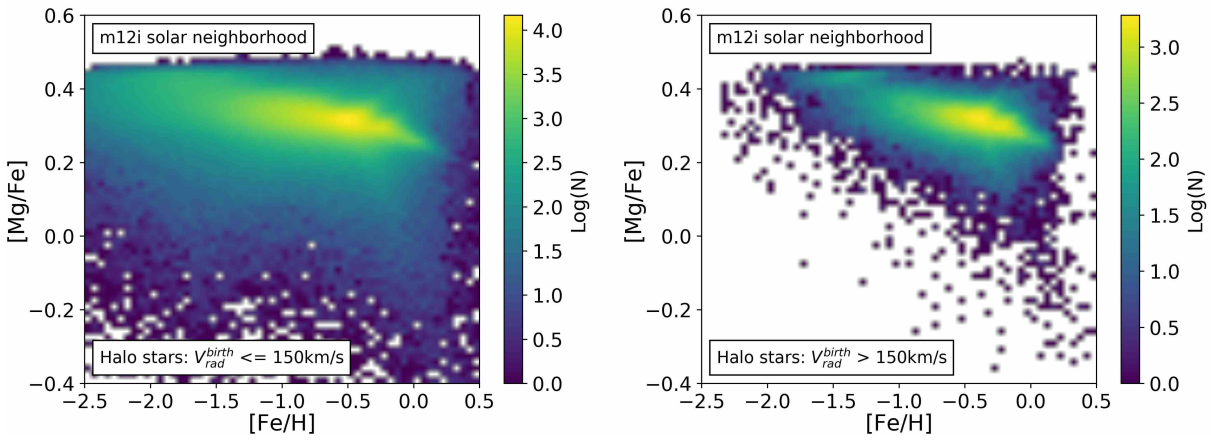

Figure A.2: Chemical abundances for the local stellar halo in `m12i` split by birth radial velocity, with stars identified as being born in outflows shown on the right and other stars shown on the left. At fixed [Fe/H], differences are not substantial.

radial (left) and tangential (right) velocities. The two populations are virtually identical in tangential velocity space. In radial velocity, the distributions show some differences (with outflow material peaked towards both high and low velocities). The dotted lines show the distribution of stars born in outflows scaled relative to the other stars based on the numbers of the two population. Given the relatively small number of outflow stars, it would be difficult to distinguish any individual stars based on kinematics alone.

A.3 Merger histories

As discussed in §3.3.2, we have explored the importance of mergers in shaping thin/thick disc formation in our simulations. In particular, we focus on merging events that perturb the total mass content within 20 kpc by more than $2 \times 10^{10} M_{\odot}$ in the final coalescence of a satellite and that the merging satellite crossed within the 50 kpc sphere for the first time with more than $5 \times 10^{10} M_{\odot}$ of total mass (which includes both dark matter and baryons). We have made these choices because only above these thresholds do we discern any correlated activity that influences star formation or disc structure.

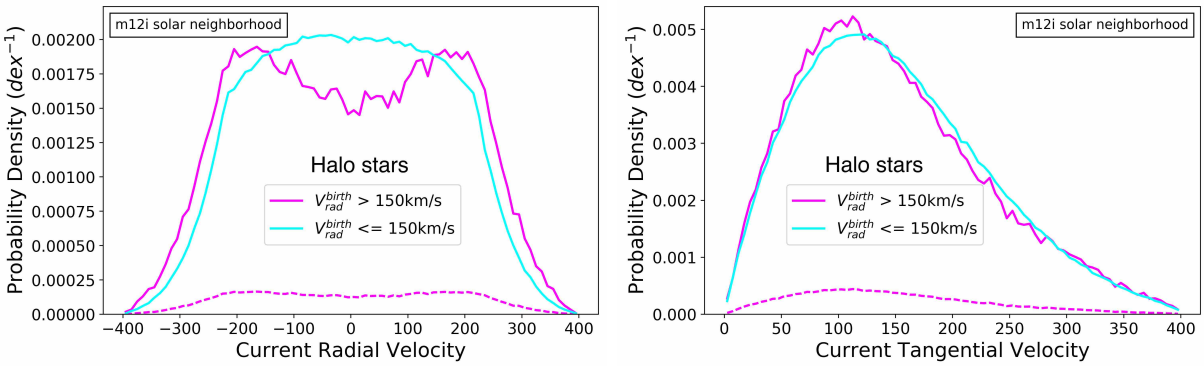

Figure A.3: Current radial and tangential velocity distribution for the local stellar halo in `m12i` split by birth radial velocity. Dotted lines in both plots show the distribution of the outflow stars set to the same scale as the other stars. No substantial differences spotted in both distribution.

Figure 3.6 shows the mass assembly histories (middle panels) for two galaxies that experience late-time mergers by this definition. These mergers happened after the steady phase has commenced and appear to trigger late-time starbursts and also to add to the young-start tail of the age distribution of thick-disc stars. Figure A.5 shows example mass growth histories for two galaxies without such mergers. They also show star formation histories, specifically for `Romeo` (left) and `Juliet` (right). The lower panels show total mass within 50 kpc (dotted) and 20 kpc (solid) for each galaxy. We see that the central galaxies themselves experience little in the way of merger activity that perturbs their overall masses going back prior to the time the steady phase began (red dashed lines). Nevertheless the transition from bursty to steady phase is sharp, and these transition times correlate with thick-disc ages (Fig. 3.7) and thin-disc fractions (Fig. 3.8).

We have tabulated the lookback times of the last $M_{\rm tot} > \times 10^{10} M_{\odot}$ mergers in each of our simulated galaxies. Figure A.4 shows these times plotted against the bursty-phase lookback time, thick disc age, and thin-disc fraction for our galaxies. Four galaxies, `Romeo`, `Juliet`, `m12i`, and `m12m`, experience no such merger over their lifetimes and are not plotted. We find no correlation between the last merger time and bursty-phase lookback time (left panel). We find, at best, weak correlations with thick disc age. A more detailed analysis of possible

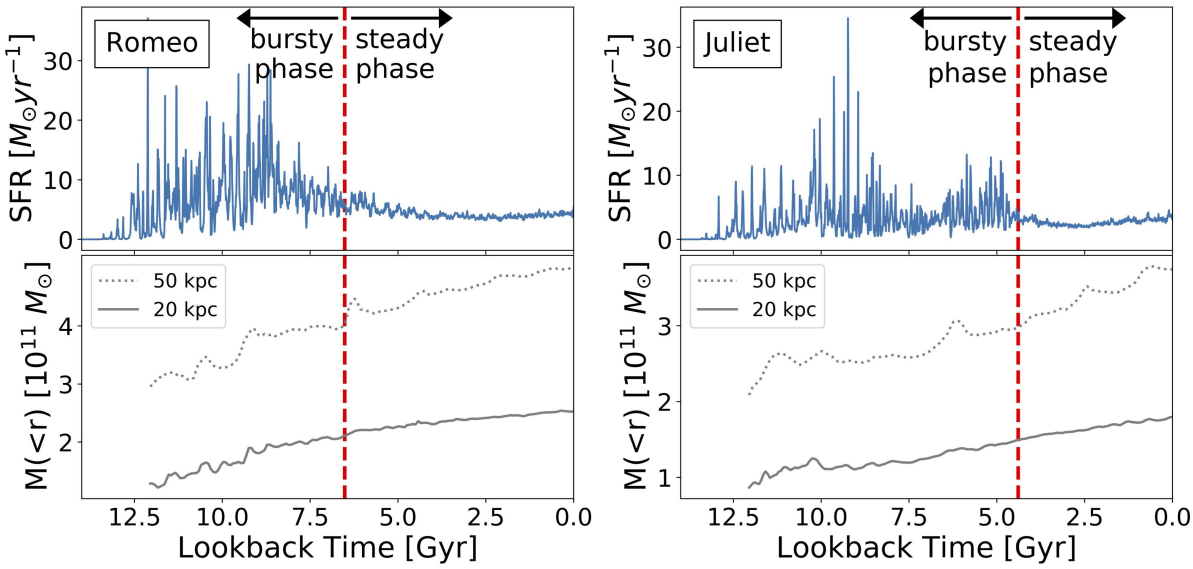

Figure A.4: Star formation histories and mass assembly histories for `Romeo` (left) and `Juliet` (right). The solid and dotted lines in the lower panel show the total mass within 20 kpc and 50 kpc of the main galaxy, respectively, as a function of time. We see that the mass growth is quite steady within 20 kpc, as expected for galaxies without significant merger activities.

correlations between mergers and bursty/steady transition is deferred for future work.

A.4 Properties of all halos

Similar to Figure 4.2, Figure A.6 shows for other four galaxies we have analyzed. Although they have different bursty phase lookback time $t_{\rm B}$, the general trend holds true for all the sample galaxies – at early times, galaxies experience an period of bursty star formation that later transitions into a steady phase with a relatively constant star formation rate. And the transition coincides with the transition of young stars' orbits from radial to more circular and the time when the inner CGM becomes sub-sonic and virialises.

Figure A.7 shows the chemical abundance patterns for stars in different structures classified by circularity ϵ. From left to right, we show the mass-weighted [Mg/Fe] versus [Fe/H] distributions for thin-disc, thick-disc, bulge, and all stars for all five halos as indicated,

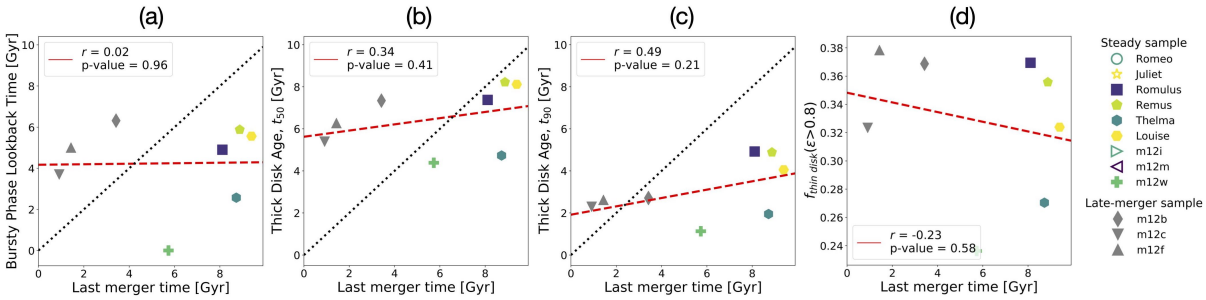

Figure A.5: Correlations between the bursty-phase lookback time, thick-disc age, thin-disc fraction and the last merger lookback time. (a) Bursty-phase lookback time versus the last merger lookback time for each run. We record the merger time as the first central impact time as indicated by the grey dashed line in the middle panel of Figure 3.6. (b) Median thick-disc age (t_{50}) versus the last merger lookback time. (c) Ninetieth percentile youngest thick-disc stars (t_{90}) versus the last merger lookback time. (d) Mass-weighted thin-disc fraction versus the last merger lookback time. The legend (far right) shows the unique symbol type per galaxy similar to Figure 3.7 and Figure 3.8. Note that, colored open markers are not plotted and they correspond to the galaxies that we do not identify any recent mergers from the mass assembly histories. In all panels, we see no significant correlations.

ordered from top to bottom with decreasing bursty phase lookback time $t_{\rm B}$. The thin-disc populations tend to be metal-rich and the thick-disc populations are more alpha-enhanced at fixed iron abundance. The bulge populations are typically more metal-poor and alpha-enhanced. These differences may be loosely interpreted as evidence that thick-disc and bulge stars formed early and rapidly. They formed when the galaxies were less massive, which tend to have lower metallicity. Elements like Mg are produced in core-collapse supernovae (CCSN) on timescales that are significantly shorter than supernovae of Type Ia (SNIa), which produce the majority of iron [194, 154]. The majority of thick-disc and bulge stars form in bursts, which pushed them towards higher α element abundance at fixed [Fe/H].

Parul et al. *in prep* further explores the chemical abundance patterns in FIRE-2 and finds a tight correlation between the scatter in the alpha abundance and the burstiness in star formation. The transition time derived from the scatter of [O/Fe] agrees well with that calculated directly from the star formation history, providing the possibility of utilizing the abundances of Milky-Way stars to infer the history of its star formation.

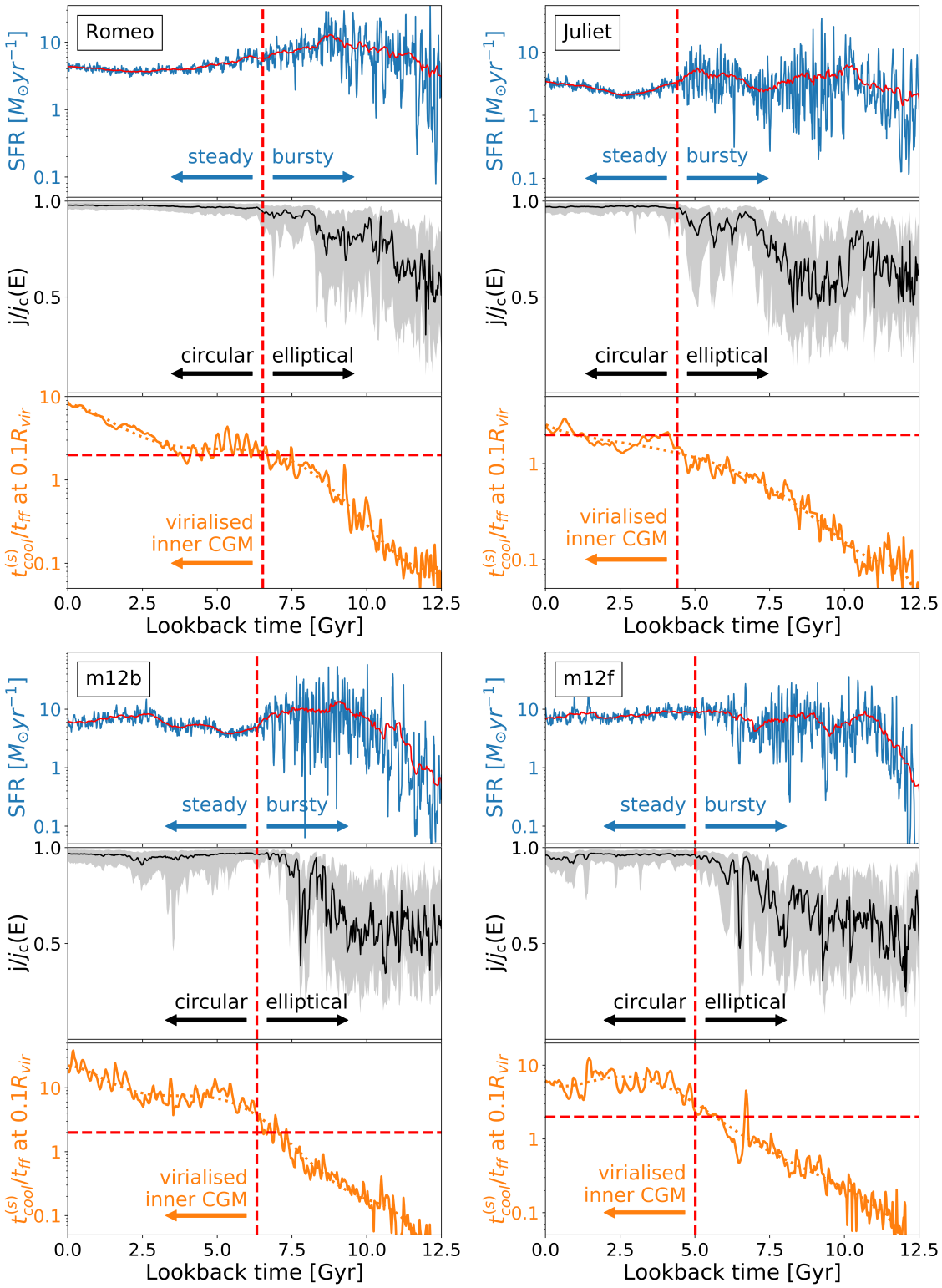

Figure A.6: Similar to Figure 4.2, star formation history, young stars orbital property and CGM virialisation propensity as functions of lookback time for `Romeo`, `Juliet`, `m12b`, and `m12f`.

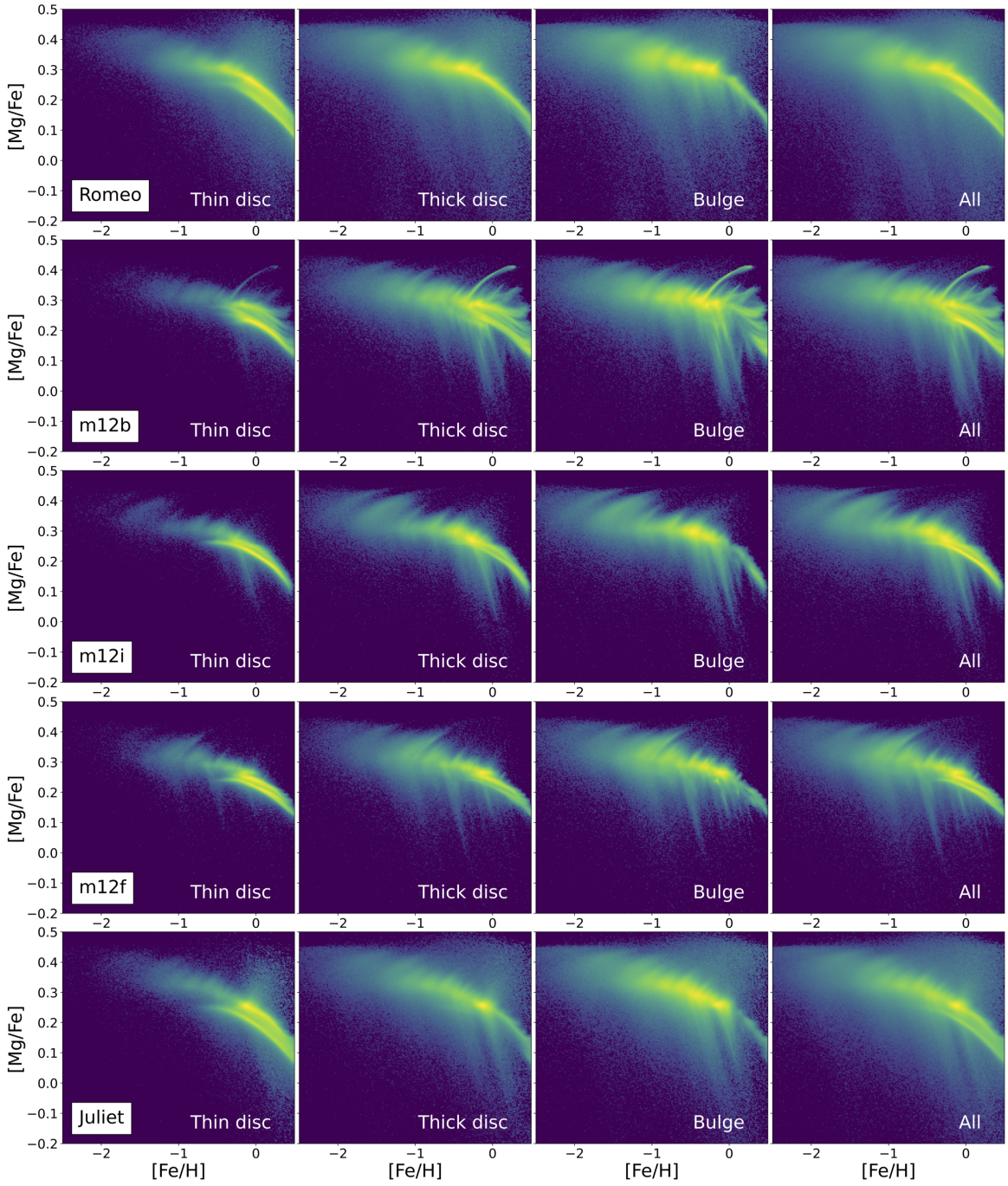

Figure A.7: Chemical abundances for different components identified in the center galaxy. From left to right, we show the 2D density weighted by stellar mass in [Mg/Fe] versus [Fe/H] for thin-disc, thick-disc, bulge, and all stars. Stars classified as thin disc are more metal-rich while thick-disc and bulge stars tend to be more metal-poor and alpha-enhanced.

A.5 Thickening Effect Breakdown

We have briefly explore the "thickening" effect by calculating the average change over time in §4.3.2. Figure A.8 and Figure A.9 here show the "instantenous" effect in all three quantities. Instead of averaging over the entire time period, we select 500-Myr time windows right after stars form and right before $z = 0$. And then we calculate the change in all three quantities over this short period of time. Since the time period we choose is relatively small compared to the cosmological timescale of the transition in the galaxy evolution, it is reasonable to use these two values to quantify the "instantaneous" thickening/heating/torquing effect.

Red dots represent stellar populations born during the bursty phase and blue dots show for stars that form after star formation settles down. The grey dashed lines mark the 0 value. Dots that lie on this line indicate that the corresponding stellar populations have 0 change in ϵ, ϵ_{3D}, or θ during this time period. As we can see, in Figure A.8, $\Delta\epsilon$/Gyr, $\Delta\epsilon_{3D}$/Gyr and $\Delta\theta$/Gyr right before $z = 0$ in both `Romeo` and `m12b` are almost 0 for most stellar populations, especially stars born during the steady phase. Most of the blue dots lie on the grey dashed line. Similar behavior could be seen in Figure A.8 for `m12i`. `m12f`, however, is a little different. The recent merger in `m12f`, as indicated by the black arrows in Figure 4.7, Figure 4.8, and Figure 4.9, would affect the calculation for the orientation of the disc as well as the mass profile of the central galaxy, as discussed in §4.3.2. Therefore, the change around $z = 0$ would still be large compared to `Romeo`, `m12b`, and `m12i`. Overall, stars are getting heated/torqued after they form. But it is more likely to be very temporary and this effect eventually dies down. We did not observe any secular evolution in the stellar populations form after star formation settles down. Combined with the result from §4.3.2, this suggests that disk heating/torquing is too minor to turn thin-disc stars into thick disc and thus is unlikely to be the primary formation mechanism for the bulk of the thick disc stars in the Milky-Way-mass systems.

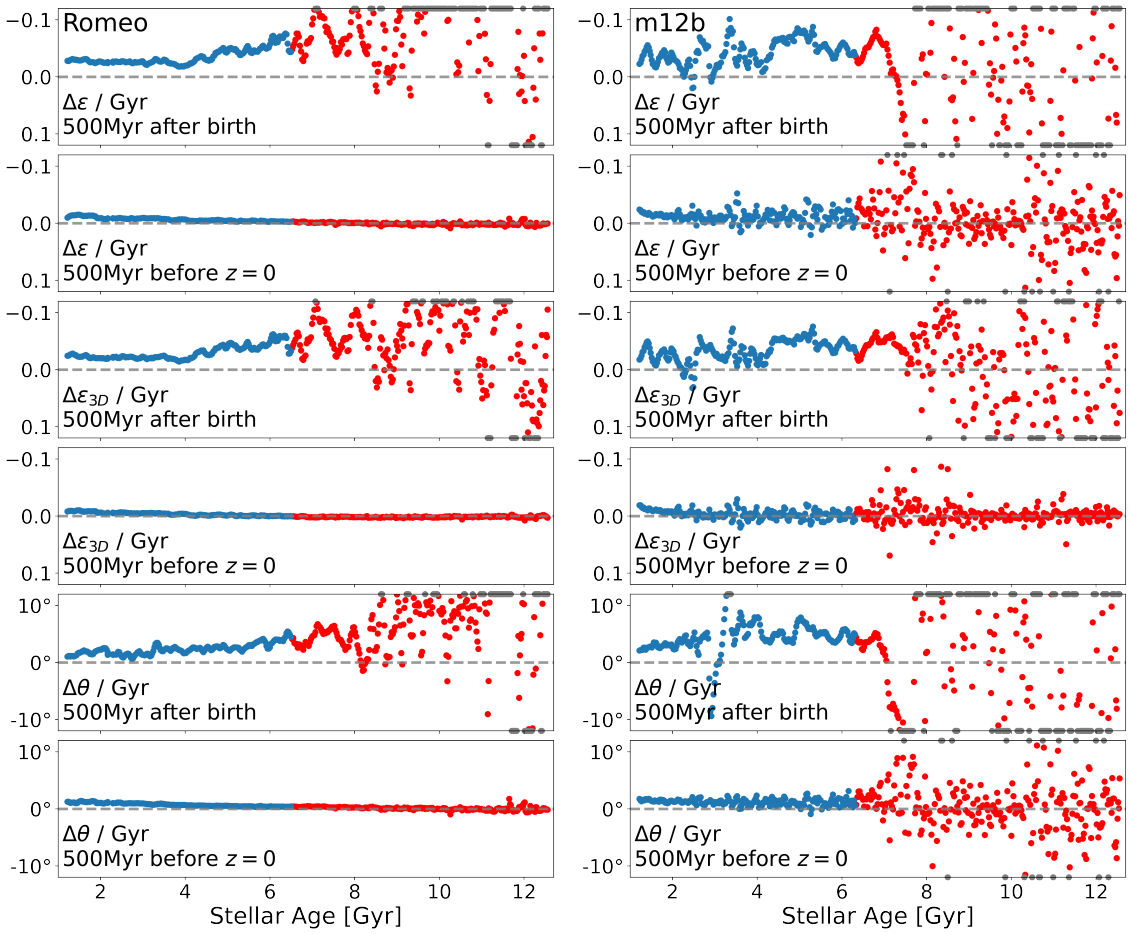

Figure A.8: "Instantaneous" thickening/heating/torquing effect for different stellar populations born at different times in `Romeo` (left) and `m12b` (right). Similar to Figure 4.10, here we quantify the amount of thickening/heating/torquing happening for different populations at birth and now by calculating the change in circularity ϵ, 3D circularity ϵ_{3D}, and alignment angle θ 500 Myr after alignment angle r birth and 500 Myr before $z = 0$. For all three quantities, the change happens mostly right after birth while for the period of time before $z = 0$, the change for all populations, especially the ones born in steady phase, is almost zero. This could also be seen in Figure 4.10 as the lines are getting flatter around 0 Gyr.

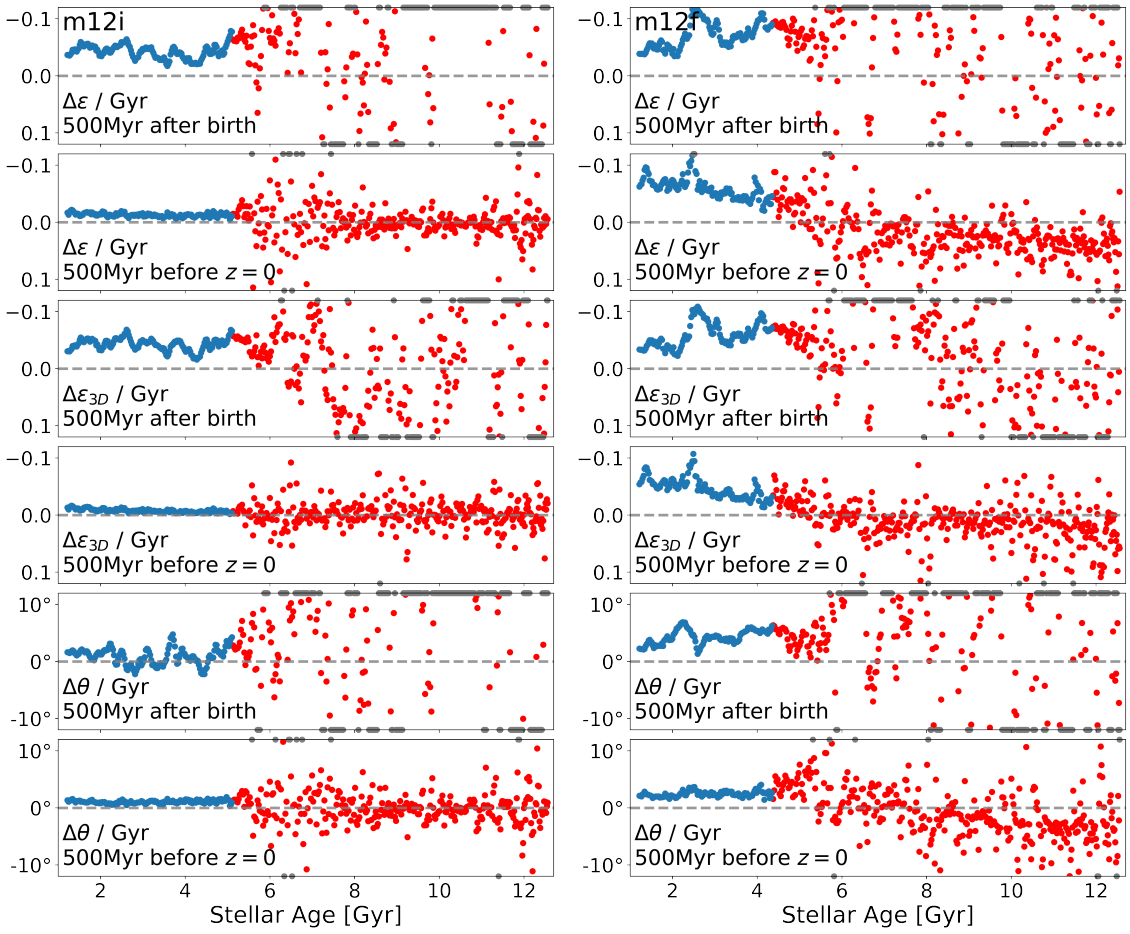

Figure A.9: Same as Figure A.8, now for `m12i` (left) and `m12f` (right). Note that, for `m12f`, the change around $z = 0$ is still large and this is due to the fact that m12f has recently undergone a merger (as indicated by the arrow in Figure 4.7, Figure 4.8, and Figure 4.9). The recent merger would perturb the orientation and total mass of the central galaxy, resulting in fluctuation in all three quantities.